Unfocused Ultrasound Waves for Manipulating and Imaging Microbubbles

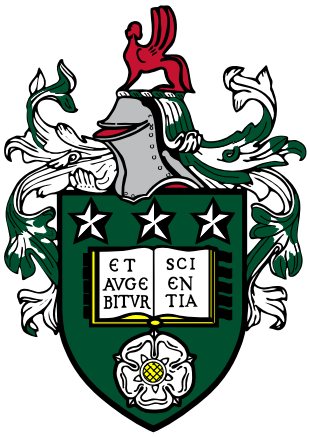

Luzhen Nie

Ultrasonics and Instrumentation Group
School of Electronic and Electrical Engineering

University of Leeds

Submitted in accordance with the requirements for the degree of

Doctor of Philosophy

November 2019

The candidate confirms that the work submitted is his own, except where work which has formed part of jointly authored publications has been included. The contribution of the candidate and the other authors to this work has been explicitly indicated below. The candidate confirms that appropriate credit has been given within the thesis where reference has been made to the work of others.

Chapter 3 contains materials from (Harput *et al.*, 2016; Nie *et al.*, 2016, 2017, 2018b).

Chapter 4 contains materials from (Nie *et al.*, 2018).

Chapter 5 contains materials from (Nie *et al.*, 2018a; Nie *et al.*, 2019).

Chapter 6 contains materials from (Nie *et al.*, 2018a; Nie *et al.*, 2019).

This thesis is dedicated to Mingying Bai.

Acknowledgements

This thesis would not have been possible without help from many people. First and foremost, I owe thanks to my supervisors: Prof. Steven Freear, Dr. Sevan Harput, Dr. James R. McLaughlan, and Dr. David M. J. Cowell.

I am grateful for Steve's wisdom, patience, tolerance, encouragement, and trust during my PhD study. I am thankful for your guidance in developing my research interest and generous support in all aspects of my research.

I must thank Sevan for providing the day-to-day supervision during the first year of my PhD, and with unconditional support, encouraging me to exploit different fields that are of my interest. Especially, chapter 3 owes its existence to you.

I must thank James for voluntarily supervising me during the second year of my PhD before becoming my co-supervisor thereafter. I am grateful for all microbubble-related experimental skills and insightful comments that you have shared, which have made chapters 3 and 4 possible.

Without many years of development, the Ultrasound Array Research Platform II (UARP II) would not have existed. I greatly appreciate the contributions of David and Mr. Thomas M. Carpenter to design, develop and maintain the UARP II, which have underpinned the physical background to support my research and particularly the contents presented here in chapters 3-6.

I have a special gratitude for all my colleges in the Ultrasound Group for their accompany and numerous valuable discussions. I owe my thanks to Dr. Safeer Hyder, Dr. Zainab Alomari, Abdulrhman Alshaya, Dr. Chau Vo Ky, Christopher Cookson, Jordan Tinkler, Damien Batchelor, Harry Clegg, Chunqi Li and anyone else I may forget to mention their names. Especially,

I am grateful to Dr. Christopher Adams, Oscar Knights and Dr. Asraf Moubark for their friendship, enlightening conversations and help.

I would like to thank my close friend Mr. Fei Ma, who was my classmate for six years since 2009 and my housemate for two years since 2013. He originally nudged me to pursue a PhD study.

I must thank our institute administrators Ms. Anna De Jong and Ms. Louise Coffey for their secretarial assistance.

My gratitude would not be complete without special thanks to all of my families. Especially I thank my wife Mingying Bai, your love, patience and unwavering support throughout these years has been at true blessing. I am incapable of articulating my deepest love for you.

Abstract

With unfocused plane/diverging ultrasound waves, the capability of simultaneous sampling on each element of an array transducer has spawned a branch known as high-frame-rate (HFR) ultrasound imaging, whose frame rate can be two orders of magnitude faster than traditional imaging systems. Microbubbles are micron-sized spheres with a heavy gas core that is stabilized by a shell made of lipids, polymers, proteins, or surfactants. They are excellent ultrasound scatters and have been used as ultrasound contrast agents, and more recently researched as a mechanism for targeted drug delivery. With the Ultrasound Array Research Platform II (UARP II), the objective of this thesis was to develop and advance several techniques for manipulating and imaging microbubbles using unfocused ultrasound waves. These techniques were achieved by combining custom transmit/receiving sequencing and advanced signal processing algorithms, holding promise for enhanced diagnostic and therapeutic applications of microbubbles.

A method for locally accumulating microbubbles with fast image guidance was first presented. A linear array transducer performed trapping of microbubble populations interleaved with plane wave imaging, through the use of a composite ultrasound pulse sequence. This technique could enhance image-guided targeted drug delivery using microbubbles.

A key component of targeted drug delivery using liposome-loaded microbubbles and ultrasound is the ability to track these drug vehicles to guide payload release locally. As a uniquely identifiable emission from microbubbles, the subharmonic signal is of interest for this purpose. The feasibility of subharmonic plane wave imaging of liposome-loaded microbubbles was then proved. The improved subharmonic sensitivity especially at depth

compared to their counterpart of bare (unloaded) microbubbles was confirmed.

Following plane wave imaging, the combination of diverging ultrasound waves and microbubbles was investigated. The image formation techniques using coherent summation of diverging waves are susceptible to tissue and microbubble motion artefacts, resulting in poor image quality. A correlation-based 2-D motion estimation algorithm was then proposed to perform motion compensation for HFR contrast-enhanced echocardiography (CEE). A triplex cardiac imaging technique, consisting of B mode, contrast mode and 2-D vector flow imaging with a frame rate of 250 Hz was presented.

It was shown that the efficacy of coherent diverging wave imaging of the heart is reliant on carefully designed motion compensation algorithms capable of correcting for incoherence between steered diverging-wave transmissions. Finally, comparisons were made between the correlation-based method and one established image registration method for motion compensation. Results show that the proposed correlation-based method outperformed the image registration model for motion compensation in HFR CEE, with the improved image contrast ratio and visibility of geometrical borders both *in vitro* and *in vivo*.

Contents

List of Figures

List of Tables

Abbreviations

AM	Amplitude modulation
ARF	Acoustic radiation force
BMUS	British Medical Ultrasound Society
CEE	Contrast-enhanced echocardiography
CNR	Contrast-to-noise ratio
CPS	Contrast pulse sequences
CR	Contrast ratio
CTR	Contrast-to-tissue ratio
CW	Continuous wave
FDA	Food and Drug Administration
FFT	Fast Fourier transform
GPU	Graphics processing unit
HFR	High-frame-rate
HIFUARP	High Intensity Focused Ultrasound Array Research Platform
HRI	High resolution image
HRPWM	Harmonic reduction pulse width modulation
LRI	Low resolution image
LV	Left ventricle
mHRPWM	Modified harmonic reduction pulse width modulation
MI	Mechanical index
MLA	Multi-line acquisition
MOSFET	Metal-oxide-semiconductor field-effect transistor
MV	Multiplane-wave
PCIe	Peripheral component interconnect express
PI	Pulse inversion

PIAM	Pulse inversion amplitude modulation
PMUT	Piezoelectric micromachined ultrasonic transducer
PNP	Peak negative pressure
PRF	Pulse repetition frequency
PZT	Piezoelectric
RMS	Root mean square
ROI	Region of interest
SARUS	Synthetic Aperture Real-time Ultrasound System
SNR	Signal-to-noise ratio
SVD	Singular value decomposition
TMM	Tissue mimicking material
UARP	Ultrasound Array Research Platform
ULA-OP	Ultrasound Advanced Open Platform

List of Symbols

a_i	Contribution of the nonlinear component
$A_{\text{diverging}}$	Physical aperture size for emanating the diverging wave
$B(x)$	Rectangular window function
c	Speed of sound
$C_{\text{Similarity}}$	Image similarity
C_{Smooth}	Penalty term
d	Distance from a microbubble
$\frac{D}{T}$	Pulse duty cycle
d_{v}	Diameter of the vessel
f	Driving frequency
$\bigtriangledown f$	Doppler shift
f_0	Centre frequency of the incident ultrasound wave
f_{b}	Resonant frequency of a microbubble
f_s	Sampling frequency
F_{axial}	Axial radiation force on a microbubble
F_{b}	Radiation force on a microbubble
$\langle f_{\text{d}} \rangle$	Centroid of the Doppler frequency
F_{drag}	Stokes drag force on a microbubble
f_{k}	Image kernel
F_{lateral}	Lateral radiation force on a microbubble
f_{PRF}	Pulse repetition frequency
$\langle f_{\text{RF}} \rangle$	Centroid of the centre frequency of the echo
g_{k}	Image kernel
I	In-phase signal
I_{a}	Acoustic intensity
I_{m}	Maximum acoustic intensity
$I_{\text{p}}, J_{\text{p}}$	Integer pixel coordinates of the correlation peak

$\Delta I_\mathrm{p}, \Delta J_\mathrm{p}$	Subpixel estimations relative to I_p and J_p
I_sppa	Spatial peak pulse average intensity
I_spta	Spatial peak temporal average intensity
$I(t), I(t0)$	Image intensity at t and $t0$
k	Number of clusters
k_i	Number of iterations
L	Entrance length for steady laminar flow
M	Length of the spatial range gate
m	Integer pixel offset
m_b	Mass of a microbubble
N	Doppler ensemble length
n	Integer pixel offset
N_e	Number of active elements
O	Reflected microbubble echo
P	Acoustic Pressure
ΔP	Spatial pressure gradient
P_0	Hydrostatic pressure
P_∞	Pressure at infinity
P_drive	Driving acoustic pressure
P_lateral	Lateral acoustic pressure
$\Delta P_\mathrm{lateral}$	Lateral acoustic pressure gradient
P_MB	Acoustic pressure radiated from a microbubble
P_a	Peak acoustic pressure
Q	Quadrature signal
R	Microbubble radius as a function of time
$\dot{R}$	Microbubble wall velocity
$\ddot{R}$	Microbubble wall acceleration
R_0	Equilibrium microbubble radius
Re	Reynold's number
R_{e0}	Instantaneous variation of the microbubble radius
T	Combined transformation matrix
T_global	Global transformation

T_{local}	Local transformation
v	Relative velocity between the source and the observer
V_0	Equilibrium microbubble volume
v_{b}	Microbubble velocity
v_{f}	Liquid velocity
v_{max}	Maximum velocity
v_{mean}	Mean velocity
$V(t)$	Microbubble volume
v_{z}	Axial velocity
v_{z2D}	Axial velocity using the 2-D autocorrelator
v_{zmax}	Maximum detectable velocity in the axial direction
W_{x}	Pressure amplitude modulation function
(x, z)	Position of a point
(x', z')	Position of a virtual source
x_1	Element address
$x(t)$	Ultrasound basis function
Z	Acoustic impedance
α	Steering angle
β	Divergent angle
β_{tot}	Dimensionless damping coefficient
η	Dynamic viscosity of the liquid
κ_S	Dilatational viscosity of the microbubble shell
λ	One wavelength
λ_{lateral}	Wavelength of the modelled sinusoidal pattern in acoustic trapping
λ_{w}	Weighting parameter
ρ	Density of the propagating medium
ρ_{L}	Liquid density
σ	Surface tension between the liquid and bubble surface
μ	Viscosity of the liquid
Φ	Coefficient map of cross correlation
χ	Microbubble shell elasticity
ω	Angular driving frequency
ω_0	Angular resonant frequency of a microbubble

Chapter 1

Introduction

1.1 History

Ultrasound, a sub-discipline of acoustics, has broadened our horizons to see a world invisible to us. It is a type of longitudinal wave and it compresses and rarefies the medium during propagation. The particles of the medium undergo displacement in line with the oscillations of this wave. With reflection, it can be used for localising objects. The early use of ultrasound for echo-localisation extends back over 100 years to detect submarines during World War I (Szabo, 2004). However, the connection between underwater echo ranging and the application of ultrasound for healthcare diagnostics was not made until the allied science and technologies, such as piezoelectric (PZT) transducers, matured. The success of radar techniques in World War II hastened the evolution of 2-D underwater echo ranging techniques. With the understanding of bioeffects induced by ultrasound on tissue, numerous eminent scientists started to use ultrasound to scan human bodies with safe exposures. Ultrasound imaging of the head/brain was first explored in the 1940s, but little progress was made over years due to the strong skull attenuation. The consistence of the speed of sound (1540 m/s) in different types of soft tissue enables accurate localisation of the target with the round-trip time delays. Thus, a 2-D B-mode image reconstructed from the ultrasound echo can be faithful to represent the tissue geometry. From then on, the application list of diagnostic ultrasound has been expanding to cover cardiac imaging, baby scanning and abdominal diagnosis, among others. Over other imaging modalities, such as CT and MRI, ultrasound imaging has advantages of being affordable and portable. The continuing develop-

ments of enabling techniques have shaped the medical ultrasound imaging field since its birth. The advances of electronics, seemingly nonrelevant, have revolutionized the development of medical ultrasound imaging systems including ultrasonic transducers, accelerating their continuous miniaturization but with equivalent or enhanced imaging capabilities.

The development and use of microbubble contrast agents is a sub-discipline of medical ultrasound imaging. The story dates back to 1968 in echocardiography (Gramiak & Shah, 1968) with the demonstration of enhanced reflection in the aortic root due to the injection of air bubbles. The boundary layer between the air bubble and blood creates a substantial impedance mismatch, accounting for the enhanced reflection. The early efforts (Feigenbaum *et al.*, 1970) were seen mainly for diagnosis of cardiac diseases such as the leaked valve and shunts. However, limited by the large size and short lifetime, the widespread investigations did not occur until the development of encapsulated microbubbles in the early 1990s. Nowadays, the most common microbubbles are micron-sized gas-filled spheres that are encapsulated by a shell made of lipids, proteins, polymers or surfactants (Mulvana *et al.*, 2017). The shell facilitates prolonged stability of the microbubble in circulation and allows for substantial oscillations when subject to an ultrasonic field even with a low mechanical index (MI) (Apfel & Holland, 1991; Church, 2005). When using conventional ultrasound beams, such as that for colour Doppler imaging, the ultrasound signal can be amplified by 1000 folds (Greis, 2004), but at the cost of losing echogenicity in a few seconds. The understanding of microbubbles' nonlinear behaviour under ultrasonic exposure underpins myriad microbubble-specific detection techniques under low MI, such as second harmonic imaging (van Neer *et al.*, 2011), subharmonic imaging (Harput *et al.*, 2013), superharmonic imaging (Bouakaz *et al.*, 2003), pulse inversion (PI) (Eckersley *et al.*, 2005), amplitude modulation (AM) (Eckersley *et al.*, 2005) and contrast pulse sequences (CPS) (Phillips, 2001), among others. Clinically, the injection of microbubbles is used to increase the contrast between blood and tissue, enhancing the imaging sensitivity for deep organs (Senior *et al.*, 2009). Imaging blood flow at the microvascular level is the key advantage with microbubbles, where tissue perfusion can be analysed (Hohmann *et al.*, 2003). The commonly used phospholipid microbubbles available in the market are shown in Fig. 1.1 and their properties are shown in Table 1.1. Apart from the use as imaging contrast agents, engineering microbubbles for targeted drug or gene

delivery (Skachkov *et al.*, 2014) is a highly active area of research. Microbubbles can be functionalised by coagulating targeting ligands (Klibanov, 2009) as well as loaded with drug-filled liposomes (Peyman *et al.*, 2012), with which targeted drug release can be triggered by bursting microbubbles using high intensity ultrasound (Escoffre *et al.*, 2013).

Figure 1.1: Schematic of the phospholipid microbubble and the commercially available products: SonoVue, MicroMarker, Optison and Definity. Image courtesy of Dr. James R. McLaughlan at the University of Leeds.

Table 1.1: Properties of Phospholipid Microbubbles Available in the Market (Arif, 2010)

Brand	Manufacture	Gas	Size Range	Concentration (mb/ml)	Use
SonoVue	Bracco	SF_6	~2.95 μm (1−10 μm)	(2.0−5.0) x 10^8	Clinical
MicroMarker	FUJIFILM VisualSonics	C_4F_{10}/N_2	2.3−2.9 μm	2.0 x 10^9	Pre-clinical
Optison	GE Healthcare	C_3F_8	3.0−4.5 μm (1−32 μm)	(5.0−8.0) x 10^8	Clinical
Definity	Lantheus Medical Imaging	C_3F_8	1.1−3.3 μm (1−20 μm)	1.2 x 10^{10}	Clinical

In the last two decades, the maturing computer and electronics industry has vastly promoted multiple innovations such as the development of 2-D piezoelectric micromachined ultrasonic transducers (PMUTs) (Qiu *et al.*, 2015) and the pocket ultrasound

scanner which were not readily achievable before. Clinical systems are constrained by cost and not easily modified which needlessly impairs ultrasound research that requires arbitrary waveform generation and reconfiguration of transmit sequences. The capability of exciting and sampling each individual element of an array transducer has spawned a branch of high-frame-rate (HFR) imaging using plane/diverging waves (Boni *et al.*, 2018). HFR ultrasound technology opens new vistas for the development of new methods for vector flow mapping (Ricci *et al.*, 2018), tissue elasticity mapping (Montaldo *et al.*, 2009) and functional brain imaging (Macé *et al.*, 2011). Fig. 1.2 shows the typical HFR ultrasound platforms and Table 1.2 gives their main specifications (Boni *et al.*, 2018). The Ultrasound Array Research Platform (UARP) has been fastidiously developed by the Ultrasound Group at the University of Leeds over 10 years. It is a scalable system consisting of 16-channel modules controlled by Stratix V FPGA, supporting truly arbitrary sequencing of transmit and receiving on each channel. The UARP technologies feature a quinary excitation scheme (Cowell & Freear, 2008) together with harmonic reduced pulse width modulation (Cowell *et al.*, 2013). Each module is equipped with 1 GB DDR3 on-board memory, with raw data streamed to a PC through peripheral component interconnect express (PCIe) for further elaboration in post processing. Fig. 1.3(a) shows one 16-channel module and Fig. 1.3(b) shows the 128-channel configuration for the UARP II as shown in Fig. 1.2(a).

1.2 Motivation

The combination of unfocused ultrasound waves and microbubbles was initially explored in (Couture *et al.*, 2009), where the transient phase of microbubble collapse was depicted by using HFR plane wave imaging, enabling a vastly improved contrast-to-tissue (CTR) ratio. From then on, methods aiming to achieve super-temporal (Leow *et al.*, 2015) and super-spatial resolutions (Errico *et al.*, 2015) have been researched by taking advantages of the large amount of data afforded by HFR microbubble-enhanced ultrasound. In addition, it was shown that when subject to an ultrasound field, microbubbles can be manipulated by using acoustic radiation force (ARF) (Dayton *et al.*, 1999). The interaction between microbubbles and cells was proved to enhance drug uptake through a process called sonoporation (Mclaughlan *et al.*, 2013). Guiding microbubbles using ARF and imaging them using a single array transducer could improve

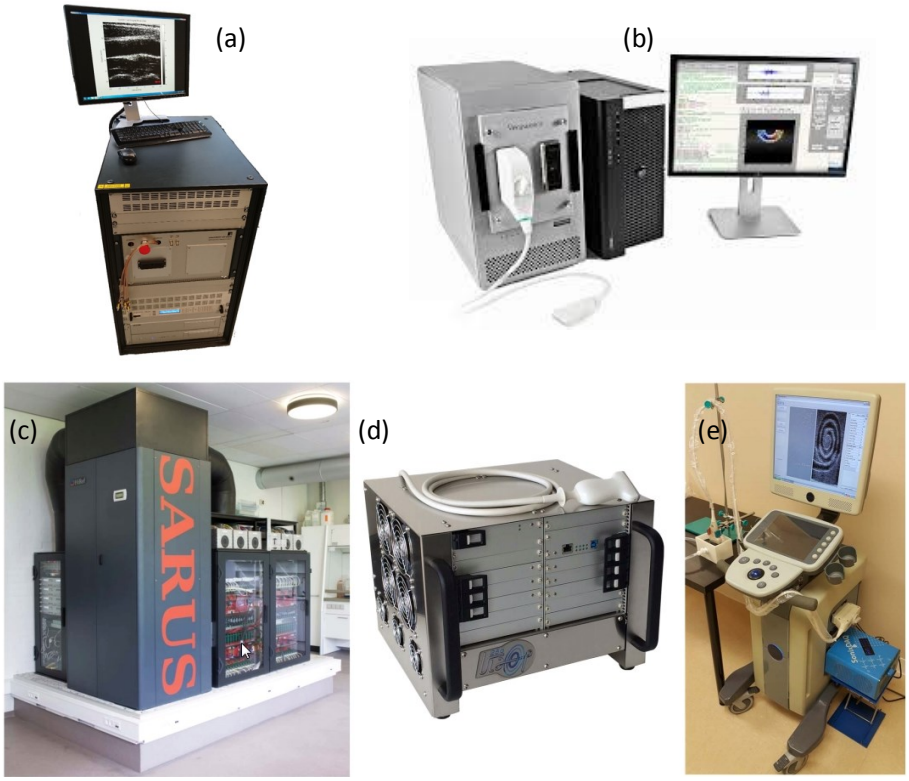

Figure 1.2: (a) Ultrasound Array Research Platform II (UARP II) developed by the Ultrasound Group at the University of Leeds (Nie *et al.*, 2018b). (b) Verasonics Vantage 256 (Kirkland, WA, USA). (c) Synthetic Aperture Real-time Ultrasound System (SARUS) developed at the Technical University of Denmark (Jensen *et al.*, 2013). (d) Ultrasound Advanced Open Platform 256 (ULA-OP 256) developed at the University of Florence (Boni *et al.*, 2016). (e) SonixTouch research scanner (Cheung *et al.*, 2012).

Table 1.2: Specifications of Main HFR Ultrasound Platforms

	UARP II	Vantage 256	SARUS	ULA-OP 256	SonixTouch
Channels	Up to 256 Tx/Rx	256 Tx/Rx	Up to 1024 Tx/Rx	Up to 256 Tx/Rx	128 Tx/Rx
Tx voltage	Up to 200 V_{pp}	3 to 190 V_{pp}	Up to 200 V_{pp}	Up to 200 V_{pp}	Up to 50 V_{pp}
Tx Freq.	0.5 to 15 MHz	0.5 to 20 MHz (standard configuration)	1 to 30 MHz	1 to 20 MHz	1 to 20 MHz
Tx Type	5-Level	3-Level	Linear	Linear	3-Level
ADC	programmable sampling rate up to 80 MHz @ 12 bits	programmable sampling rate up to 62.5 MHz @ 14 bits	70 MHz @ 12 bits, programmable downsampling with filtration	78 MHz @ 12 bits, programmable downsampling	80 MHz @ 10 bits/ 40 MHz @ 12 bits
Buffer	16 GB	16 GB	128 GB	80 GB	16 GB
Connection to PC	PCIe 3.0	PCIe 3.0	64 1GB/s ethernet links coupled through four 10 GB/s optical links	USB 3.0	USB 2.0

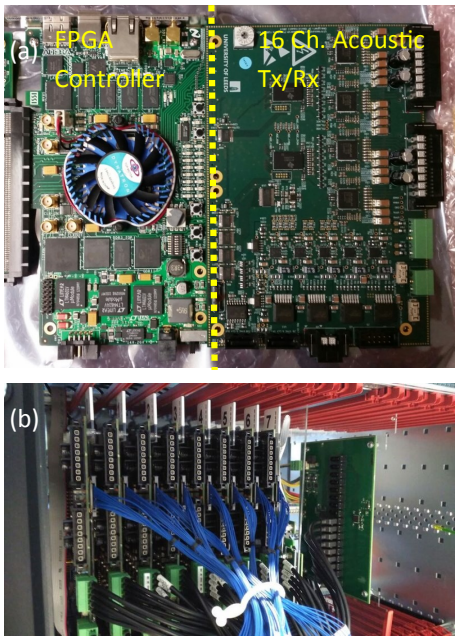

Figure 1.3: (a) One 16-channel module. (B) 128-channel configuration with 8 modules for the UARP II.

microbubble-mediated targeted drug delivery by enabling more localised treatment with imaging feedback. In this thesis, custom sequencing of unfocused ultrasound transmissions and advanced signal processing algorithms are combined to manipulate and image microbubbles by using the flexible UARP II, with the potential for both diagnostic and therapeutic applications.

1.3 Thesis Outline

The work presented is divided into 7 chapters including the first chapter for the introduction of the research.

Chapter 2 reviews the underpinning knowledge of medical ultrasound imaging. This encompasses physics of ultrasound, B-mode imaging, ultrasound transducers, ultrasound Doppler imaging, nonlinear ultrasonics, microbubble contrast-enhanced imaging and HFR ultrasound imaging using plane/diverging waves.

There has been a surge of interest in using microbubbles for targeted drug delivery. The next chapter demonstrates microbubble trapping against arterial flow rates in a large vessel by using the custom-designed transmit beams, with feedback provided by the interleaved sequence for plane wave imaging. With a single linear array transducer, this technique could contribute to image-guided targeted drug delivery, with the capability of locally increasing the concentration of payload when microbubbles are used as drug vehicles.

Chapter 4 continues on the use of plane waves by demonstrating subharmonic plane wave imaging of liposome-loaded microbubbles. The improved subharmonic sensitivity compared to their counterpart of bare microbubbles was confirmed, providing a means to specifically track the drug payload using subharmonic signals.

The advent of HFR ultrasound imaging using diverging waves is ushering revolutionary ways to assess cardiac function. Chapter 5 demonstrates diverging-wave microbubble-enhanced echocardiography with 2-D motion compensation. With the same pulse sequence, HFR B-mode imaging, contrast-mode imaging and 2-D vector blood flow mapping were obtained simultaneously at 250 Hz.

In an extension to chapter 5, two methods for motion compensation in coherent diverging wave imaging are compared in chapter 6. The proposed correlation-based

method outperformed the image registration-based technique, by providing enhanced border delineation *in vitro* and the improved CTR *in vivo*.

The last chapter summarizes the presented work.

1.4 Contributions

This thesis was built upon the extensive use of the bespoke UARP II. The research contribution of the candidate and other co-authors has been explicitly explained below. The results of this thesis have been published in two journal papers, five conference papers, and four conference abstracts. The research performed in this work also contributed to two conference papers and one conference abstract that are not presented in this thesis. The associated work for the 24th European Symposium on Ultrasound Contrast Imaging was awarded the best poster prize in the category of technology in January 2019 at Rotterdam. The associated paper was selected as the front cover of *IEEE Transactions on Ultrasonics, Ferroelectrics, and Frequency Control* in February 2019.

Journal Papers

- Luzhen Nie, David M. J. Cowell, Thomas M. Carpenter, James R. McLaughlan, Arzu A. Çubukçu, and Steven Freear, "High-Frame-Rate Contrast-Enhanced Echocardiography Using Diverging Waves: 2-D Motion Estimation and Compensation," *IEEE Transactions on Ultrasonics, Ferroelectrics, and Frequency Control*, vol. 66, no. 2, pp. 359−371, Feb. 2019.

I was responsible for the concept, simulation programs, experiments and preparation of the manuscript. D. M. J. Cowell and T. M. Carpenter were responsible for the array excitations. S. Freear, J. R. McLaughlan and A. A. Çubukçu supervised the project.

- Luzhen Nie, Sevan Harput, David M. J. Cowell, Thomas M. Carpenter, James R. McLaughlan, and Steven Freear, "Combining Acoustic Trapping with Plane Wave Imaging for Localized Microbubble Accumulation in Large Vessels," *IEEE Transactions on Ultrasonics, Ferroelectrics, and Frequency Control*, vol. 65, no. 7, pp. 1193−1204, July 2018.

S. Freear, J. R. McLaughlan and S. Harput were responsible for the concept. I was responsible for the simulation programs, experiments and preparation of the manuscript. D. M. J. Cowell and T. M. Carpenter were responsible for the array excitations.

Conference Papers

- Luzhen Nie, James R. McLaughlan, David M. J. Cowell, Thomas M. Carpenter, and Steven Freear, "Subharmonic Plane Wave Imaging of Liposome-loaded Microbubbles," *2018 IEEE International Ultrasonics Symposium (IUS).*
- Luzhen Nie, Thomas M. Carpenter, David M. J. Cowell, James R. McLaughlan, Arzu A. Çubukçu, and Steven Freear, "Coherent Diverging Wave Imaging with 2-D Motion Compensation," *2018 IEEE International Ultrasonics Symposium (IUS).*
- Luzhen Nie, Sevan Harput, James R. McLaughlan, David M. J. Cowell, Thomas M. Carpenter, and Steven Freear, "Acoustic Microbubble Trapping in Blood Mimicking Fluid," *2017 IEEE International Ultrasonics Symposium (IUS).*
- Chris Adams, David M. J. Cowell, Luzhen Nie, James R. McLaughlan, Thomas M. Carpenter, and Steven Freear, "A HIFU Excitation Scheme to Reduce Switching-induced Grating Lobes and Hard Tissue Interface Heating," *2017 IEEE International Ultrasonics Symposium (IUS).*
- Chris Adams, James R. McLaughlan, Luzhen Nie, and Steven Freear, "Excitation and Acquisition of Cranial Guided Waves Using A Concave Array Transducer," *Proceedings of Meetings on Acoustics 173EAA*. Vol. 30. No. 1. ASA, 2017.
- Luzhen Nie, Sevan Harput, David M. J. Cowell, and Steven Freear, "Velocity Estimation Error Reduction in Stenosis Areas Using A Correlation Correction Method," *2016 IEEE International Ultrasonics Symposium (IUS).*
- Sevan Harput, Luzhen Nie, David M. J. Cowell, Thomas M. Carpenter, B. Raiton, James R. McLaughlan, and Steven Freear, "Simultaneous Trapping and Imaging of Microbubbles at Clinically Relevant Flow Rates," *2016 IEEE International Ultrasonics Symposium (IUS).*

I was responsible for the entirety of these first-author publications, except the initial concept of the first conference paper which J. R. McLaughlan was responsible for. For the fourth and fifth papers, I designed the transducer delay profiles. For the last paper which was written by S. Harput, I was responsible for rendering vector flow maps.

Conference Abstracts

- Luzhen Nie, David M. J. Cowell, Thomas M. Carpenter, James R. McLaughlan, Arzu A. Çubukçu, and Steven Freear, "Motion Compensation for High-Frame-Rate Contrast-Enhanced Echocardiography Using Diverging Waves," *The 24th European Symposium on Ultrasound Contrast Imaging*, Rotterdam, Jan. 2019.

- Luzhen Nie, James R. McLaughlan, Thomas M. Carpenter, David M. J. Cowell, and Steven Freear, "Subharmonic Imaging of Liposome-loaded Microbubbles," *The 23rd European Symposium on Ultrasound Contrast Imaging*, Rotterdam, Jan. 2018.

- Luzhen Nie, Sevan Harput, David M. J. Cowell, Thomas M. Carpenter, James R. McLaughlan, and Steven Freear, "Acoustic Microbubble Trapping for Enhanced Targeted Drug Delivery," *The Journal of the Acoustical Society of America*, 141 (5), 4012-4012, May 2017.

- Chris Adams, James R. McLaughlan, Luzhen Nie, David M. J. Cowell, Thomas M. Carpenter, and Steven Freear, "Excitation of Leaky Lamb Waves in Cranial Bone Using A Phased Array Transducer in A Concave Therapeutic Configuration," *The Journal of the Acoustical Society of America*, 141(5), 3918-3918, May 2017.

- Luzhen Nie, Sevan Harput, David M. J. Cowell, Thomas M. Carpenter, James R. McLaughlan, and Steven Freear, "Microbubble Trapping, Imaging and Destruction for Targeted Drug Delivery," *The 22nd European Symposium on Ultrasound Contrast Imaging*, Rotterdam, Jan. 2017.

I was responsible for the entirety of these abstracts, except the fourth one for which I designed the transducer delay profiles.

Chapter 2

Literature Review

Over the past few decades, medical ultrasound imaging has continued to constitute an important aid for healthcare diagnostics. The list of its applications is expanding including 2-D or 3-D blood flow imaging (Osmanski *et al.*, 2014), elasticity imaging of soft tissue (Grondin *et al.*, 2017), wall motion analysis (Senior *et al.*, 2009) and myocardial perfusion imaging with microbubbles (Senior *et al.*, 2009), among others. Intriguing innovations such as ultrasound molecular imaging (Daeichin *et al.*, 2015) and super-resolution ultrasound imaging (Errico *et al.*, 2015) are also being widely explored for cancer diagnosis (Kaneko & Willmann, 2012; Opacic *et al.*, 2018). This chapter revisits the basic principles and related physics of ultrasound imaging which lay the solid basis for the work in this thesis.

2.1 Fundamental Principles of Medical Ultrasound Imaging

2.1.1 B-mode Imaging and Ultrasound Array Transducers

A B-mode image is the cross-sectional representation of the tissue boundary and structure as shown in Fig. 2.1. It is reconstructed with echoes that are reflected back from the tissue boundary and received by the elements in an array transducer as shown in Fig. 2.2. As the speed of sound in soft tissue is relatively constant (∼1540 m/s), the positions of scattering points can be faithfully located by calculating the time of flight, precisely depicting the anatomical structure. The received echoes are beamformed, envelope detected, and log-compressed to create a map with different brightness values.

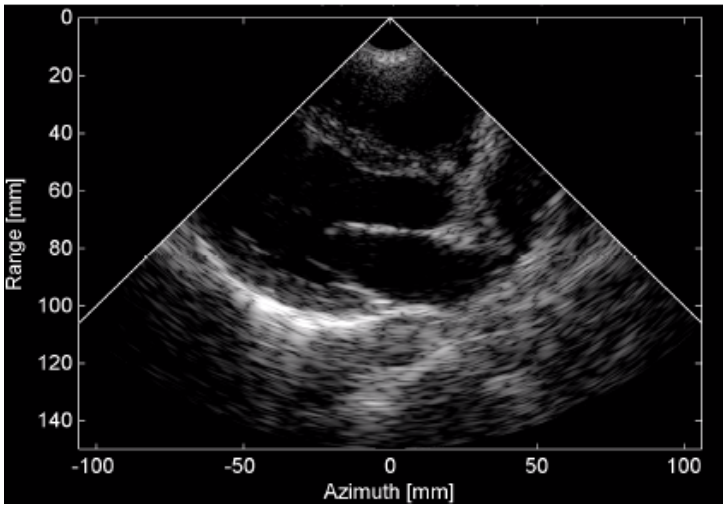

Figure 2.1: Parasternal long axis view of a heart. Reproduced from (Tong *et al.*, 2019) with permission under the CC-BY 4.0 licence.

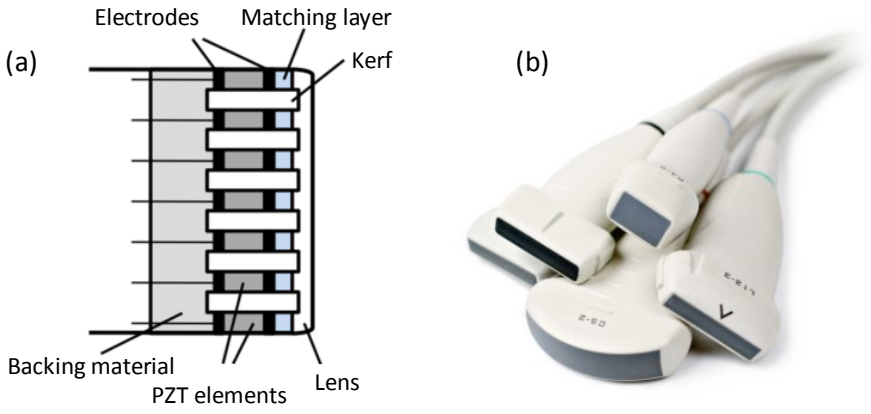

Figure 2.2: (a) Components of an array transducer. (b) Group of transducers that are compatible to the UARP II.

'B-mode' is thus the short name of 'brightness mode'.

B-mode imaging is a pulse-echo technique in which the array transducers play a vital role as the transmitter and sensing device. As shown in Fig. 2.2(a), a typical multi-element array transducer consists of PZT ceramics, a matching layer, an acoustic lens, backing materials and wires that are attached to both sides of the PZT ceramics through electrodes. The PZT elements are compressed or stretched to send ultrasonic waves when a positive or negative voltage is applied through them, converting electrical energy to ultrasonic power, and vice versa. A thin layer of conductive paint is coated on both sides of the PZT elements as the electrodes. The matching layer is used to decrease the acoustic impedance mismatch between the PZT elements and the coupling medium, such as the ultrasound gel, minimising the loss of transmitted acoustic energy. An acoustic lens is typically adopted to generate the elevation focus, at which the elevation resolution achieves its best. Due to reverberations within the PZT elements, the backward reflection needs to be attenuated by using a strong absorbing backing layer. For further reading on the structure of ultrasonic array transducers, please refer to (Hoskins *et al.*, 2010; Szabo, 2004).

As shown in Fig. 2.2(b), a group of medical array transducers are available in the market, fulfilling the need for scanning different parts of the body, such as superficial carotid arteries or a relatively deep heart. The formation of B-mode images varies with the type of transducer adopted. A linear array transducer is composed of sequential PZT elements in a line, with beams or imaging lines typically perpendicular to the array, as shown in Fig. 2.3(a). For an expanded field of view when scanning a heart or baby, a phased or curvilinear array transducer is adopted, with varied imaging formats as shown in Fig. 2.3(b) and Fig. 2.3(c). The phased array transducer is fabricated in a way similar to that for a liner array transducer, except the pitch size is not larger than one half wavelength (see Section 2.1.2 for its definition), avoiding grating lobes in the imaging field during beam steering. In addition, the curvilinear array transducer is similar to the curved version of the linear array transducer.

2.1.2 Frequency, Speed of Sound, Wavelength, Pressure, Intensity and MI

The ultrasonic waves used for medical applications are longitudinal waves. If the PZT elements are static, the surrounding medium will be in the rest condition where there

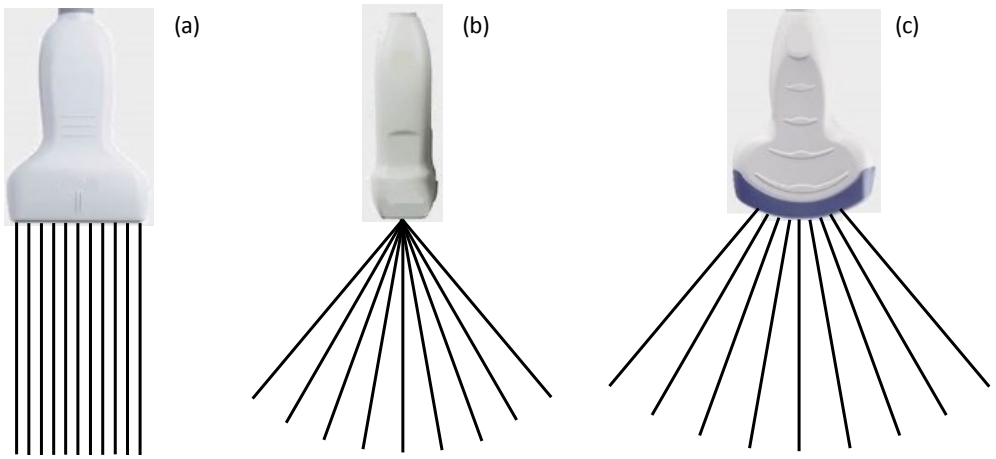

Figure 2.3: Different imaging formats with a (a) linear array transducer, (b) phased array transducer and (c) curvilinear array transducer. The black lines represent the focused beams or beamformed imaging lines.

will be a rest acoustic pressure at all locations. Applying voltages on both sides of the PZT elements displaces the PZT surface. As a result, a positive or negative acoustic pressure relative to the rest pressure exists, resulting in medium compression and rarefaction as shown in Fig. 2.4(a). The energy is transported through the passage of the wave in the medium.

Frequency represents the number of repeated wave cycles in a second. Its unit is hertz/Hz (1 Hz = 1 cycle per second). The audible sound waves have a frequency range of 20 Hz−20 kHz, whilst the ultrasonic waves have a frequency above 20 kHz. For medical ultrasound imaging, the frequency typically varies between 1 MHz and 10 MHz, encompassing most applications excluding intravascular ultrasound imaging that employs higher frequencies. The ultrasonic wave with a frequency of f_0, propagating through the medium with a speed of sound of c, has a wavelength of λ ($\lambda = c/f_0$). The wavelength represents the distance between consecutive similar points on the wave as illustrated in Fig. 2.4(a).

The pressure amplitude relative to the rest value corresponds to the acoustic intensity. The relationship between them is described by $I_\mathrm{a} = \dfrac{P^2}{\rho c}$, where I_a is the acoustic intensity, P is the relative acoustic pressure (normally referred to as acoustic pressure), and ρ is the density of the propagating medium. Pressures are first measured by using needle or membrane hydrophones which are calibrated by the National Physical Labo-

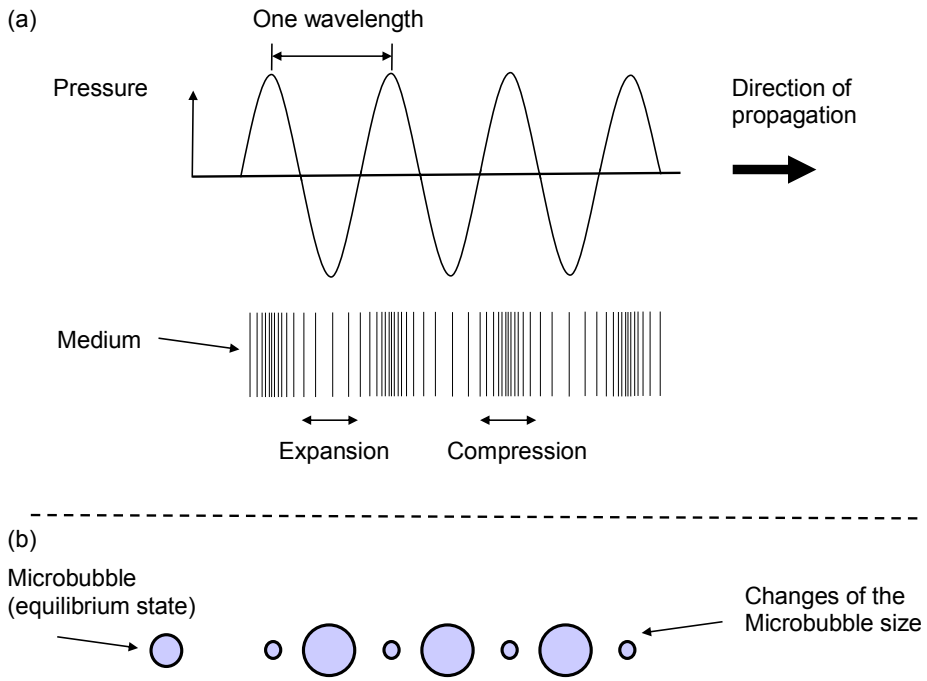

Figure 2.4: (a) Medium expansion and compression in line with the acoustic pressure distribution. (b) Schematic diagram showing microbubble compression in response to the positive pressure and expansion during the negative part of the ultrasound wave.

ratory in the U.K. The Food and Drug Administration (FDA) (Food *et al.*, 1985) and the British Medical Ultrasound Society (BMUS) (BMUS, 2010) regulate the limits of acoustic outputs for medical ultrasound imaging, with values given in Table 2.1.

Table 2.1: Limits of Acoustic Outputs for Medical Ultrasound Imaging

	I_{sppa}	I_{spta}	I_{m}	MI
FDA	240	1500	600	1.9
Unit	W/cm^2	mW/cm^2	W/cm^2	–

where I_{sppa} is the spatial peak pulse average intensity, I_{spta} is the spatial peak temporal average intensity, and I_{m} is the maximum intensity. MI denotes mechanical index which is determined by $\text{MI} = \text{PNP}/\sqrt{f_0}$, where PNP is the peak negative pressure (MPa) and f_0 is the centre frequency of the ultrasound wave (MHz).

2.1.3 Reflection, Scattering and Attenuation

The B-mode images are formed with echoes that are reflected back from the tissue boundaries because of the differences in acoustic impedance. The acoustic impedance of a medium Z is formulated as $Z = \rho c$. When the beam insonifies the object of size similar to or smaller than a wavelength, the wave is scattered over a large range of angles as shown in Fig. 2.5. The scattered signal is received by multiple elements across an array, facilitating parallel beamforming when using unfocused ultrasound waves which will be discussed in Section 2.3. When propagating through the medium, the transported energy is decreased mainly by the mechanism of absorption where the acoustic energy is transferred to thermal energy. Attenuation is frequency relevant, and Table. 2.2 (Hoskins *et al.*, 2010) gives the attenuation values for different types of tissue.

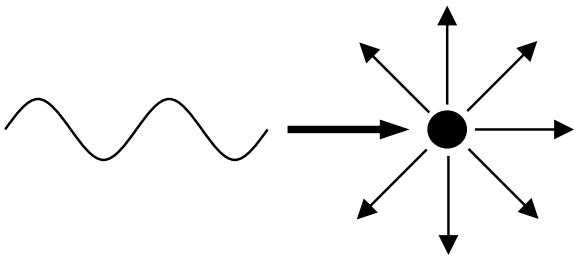

Figure 2.5: Illustration of scattering.

Table 2.2: Acoustic Attenuation Values of Different Types of Tissue

Tissue	Attenuation(dB/MHz/cm)
Liver	0.399
Brain	0.435
Muscle	0.57
Blood	0.15
Water	0.02
Bone	22

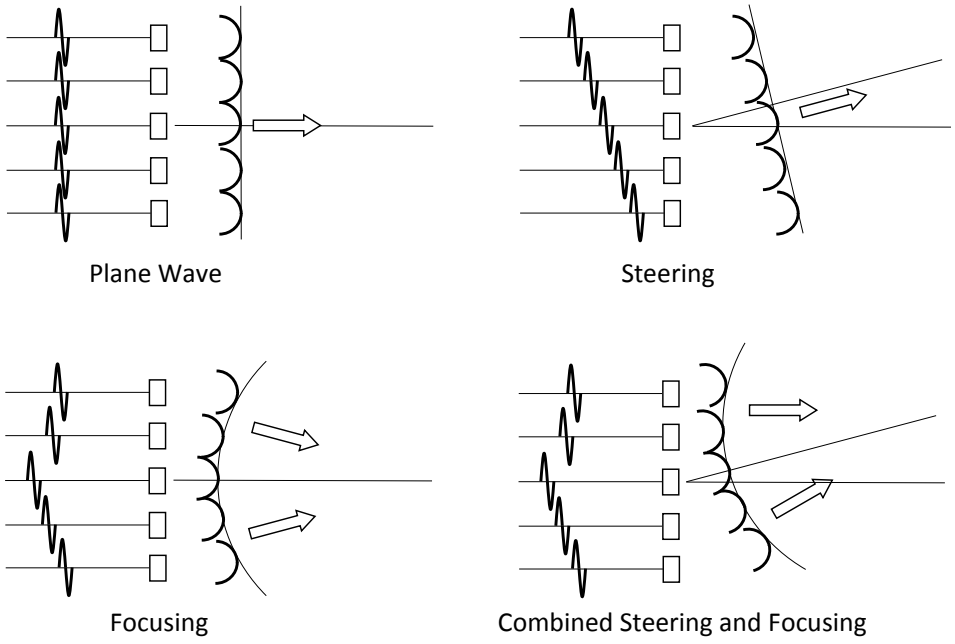

Figure 2.6: Schematic of beam steering and focusing.

2.1.4 Beamforming

In modern ultrasound scanners, the transmitted beams are shaped by using electronic-based time delays on multiple active elements in a group. Fig. 2.6 shows the basic operation of beam steering and focusing. In order to acquire a line in the B-mode image with a conventional sequential system, an active group of elements are programmed to transmit the acoustic beam where the interrogated line is at the centre. For a linear or curvilinear array transducer, once the previous echoes have been received by the same transducer, the next group of active elements are activated. The new group is formed by dropping one element at one side and adding a new element at the other side. This moves the group of active elements and hence the image line by one element. The whole region of interest (ROI) is swept by multiple transmissions and a full B-mode image is then formed. In contrast, all elements are employed for every transmission with a phased array transducer to maximise the lateral resolution due to an expanded aperture size. Every line in the polar coordinate system as shown in Fig. 2.3(b) is thus formed by combined beam steering and focusing with all elements as illustrated in Fig. 2.6.

2.1.5 Spatial Resolution

For 2-D ultrasound imaging, spatial resolution (Ng & Swanevelder, 2011) refers to the minimum distance that can be differentiated between two objects in the direction of the incident beam (axial resolution) or perpendicular to that (lateral resolution). Mathematically, axial resolution is equal to half the pulse length. Lateral resolution is predominantly determined by the transducer and transmission parameters, for sequential systems it can be improved by increasing the frequency of the wave or the aperture size for transmission.

2.1.6 Doppler Effect, Continuous Doppler, Pulsed Doppler and Doppler Aliasing

The Doppler effect can be observed in daily life as we might have noticed the changed tone of a buzzer when a car passes by. The tone of the buzzer changes due to the change of the sound frequency compared to the emitted frequency as illustrated in Fig. 2.7. When there is no motion between the source and the observer, the observed sound has the same frequency as the transmitted one. However, when the source is moving towards the observer, the wavefront will be more closely packed, resulting in a higher frequency. Conversely, a lower frequency is detected when the source is moving away. The change of the received frequency relative to the emitted sound is called Doppler shift and the amplitude of the Doppler shift is related to the relative velocity between the source and the observer. The Doppler shift Δf is quantitatively determined by

$$\Delta f = \frac{v}{c} f_0, \tag{2.1}$$

where v is the relative velocity between the source and the observer, and f_0 is the frequency of the originally transmitted sound.

The use of the Doppler shift of ultrasound waves can detect the velocity of blood or tissue. Either the continuous wave (CW) or the pulsed wave system can be employed to gather the Doppler shift and hence the velocity. For a CW Doppler system, the incident wave is emitted without interruption from a transmitter, and the reflected echo is captured with a separate sensor as the receiver. Only within the region where the transmit and receiving beams overlap, the ultrasound echo is acquired. The CW ultrasound systems are routinely used for accurately detecting the peak blood velocities

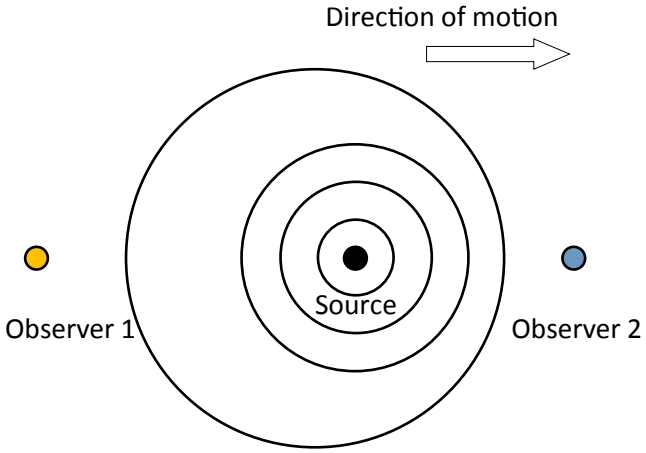

Figure 2.7: Illustration of the Doppler effect. The circular curves represent the wavefront.

especially in the stenosed vessels by analysing the spectrum of the Doppler signal with a sliding temporal window of approximately 10 ms. However, the spatial information indicating the location where these signals are picked up is missing with this technique.

Similar to fundamental B-mode imaging, the blood flow velocity can be depicted in 2-D space by using the pulsed transmission scheme. Short ultrasound pulses are transmitted and received with the same transducer, doubling the Doppler shift to

$$2\Delta f = \frac{2v}{c} f_0. \tag{2.2}$$

The pulse repetition frequency (PRF) determines how frequently the signal is sampled in each pixel for Doppler processing. Based on the Nyquist sampling theory, the Doppler shift that can be accurately detected will not be higher than a half of the PRF. If the signal is sampled infrequently, we get a phenomenon called Doppler aliasing, where we are measuring the wrong frequency and hence wrong velocity. The maximum detectable Doppler shift without aliasing for a given PRF (f_{PRF}) is

$$\Delta f_{\max} = \frac{2v_{\mathrm{zmax}}}{c} f_0 = \frac{f_{\mathrm{PRF}}}{2}, \tag{2.3}$$

where v_{zmax} is the maximum detectable velocity in the axial direction, and it is thus determined by

$$v_{\mathrm{zmax}} = \frac{c f_{\mathrm{PRF}}}{4 f_0}. \tag{2.4}$$

The number of samples for calculation of the Doppler shift is the ensemble (packet) size. In practice this number is in the range of 8 to 32, depending on the applications. The deeper the object or the faster the object is moving (such as a heart), the smaller the number. The short ensemble length hinders the ability to separate the blood signal and the tissue signal due to the difficulty of designing the FIR or IIR filter to operate on a short vector. Additionally, the short ensemble length imposes difficulties in the determination of the Doppler shift by spectral analysis due to the broadened bandwidth. Instead, the modern ultrasound pulsed-Doppler platforms measure the blood velocity through detecting the phase shift of the pulse. A technique termed 'autocorrelation' is prevalent in such platforms especially for colour Doppler imaging. Autocorrelation calculates the mean phase shift detected within each sample volume (normally a pixel), which is then transformed to display the amplitude and direction of the flow velocity. The axial velocity at each pixel v_z can be estimated by using the following equation (Kasai *et al.*, 1985)

$$v_z = \frac{cf_{PRF}}{4\pi f_0}\text{atan}\left(\frac{\sum_{i=1}^{N-1} I(i+1)Q(i) - Q(i+1)I(i)}{\sum_{i=1}^{N-1} I(i+1)I(i) + Q(i+1)Q(i)}\right), \tag{2.5}$$

where I and Q are in-phase and quadrature signals, and N represents the ensemble length. A duplex mode consisting of ultrasound Doppler and B-mode imaging is usually adopted in the clinic, allowing for a better location of the scanned region as shown in Fig. 2.8.

2.1.7 Colour Doppler Imaging with Broadband Signals

In colour Doppler imaging, there is a tradeoff between the spatial resolution and accuracy of velocity estimations. The use of a short ultrasound pulse increases the spatial resolution but broadens the spectrum of the incident wave, making the determination of the centre frequency of the echo (or incident wave) f_0 in Eq. 2.5 difficult. To tackle the problems arising from broadband Doppler signals, a 2-D autocorrelator was proposed (Loupas *et al.*, 1995). The centroids of the Doppler frequency $\langle f_d \rangle$ and centre frequency of the echo $\langle f_{RF} \rangle$ were first calculated using Eq. 2.6 and Eq. 2.7:

$$\langle f_d \rangle = \frac{f_{PRF}}{2\pi}\text{atan}\left(\frac{\sum_{j=1}^{M}\sum_{i=1}^{N-1} I(j,i+1)Q(j,i) - Q(j,i+1)I(j,i)}{\sum_{j=1}^{M}\sum_{i=1}^{N-1} I(j,i+1)I(j,i) + Q(j,i+1)Q(j,i)}\right), \tag{2.6}$$

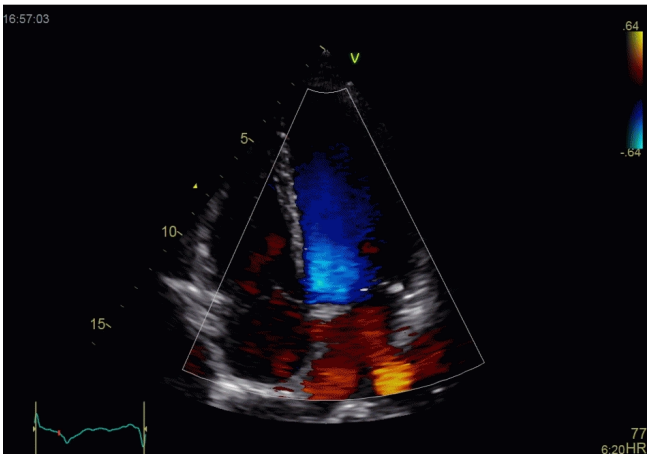

Figure 2.8: Example of duplex mode ultrasound imaging. Reproduced with permission from http://folk.ntnu.no/stoylen/strainrate.

$$\langle f_{\mathrm{RF}} \rangle = \frac{f_{\mathrm{s}}}{2\pi} \mathrm{atan} \left(\frac{\sum_{j=1}^{M-1} \sum_{i=1}^{N-1} I(j+1,i)Q(j,i) - Q(j+1,i)I(j,i)}{\sum_{j=1}^{M-1} \sum_{i=1}^{N-1} I(j+1,i)I(j,i) + Q(j+1,i)Q(j,i)} \right), \tag{2.7}$$

where f_{s} is the sampling frequency, and M is the length of the spatial range gate. Following these calculations, the axial velocity $v_{\mathrm{z_{2D}}}$ was determined by Eq. 2.8

$$v_{\mathrm{z_{2D}}} = \frac{c}{2} \frac{\langle f_{\mathrm{d}} \rangle}{\langle f_{\mathrm{RF}} \rangle}. \tag{2.8}$$

To investigate the effect of using different autocorrelators on the accuracy of estimation of the broadband Doppler signals, a rotating disk phantom (Harput *et al.*, 2013) was manufactured with a diameter of approximately 3 cm and rotated at 12π rad/s. The UARP II equipped a linear array transducer Prosonic L3-8 40EP was programmed to image the rotating disk by using zero-degree plane waves with a PRF of 5 kHz. Details about plane wave imaging can be found later in Section 2.3.1. This transducer owned a -6 dB bandwidth of 57% with a centre frequency of 5 MHz. The short negative pulses of 50 ns were employed to emanate plane waves with a broad bandwidth (MI = 1.0) and hence the corresponding Doppler signals are broadband.

Fig. 2.9 and Fig. 2.10 show colour Doppler images of the cross section of the rotating disk phantom when using the 1-D autocorrelator and 2-D autocorrelator, respectively. By considering Eq. 2.4 for Doppler estimation without aliasing, the maximum

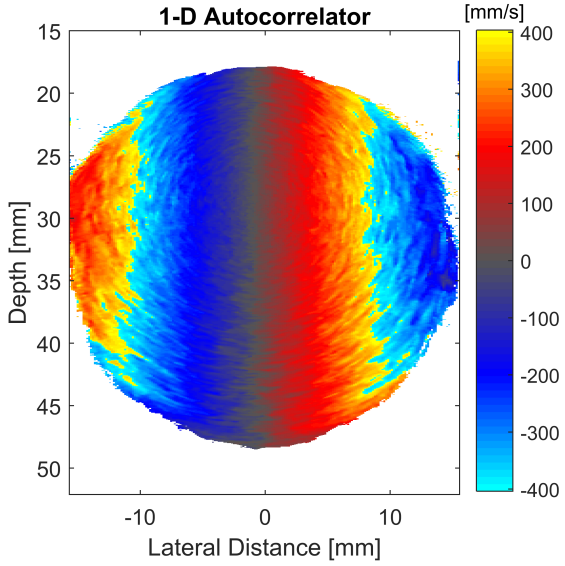

Figure 2.9: Colour Doppler image of the disk phantom rotated at 12π rad/s when using the 1-D autocorrelator. The Doppler ensemble length is 20.

detectable velocity is thus calculated to 385 mm/s for a centre frequency of 5 MHz. Doppler aliasing is noticeable in both Figs. 2.9 and 2.10, where the motion is heading in the opposite direction at regions with an axial velocity higher than the Nyquist limit. This happens because the sampling rate (f_{PRF}) is insufficient to decode the correct velocity information. Fig. 2.11 shows the locally estimated centre frequency $\langle f_{\mathrm{RF}} \rangle$, where considerable discrepancy is found between the guessed centre frequency of 5 MHz and the calculated centre frequencies in pixels. The effect of using a more accurate centre frequency is manifest in Figs. 2.9 and 2.10, with a smoother flow pattern in Fig. 2.10.

As will be shown in Section 2.2, microbubbles oscillate nonlinearly when impinged by ultrasonic waves, where broadband echoes are dominant. This poses problems on the accurate estimation of blood flow velocity when using microbubbles to improve the sensitivity of ultrasound Doppler. For broadband insonations, the 2-D autocorrelator has been shown to perform better in colour Doppler imaging, and is also anticipated to improve colour Doppler imaging with microbubbles.

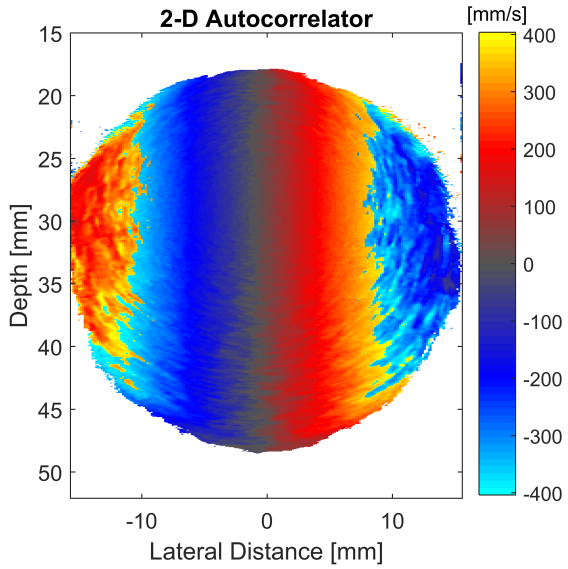

Figure 2.10: Colour Doppler image of the disk phantom rotated at 12π rad/s when using the 2-D autocorrelator. The Doppler ensemble length is 20, and the length of the range gate is 2 pixels.

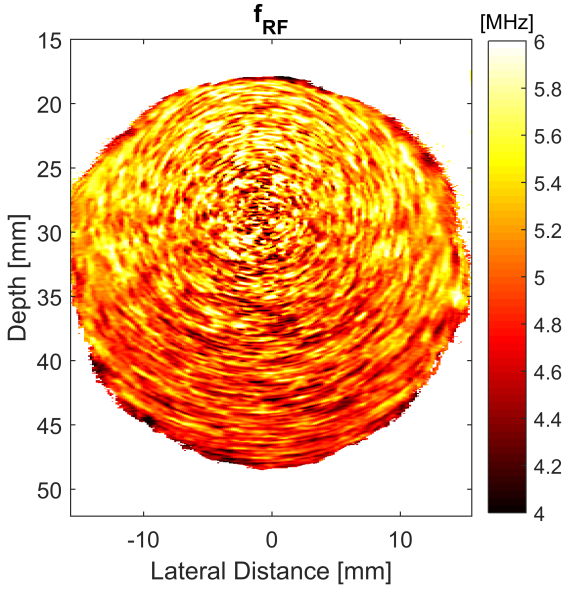

Figure 2.11: Local estimation of the centre frequency $\langle f_{\mathrm{RF}} \rangle$ of the echoes.

2.1.8 Advanced Blood Flow Measurement Techniques

Ultrasonic imaging underpins quantification of blood flow for many cardiovascular diseases which manifest strong flow abnormalities. Conventional colour Doppler imaging prevails in real-time operation but is confined by fundamental limitations such as angle-dependence and aliasing (Jensen & Munk, 1998). Angle dependence and aliasing could be partially approached by angle correction and shifting the Doppler frequency baseline, respectively (Gill, 1985). But the following-up monitoring of disease progression is hampered due to large inter-operator variations when correcting the beam-to-flow angle.

More intuitive and accurate angle-independent 2-D blood flow imaging methods have been suggested varying from transverse oscillation (Udesen & Jensen, 2006) and vector Doppler (Dunmire *et al.*, 2000) to speckle tracking (Bohs *et al.*, 2000) and echo particle image velocimetry (Kim *et al.*, 2004). These can be categorized into Doppler-based and non-Doppler-based techniques.

It is well known that velocity can be estimated according to the Doppler shift as adopted by conventional Doppler imaging and it is rational to generate the oscillation field along the transverse direction to reconstruct 2-D flow maps. This concept named transverse oscillation has been introduced by Jorgen Arendt Jensen (Jensen & Munk, 1998), and implemented in commercial platforms using the conventional line-by-line mode with a frame rate limited to approximately 20 Hz. As there is a Fourier relationship between the apodization function and beam pattern in the far field or at the focus, a sinusoidal pattern can be formed along the transverse direction by manipulating the receive apodization function applied to the aperture. A phase-based estimator was developed to decode the 2-D velocity components.

Cross-beam vector Doppler uses 1-D velocities from two angles to derive the velocity vector (Tortoli *et al.*, 2006). The geometric relationship of these two angles holds the core of this method, and the inaccurate estimation along one direction would significantly bias the overall estimation. To minimise the variance due to the inaccurate estimation from one direction, an over-determined structure by using multiple angles was developed, with the two velocity components estimated by using least squares fitting (Yiu *et al.*, 2014).

As the early effort of non-Doppler-based techniques to render 2-D vector velocities, speckle tracking algorithms were proposed in the late 1980s (Meunier *et al.*, 1988). With the assumption of the relatively stable speckle pattern from the blood cells over a short interval, the average motion field can be calculated with a series of speckle images by using cross correlation. However, the utility of this technique is confined by the low SNR of the echoes from blood cells. The image SNR could become high enough to portray blood flow when microbubble contrast agents are introduced into the blood stream, with microbubbles faithfully tracking the flow pattern. This concept stimulates the development of echo particle image velocimetry (Kim *et al.*, 2004), where the velocity estimation basically relies on the calculation of displacement of interrogation windows by using cross correlation. Given the highest correlation peak position and the time interval between the interrogated images, the averaged velocity is obtained. For the sake of computational efficiency, the calculation of cross correlation as given by Eq. 2.9 can be replaced by the FFT-based method in the frequency domain (Eqs. 2.10 and 2.11).

$$\Phi(m,n) = \sum_i \sum_j f_{\mathrm{k}}(i,j) g_{\mathrm{k}}(i+m, j+n), \tag{2.9}$$

where Φ denotes the coefficient map of cross correlation, f_{k} and g_{k} are two kernels in two frames, m and n are the integer pixel offsets (both are zero for echo particle image velocimetry).

$$\Phi(m,n) = f_{\mathrm{k}}^{\star}(-m,-n) * g_{\mathrm{k}}, \tag{2.10}$$

Based on the convolution theorem, Eq. 2.10 can be changed to:

$$\Phi(m,n) = \mathrm{iFFT}(\mathrm{FFT}^{\star}(f_{\mathrm{k}})\mathrm{FFT}(g_{\mathrm{k}})), \tag{2.11}$$

where $\star$ indicates the complex conjugate, $*$ is the convolution operation, FFT denotes the fast Fourier transform, and iFFT is the inverse fast Fourier transform.

As integer pixel displacements are not guaranteed, a Gaussian interpolation method is normally employed to fit the correlation peak, enabling a subpixel estimation accuracy as illustrated by Eqs. 2.12 and 2.13 (Niu *et al.*, 2009).

$$\Delta I_{\mathrm{p}} = \frac{\ln[\Phi(I_{\mathrm{p}}-1, J_{\mathrm{p}})] - \ln[\Phi(I_{\mathrm{p}}+1, J_{\mathrm{p}})]}{2\ln[\Phi(I_{\mathrm{p}}-1, J_{\mathrm{p}})] - 4\ln[\Phi(I_{\mathrm{p}}, J_{\mathrm{p}})] + 2\ln[\Phi(J_{\mathrm{p}}+1, J_{\mathrm{p}})]}, \tag{2.12}$$

$$\Delta J_{\mathrm{p}} = \frac{\ln[\Phi(I_{\mathrm{p}}, J_{\mathrm{p}} - 1)] - \ln[\Phi(I_{\mathrm{p}}, J_{\mathrm{p}} + 1)]}{2\ln[\Phi(I_{\mathrm{p}}, J_{\mathrm{p}} - 1)] - 4\ln[\Phi(I_{\mathrm{p}}, J_{\mathrm{p}})] + 2\ln[\Phi(I_{\mathrm{p}}, J_{\mathrm{p}} + 1)]}, \tag{2.13}$$

where I_{p} and J_{p} are integer pixel coordinates at which the maximum cross correlation coefficient is reached, ΔI_{p} and ΔJ_{p} are the subpixel estimations relative to I_{p} and J_{p}, respectively.

All Doppler-based vector flow mapping techniques are prone to aliasing. Cross-beam vector Doppler can be performed within a region where cross beams overlap, limiting the application of this method to shallow regions. For the transverse component when using the transverse oscillation method, the estimation accuracy could be biased by the inaccurate prediction of the lateral wavelength which is obtained based on the apodization function. Though it is still challenging to portray turbulent flow due to its 3-D nature, non-Doppler-based methods such as echo particle image velocimetry enable aliasing-free 2-D flow imaging, which could provide good insight into abnormal flow patterns especially in the heart.

2.1.9 Nonlinear Propagation

A constant speed of sound in the medium is used to approximate the reality when the acoustic pressure is low. Nevertheless, this assumption is challenged when the amplitude of the pulse is large (>1 MPa) due to two reasons (Leighton, 2007). For the first instance, the speed of sound varies with the properties of the medium such as its stiffness. A positive pressure compresses the medium, locally increasing the stiffness and hence the speed of sound. Otherwise, a negative pressure rarefies the medium, decreasing the stiffness of the medium and hence the speed of sound locally. Additionally, the velocity of particles induced by medium compression or rarefaction interferes with the transmitted wave propagating through the medium. In the compressed region with a positive acoustic pressure, the particle motion is in line with the direction of wave propagation, giving an increase in phase speed. Whereas in the rarefied region, particles move in the opposite direction of the incident beam, where a decrease in phase speed is induced. In the temporal domain, the transmitted pulse is intuitively distorted with the positive parts being narrower and the negative parts being stretched as shown in Fig. 2.12 (a). The distortion of the pulse is also visible in the frequency domain, with high frequency components appearing at the multiples of the original frequency, termed

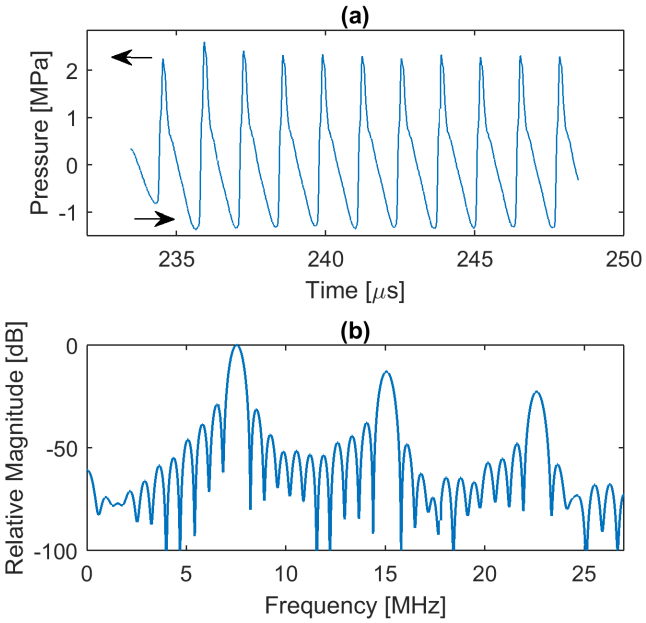

Figure 2.12: A gated pulse waveform captured by a 200-μm needle hydrophone is shown in (a), with its corresponding spectrum shown in (b). The pulse waveform has a centre frequency of 7.55 MHz.

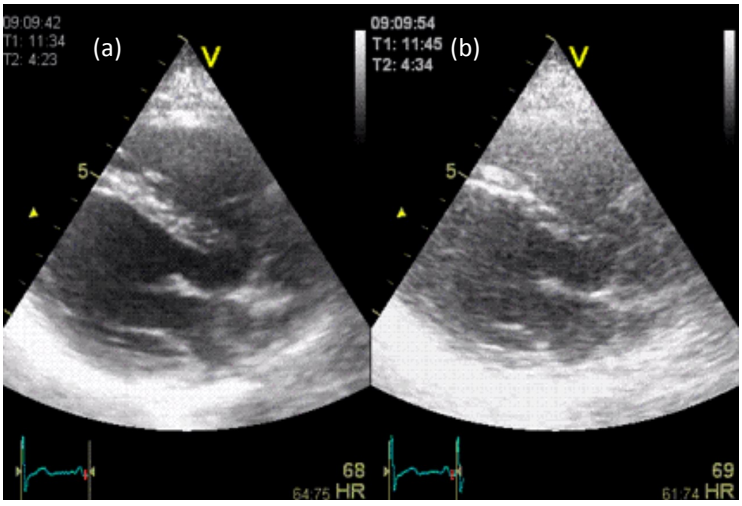

Figure 2.13: Parasternal long axis view of a heart: (a) harmonic-mode image and (b) fundamental B-mode image. Reproduced with permission from http://folk.ntnu.no/stoylen/strainrate.

harmonics. Nonlinear propagation gives rise to the energy transfer from the fundamental frequency f_0 to multiple harmonics such as $2f_0$ and $3f_0$ as shown in Fig. 2.12 (b). In medical ultrasound imaging, the use of high-order harmonics has long been investigated to increase the image resolution. Reducing the imaging artefacts such as clutter noise is widely adopted using tissue harmonics (Averkiou, 2001) as shown in Fig. 2.13. The second tissue harmonic is predominately employed in clinical scanners due to the limited bandwidth of the transducer and higher attenuation of higher-order harmonics.

2.2 Contrast-Enhanced Medical Ultrasound with Microbubbles

In addition to nonlinear propagation, the vibration of microbubbles can be extremely nonlinear, when subject to an ultrasonic field even with low-level acoustic pressures (MI < 0.12) (Toulemonde *et al.*, 2018), where the tissue response is largely linear. The reason of the microbubble nonlinearity is mainly because of the nonlinear vibration of the microbubble shell in response to the positive and negative pressures. During the phase of negative pressures, microbubbles easily expand, but they gradually become less compressible in response to positive parts of the ultrasound wave as shown in Fig. 2.4(b). In the frequency domain, the microbubble nonlinearity appears with the presence of multiple harmonics such as $2f_0$ and even the subharmonic at $f_0/2$ if the applied pressure is above a threshold to elicit it (McLaughlan *et al.*, 2017). It is normally accepted that the MI or PNP accounts for microbubble destruction (McLaughlan *et al.*, 2017), as microbubbles expand to collapse in response to a high level of PNPs.

The nonlinear response of microbubbles at low MI enables real-time detection of them in both large vessels and microcirculation. This stimulates a large amount of tissue perfusion studies especially for myocardium (Kaul, 1998), where differentiating slow-moving microbubbles from the fast-moving tissue background is achieved. The second harmonic and superharmonics are exploited to increase the CTR, and this can be done by using band-pass filtering or multi-pulse nonlinear imaging schemes (Eckersley *et al.*, 2005). Compared against the bandpass filtering method, multi-pulse imaging techniques allow for the use of wide-band pulses, where spatial resolution can be optimised. Whereas for bandpass filtering, a narrow-band excitation signal should be employed, where the spatial resolution is compromised.

A number of multi-pulse strategies have been developed to efficiently enhance the sensitivity of nonlinear imaging of microbubbles, such as PI (Simpson *et al.*, 1999), AM (Frinking *et al.*, 2000), pulse inversion amplitude modulation (PIAM) (Eckersley *et al.*, 2005) and CPS (Phillips, 2001), among others. Figs. 2.14−2.17 show schematic illustrations of pulsing for PI, AM, PIAM and CPS, respectively. In PI, two consecutive ultrasound pulses with the opposite polarities are transmitted and the corresponding echoes are summed to cancel out the fundamental frequency with the second harmonic highlighted. For AM, two consecutive ultrasound pulses are transmitted, with the first pulse transmission having a full amplitude and the second one having a half amplitude. The echo from the full-amplitude transmission and twice of the sign-inverted echo from the half-amplitude transmission are then combined. Both phase and amplitude modulation are employed in PIAM and CPS, where both even and odd harmonics can be preserved. In PIAM, the only difference to AM is that the second pulse transmission is inverted with a phase shift of π. Three pulse transmissions are used in CPS. First, a half-amplitude pulse is transmitted, then a full-amplitude pulse of inverted polarity is fired followed by the emission of another half-amplitude pulse. For a CPS image, echoes from the three pulse transmissions are summed.

The effort for understanding the underlying theory of these multi-pulse imaging schemes was seen by modelling the nonlinear microbubble echo as a polynomial expansion of a basis waveform (Eckersley *et al.*, 2005).

$$O(x(t)) = a_1 x(t) + a_2 x^2(t) + a_3 x^3(t) + ... + a_i x^i(t), \tag{2.14}$$

where O is the reflected echo and $x(t)$ is the basis function. The coefficient a_i denotes the contribution of a specific-order harmonic. By considering an ultrasound basis function $x(t) = \cos(wt)$, then:

$$x^2(t) = \frac{1}{2}[1 + \cos(2wt)], \tag{2.15}$$

$$x^3(t) = \frac{1}{4}[\cos(wt) + \cos(3wt)], \tag{2.16}$$

$$x^4(t) = \frac{1}{8}[3 + 4\cos(2wt) + \cos(4wt)]. \tag{2.17}$$

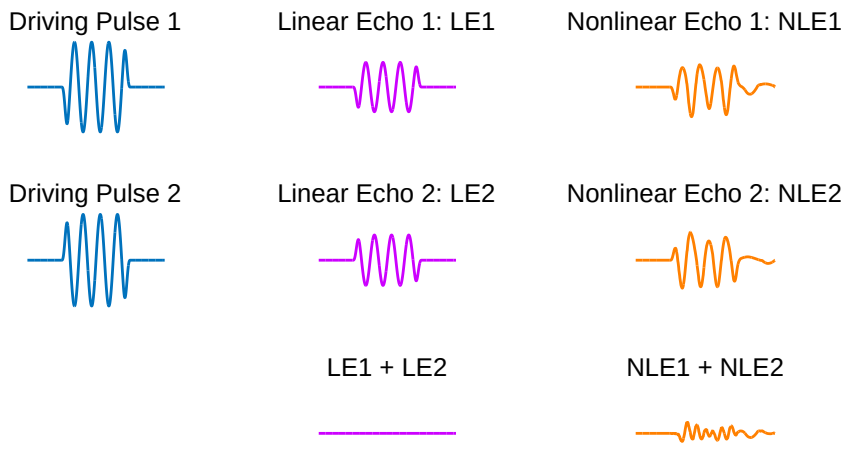

Figure 2.14: Schematic of PI sequencing. Driving Pulse 1 = (−Driving Pulse 2), and these two pulses are transmitted sequentially. The summation of their corresponding echoes is zero for linear targets, whereas residual signals remain for microbubbles.

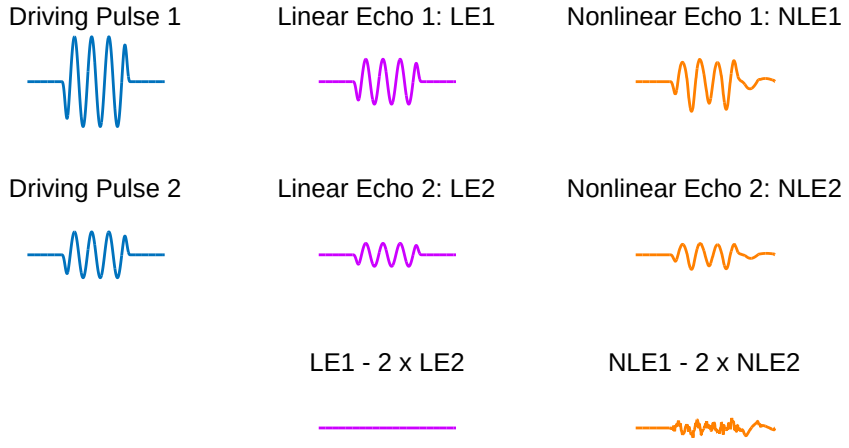

Figure 2.15: Schematic of AM sequencing. Driving Pulse 1 = (2 x Driving Pulse 2), and these two pulses are transmitted successively. The echo from the second pulse is doubled before subtracted by the echo from pulse 1, removing the linear echo.

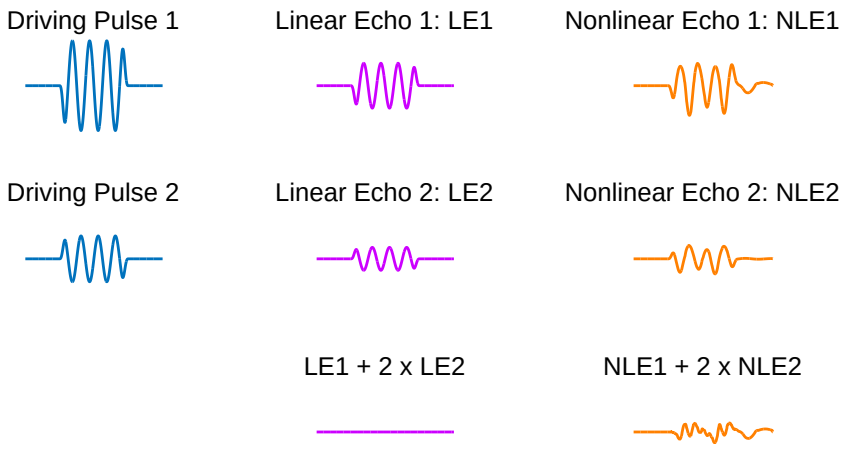

Figure 2.16: Schematic of PIAM sequencing. Driving Pulse 1 = (−2 x Driving Pulse 2). The amplitude difference of the echoes is compensated by scaling up the second echo with a factor of 2 before summing them together.

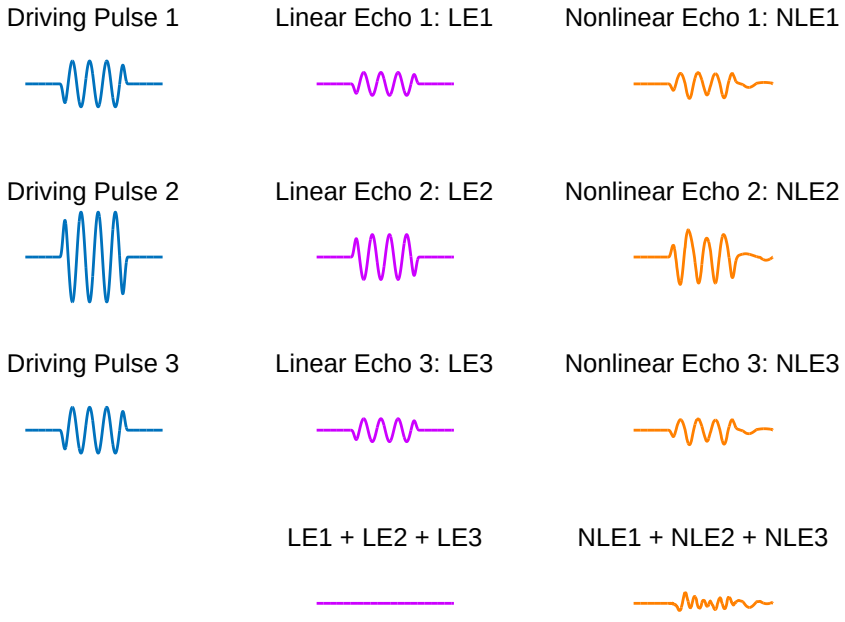

Figure 2.17: Schematic of CPS sequencing. Driving Pulse 2 = (−2 x Driving Pulse 1) = (−2 x Driving Pulse 3). All echoes from three pulse transmissions are summed to cancel the linear component.

By considering $-x(t) = -\cos(wt)$ and neglecting harmonics above the third order, $O(x(t)) + O(-x(t)) = 2a_2x^2(t)$. This explains the underlying mechanism for PI, where the second-order harmonic is preserved. For AM, $O(2x(t)) - 2O(x(t)) = 2a_2x^2(t) + 6a_3x^3(t)$, where both odd-order and even-order harmonics can be highlighted. By modulating both phase and amplitude for PIAM, $O(2x(t)) + 2O(-x(t)) = 6a_2x^2(t) + 6a_3x^3(t)$. For CPS, $O(x(t)) + O(-2x(t)) + O(x(t)) = 6a_2x^2(t) - 6a_3x^3(t)$. When taking Eqs. 2.15−2.17 into consideration, the second harmonic is dominant in PI, and both the second harmonic and nonlinear fundamental component are preserved in AM, PIAM and CPS. AM, PIAM and CPS prevail in providing a higher CTR when compared to PI, as the nonlinear signal can be received at the fundamental frequency band, where the impact of acoustic attenuation is less significant. The use of AM, PIAM and CPS also looses the requirement of a broadband transducer that is used for second harmonic imaging. However, the drawbacks of this simplified model are the neglected effects of the shell composition, microbubble size and acoustic pressure on the microbubble response.

The field of single-microbubble simulation is maturing with a number of models proposed to describe the dynamics of a single microbubble under ultrasound stimulations. The story starts from modelling an air bubble in liquids with the well-established Rayleigh-Plesset-Noltingk-Neppiras-Poritsky (RPNNP) equation (Hasson *et al.*, 2016):

$$\rho_{\mathrm{L}}\left(R\ddot{R} + \frac{3}{2}\dot{R}^2\right) = \left(P_0 + \frac{2\sigma}{R_0}\right)\left(\frac{R_0}{R}\right)^{3\gamma} - \frac{2\sigma}{R} - \frac{4\mu\dot{R}}{R} - p_\infty, \tag{2.18}$$

where ρ_{L} is the density of the liquid, R is the bubble radius as a function of time, $\dot{R}$ is the bubble wall velocity, $\ddot{R}$ is the bubble wall acceleration, σ is the surface tension between the liquid and bubble surface, R_0 is the equilibrium radius, γ is the polytropic index, μ is the viscosity of the liquid (water), and p_∞ is the pressure at infinity.

p_∞ is defined as:

$$p_\infty = P_0 + P_{\mathrm{drive}}(t), \tag{2.19}$$

where P_0 is the hydrostatic pressure, and $P_{\mathrm{drive}}(t)$ is the driving acoustic pressure.

Incorporating the shell properties into the model is required when modelling the coated microbubbles. The Sarkar model (Chatterjee & Sarkar, 2003) extends the RPNNP equation by adding the dilatational viscosity of the shell κ_S as follows:

Table 2.3: Simulation Parameters: Marmottant Model

Parameter	Value
R_0	2 μm
$P_{\text{drive}}(t)$	10 μs sinusoid (2 MHz)
P_0	101325 Pa
ρ_{L}	998 kg/m^3
σ	0.0728 N/m
γ	1.095
μ	0.001 Pa·s
κ_S	6 x 10^{-9} Pa·m·s
χ	0.3 N/m
d	1 cm

$$\rho_{\text{L}}\left(R\ddot{R}+\frac{3}{2}\dot{R}^2\right)=\left(P_0+\frac{2\sigma}{R_0}\right)\left(\frac{R_0}{R}\right)^{3\gamma}-\frac{2\sigma}{R}-\frac{4\mu\dot{R}}{R}-\frac{4\kappa_S\dot{R}}{R^2}-p_\infty. \tag{2.20}$$

Eq. 2.20 is further improved to describe the surface tension as a function of the microbubble radius, forming the Marmottant model (Marmottant *et al.*, 2005) as follows:

$$\rho_{\text{L}}\left(R\ddot{R}+\frac{3}{2}\dot{R}^2\right)=\left(P_0+\frac{2\sigma(R_0)}{R_0}\right)\left(\frac{R_0}{R}\right)^{3\gamma}-\frac{2\sigma(R)}{R}-\frac{4\mu\dot{R}}{R}-\frac{4\kappa_S\dot{R}}{R^2}-p_\infty, \tag{2.21}$$

The surface tension $\sigma(R)$ between the liquid and microbubble shell varies with the microbubble radius and can be described by Eq. 2.22.

$$\sigma(R)=\begin{cases}0 & \text{if } R\le R_{\text{buckling}}\\ \chi\left(\dfrac{R^2}{R_{\text{buckling}}^2}-1\right) & \text{if} R_{\text{buckling}}\le R\le R_{\text{rupture}}\\ \sigma & \text{if } R\ge R_{\text{rupture}}\end{cases} \tag{2.22}$$

where $R_{\text{buckling}}=R_0$, $R_{\text{rupture}}=R_0\sqrt{1+\sigma/\chi}$, and χ denotes the shell elasticity.

The nonlinear imaging schemes were then investigated by using the Marmottant model with similar parameters as used in (Eckersley *et al.*, 2005) (Table. 2.3). The

dynamics of the microbubble radius were first solved by using Eq. 2.21, followed by the calculation of the pressure response P_{MB} radiated from the microbubble at a distance d by using Eq. 2.23:

$$P_{\mathrm{MB}} = \frac{\rho_{\mathrm{L}}}{d}(R^2\ddot{R} + 2R\dot{R}^2). \tag{2.23}$$

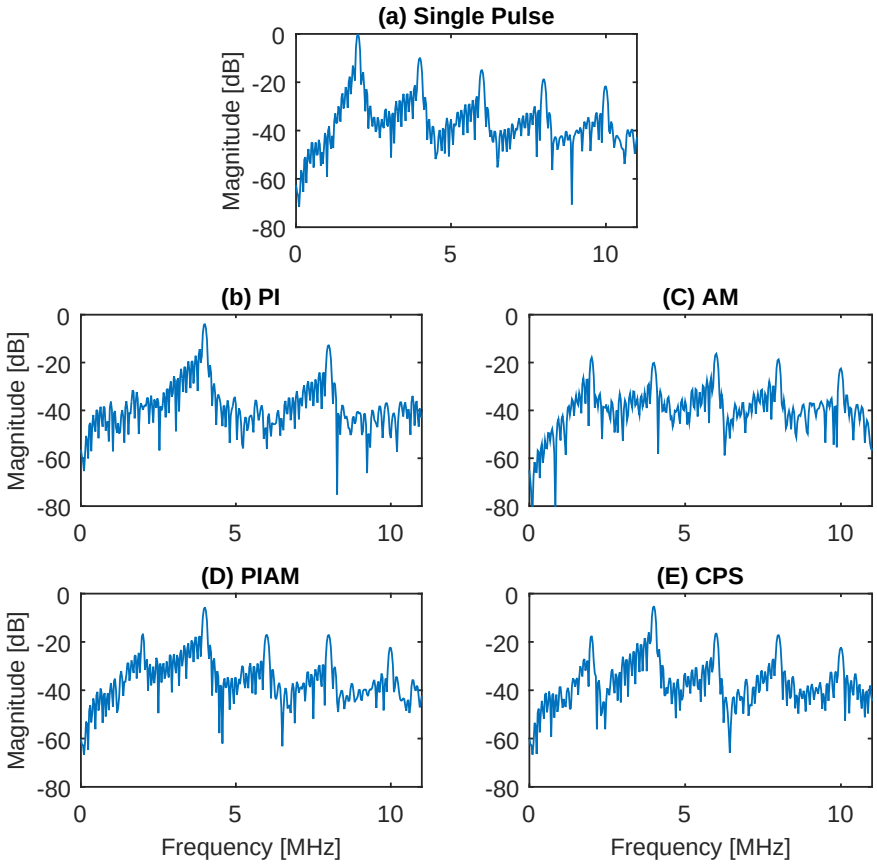

Figure 2.18: Scattered spectra from a microbubble for different pulsing schemes with simulation parameters given in Table 2.3. PNP = 130 kPa. All curves are normalized to the peak value in (a).

The simulated spectra of microbubble responses for all pulsing schemes are shown in Fig. 2.18. All curves were normalized to the peak value for the single pulse. The results show that only the even-order harmonics are preserved with PI. The nonlinear

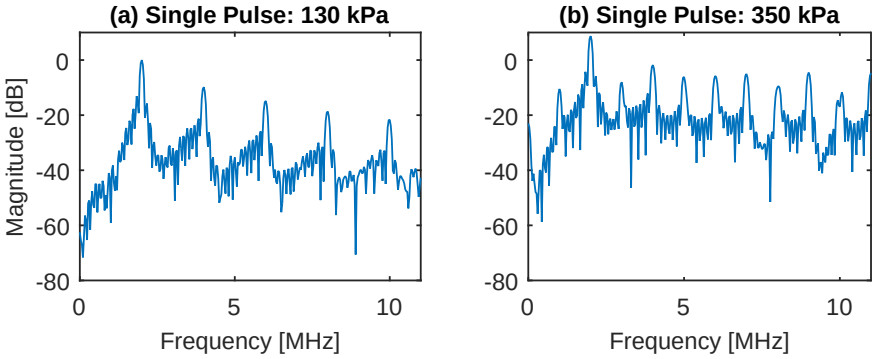

Figure 2.19: Scattered spectra from a microbubble for different PNPs with simulation parameters given in Table 2.3. (a) PNP: 130 kPa. (b) PNP: 350 kPa. All curves are normalized to the peak value in (a).

component resides within the fundamental band when using AM, PIAM and CPS. Compared against AM, the second harmonic is more manifest with PIAM and CPS.

The subharmonic at $f_0/2$ is absent from tissue at diagnostic pressure levels, while encapsulated microbubbles suspended in fluid could backscatter the subharmonic of the incident frequency, when the applied acoustic pressure exceeding a threshold to generate Faraday waves on the bubble surface (Leighton *et al.*, 1996; Shankar *et al.*, 1998). A simulation based on the Marmottant model was performed to show the generation of the subharmonic which cannot be explained by the model in (Eckersley *et al.*, 2005). The scattered spectra for two different PNPs are shown in Fig. 2.19. The curves were normalized to the maximum for the PNP of 130 kPa, where no subharmonic components are visible. For a PNP of 350 kPa, the subharmonic ($f_0/2$) and ultraharmonics ($3f_0/2$, $5f_0/2$, $7f_0/2$ ...) are visible. Compared to ultraharmonics, the effect of acoustic attenuation is less significant for the subharmonic, where the penetration depth can be improved.

The use of high-order microbubble responses ($3f_0$, $4f_0$ ...) has spawned an area of acoustic angiography (Gessner *et al.*, 2010) for high-contrast and high-resolution ultrasound imaging. A dual-frequency transducer was used, with the low-frequency elements exciting the microbubbles near their resonance, and the high-frequency elements picking up the emitted high-frequency content from them. However, the use of superharmonics is confined for shallow regions due to the extremely high attenuation for high frequencies.

2.3 HFR Medical Ultrasound Imaging Using Parallel Systems

The recent engineering advancements in the development of parallel ultrasound research platforms (Boni *et al.*, 2017, 2018), such as arbitrary waveform generation on each channel, have triggered a new era with the emergence of techniques allowing for ultrahigh temporal resolution (Montaldo *et al.*, 2009) or spatial resolution (Errico *et al.*, 2015). Instead of using sequential focused beams to form the image line by line, a B-mode image can be reconstructed by transmitting a single plane/diverging wave and the image contrast and resolution can be improved at the receiving side by coherent summation of echoes from multiple transmissions (Montaldo *et al.*, 2009). Apart from shear wave elastography, the advent of HFR plane/diverging wave imaging proved especially beneficial for capturing transient flow patterns which was never readily achievable before. The renewed interest in colour Doppler imaging (Osmanski *et al.*, 2011), and particularly 2-D vector flow mapping (Hoyos *et al.*, 2016; Lenge *et al.*, 2015; Leow *et al.*, 2015) has been seen by using HFR ultrasound techniques.

2.3.1 Plane Wave Imaging

Crucial to plane wave imaging is beamforming for both transmission and receiving which will be described in detail (Montaldo *et al.*, 2009). The advantage of this technique is that it does not necessitate the sequential sweeping of the ROI line by line. This enables an extreme high frame rate up to 25 kHz for a depth of 3 cm (speed of sound: 1540 m/s). By no means is it without limitations. As there is no transmission focus, the image resolution and contrast are only obtained by parallel processing of echoes from the same scatter. Fig. 2.20(a) shows the straightforward zero-degree plane wave scenario when simultaneously firing all the elements. The wave is backscattered by the imaged medium and every element of the array receives the echo. The wave travels to the point (x, z) with time z/c. The time delay for the scattered wave back to a specific element located at x_1 is then calculated with $(\sqrt{z^2 + (x - x_1)^2})/c$. For an image point (x, z), the contributions from all channels (Moubark *et al.*, 2016) or a dynamic aperture with a fixed f number (Montaldo *et al.*, 2009) can be coherently summed. The f number is the ratio of the focal depth (z in this case) to the aperture size. The fixed f number is used to maintain the lateral resolution over space, with compromised

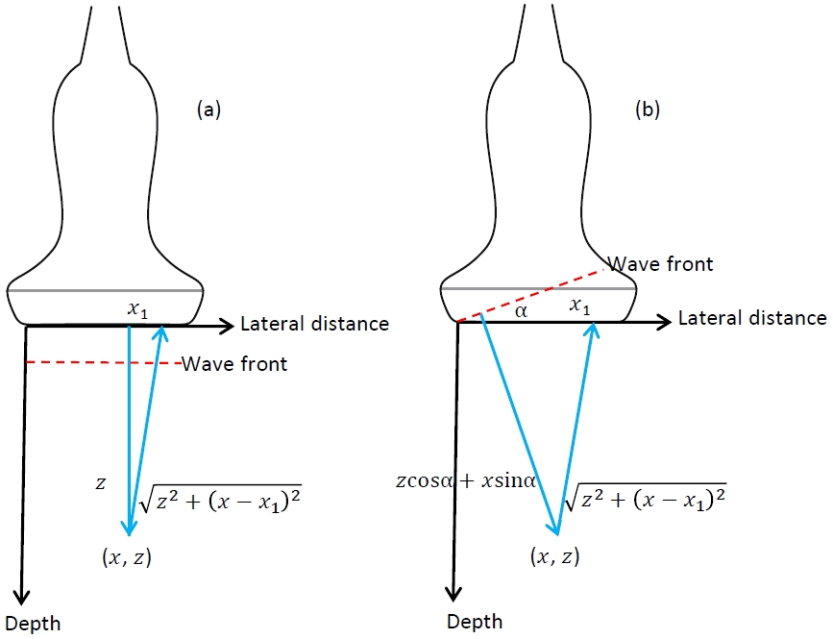

Figure 2.20: Schematic of the travelling distances to a point $(x,\ z)$ and back to an element x_1 for (a) a zero-degree plane wave, and (b) a steered plane wave with an angle of α.

performance especially at the shallow regions. When a steered plane wave is emitted, only the travelling distance to the point (x, z) and the time delay $(z\cos\alpha + x\sin\alpha)/c$ are different as shown in Fig. 2.20(b). By coherent compounding of images from different steered plane waves, the image resolution, contrast and SNR can be improved at the cost of the reduced frame rate.

2.3.2 Diverging Wave Imaging

Echocardiography is indispensable to the study of cardiac function. The non-ionising nature of ultrasound is ideal for repetitive scanning scenarios. Intriguing innovations have also been proposed by using diverging waves for HFR echocardiography (Fadnes *et al.*, 2017; Grondin *et al.*, 2017; Hasegawa & Kanai, 2011; Osmanski *et al.*, 2014; Papadacci *et al.*, 2014; Toulemonde *et al.*, 2016). By strategically placing virtual sources behind the surface of a phased array transducer, diverging waves can be formed to insonify a large field of view as needed for cardiac imaging. The use of the whole aperture for diverging wave transmissions (Poree *et al.*, 2016) is considered in this

thesis, and the schematic of the emission of a diverging wave from a phased array transducer is shown in Fig. 2.21.

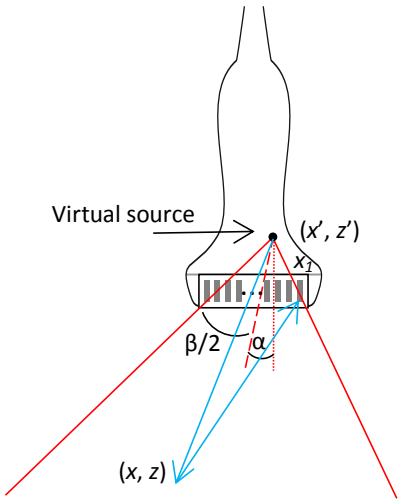

Figure 2.21: Schematic of the emanation of a diverging wave with the full aperture of a phased array transducer. α is the steering angle. β is the divergent angle and unchanged for coherent compounding. x_1 is the address of one element.

The position of the virtual source (x', z') is determined by the divergent angle β and steering angle α, as formulated by:

$$x' = \frac{A_{\text{diverging}}}{2} \frac{\tan(\alpha - \frac{\beta}{2}) + \tan(\alpha + \frac{\beta}{2})}{\tan(\alpha + \frac{\beta}{2}) - \tan(\alpha - \frac{\beta}{2})} \tag{2.24}$$

$$z' = -\frac{\frac{A_{\text{diverging}}}{2} + x'}{\tan(\alpha + \frac{\beta}{2})} \tag{2.25}$$

where $A_{\text{diverging}}$ is the physical aperture size for emanating the diverging wave.

The circular wave originating from the virtual source arrives at a point (x, z) with the time delay $\sqrt{(x' - x)^2 + (z' - z)^2}/c$. Then the reflected echo goes back to an element x_1 with the time of $\sqrt{(x - x_1)^2 + z^2}/c$. For each individual image point, the contributions from all channels are delayed and summed. To improve the image contrast and resolution, multiple steered diverging waves can be fired to facilitate coherent diverging wave imaging.

The beamforming method explained above, that is called delay-and-sum, is the most popular one for ultrasound imaging using unfocused beams including plane and diverg-

ing waves. The past decade has seen numerous efforts in developing advanced beamforming algorithms to further improve the image resolution and contrast. Of particular interest are minimum variance adaptive beamforming (Asl & Mahloojifar, 2009), filtered delay and sum (Matrone *et al.*, 2015), coherence-based beamforming (Hyun *et al.*, 2018; Li & Dahl, 2015), and machine learning-based beamforming (Gasse *et al.*, 2017). The improved image quality using these advanced beamforming algorithms usually comes with a higher computational cost. The effects of these beamforming algorithms on velocity estimation including 2-D vector flow mapping are still largely unknown.

2.3.3 HFR Contrast-Enhanced Ultrasound

The combination of microbubble contrast agents and HFR ultrasound imaging has emerged recently. Originally, it was investigated for the depiction of transient microbubble disruption (Couture *et al.*, 2009) afforded by the HFR imaging capability. It was then demonstrated that for the similar image quality, the application of HFR plane wave imaging could reduce microbubble destruction by combining multiple low-pressure transmissions and coherent summation (Couture *et al.*, 2012). Detecting microvascular abnormalities has the potential for the diagnosis of organ dysfunction at a very early stage. The combination of microbubbles and HFR ultrasound imaging has also driven the improvement of ultrasound Doppler and perfusion imaging (Tremblay-Darveau *et al.*, 2014, 2016a,b). The techniques of HFR contrast-enhanced 2-D vector flow mapping are also proliferating (Leow *et al.*, 2015). More recently, the diffraction limit in ultrasound imaging has been breached by localising single microbubbles. A super-resolved image can be constructed by accumulating multiple single microbubbles within thousands of images using plane waves, providing unsurpassed resolution for quantification of brain function (Errico *et al.*, 2015) and tumour (Lin *et al.*, 2017). With a 1-D array, ultrasound super-resolution imaging is confined within 2-D space. Research efforts are being devoted to the development of 3-D super-resolution ultrasound imaging with either a fully-addressed 2-D matrix array (Heiles *et al.*, 2017) or a sparse 2-D matrix array (Harput *et al.*, 2018). HFR contrast-enhanced ultrasound using diverging waves has been used for capturing transient flow patterns in heart chambers and quantification of myocardial perfusion (Toulemonde *et al.*, 2017a). The improved contrast ratio (CR) and contrast-to-noise (CNR) were reported compared against those

obtained with focused beams (Toulemonde *et al.*, 2018). By using singular value decomposition (SVD) and the large amount of data provided by HFR contrast-enhanced ultrasound, new avenues have been opened up for selectively separating microbubble signals without the use of nonlinear imaging schemes (Desailly *et al.*, 2016). Instead, it relies on the signal coherence both in space and time. Originally, this eigen-based filtering technique was applied to colour Doppler imaging to differentiate slow blood flow from tissue motion where conventional high-pass filtering methods have difficulties (Demené *et al.*, 2015). The tissue signal typically has a higher intensity and is more spatiotemporally coherent than flowing microbubbles. The assumption made when using SVD for separating microbubble signals is that the tissue background occupies the low-order singular vectors, microbubbles occupy the middle-order singular vectors, and noise is represented by the rest of the vectors. But the problem intrinsic to the SVD-based filtering technique is the proper selection of eigen-vectors, which is currently realized manually as done in (Nie *et al.*, 2018b). To suppress the tissue echo and noise but without affecting the microbubble echoes, the eigen-vectors can be selected as ones with eigenvalues above or below a predefined energy value (Yu & Lovstakken, 2010). But an absolute threshold for all *in vivo* scenarios does not exist.

A machine learning method based on k-means clustering could be employed for finding hidden patterns behind the singular vectors calculated from the given HFR ultrasound dataset. Groups or clusters are partitioned in such a way that the objects within a group have a higher similarity than objects in other groups. For the algorithm k-means clustering, the dataset is grouped into k distinct clusters based on data similarity by measuring the Euclidean distance to the centroid of a cluster (`https://uk.mathworks.com/help/stats/k-means-clustering.html`).

An experiment was performed to test the feasibility of clustering singular values for imaging microbubbles. Briefly, SonoVue microbubble solutions (1:3000) with an average speed of 15.2 cm/s were flowed through a wall-less flow phantom. The 2.8-mm flow channel was positioned at the depth of 35 mm. The impinging zero-degree plane waves (2 cycles, 7.55 MHz) were repeated with a PRF of 3 kHz, and a MI of 0.15 was used. As one example, an ensemble size of 30 was employed with the corresponding singular value distribution shown in Fig. 2.22. This 1-D data array was then fed into the k-means clustering algorithm with $k = 3$. This value was determined as three clusters of singular vectors are expected to represent tissue, microbubbles and

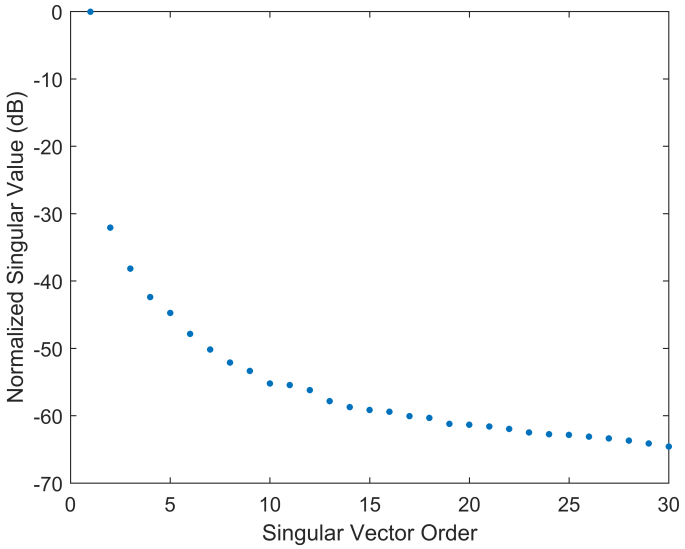

Figure 2.22: Singular value distribution of 30 plane-wave frames.

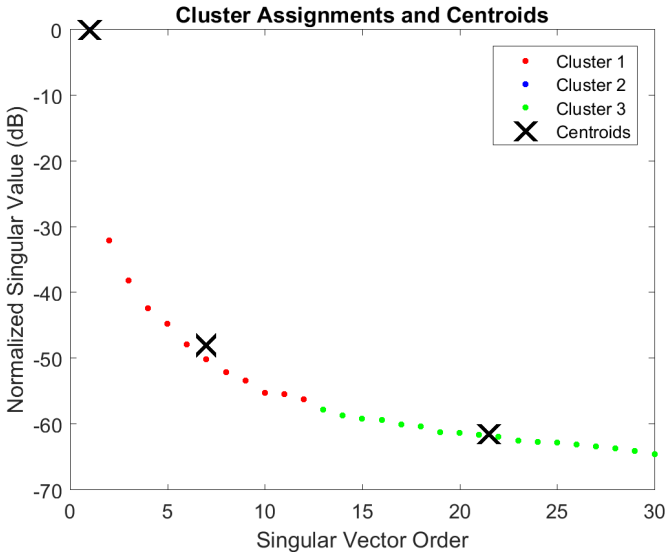

Figure 2.23: Clustering singular values for automatic spatiotemporal processing of HFR contrast-enhanced ultrasound images. The ensemble size was 30.

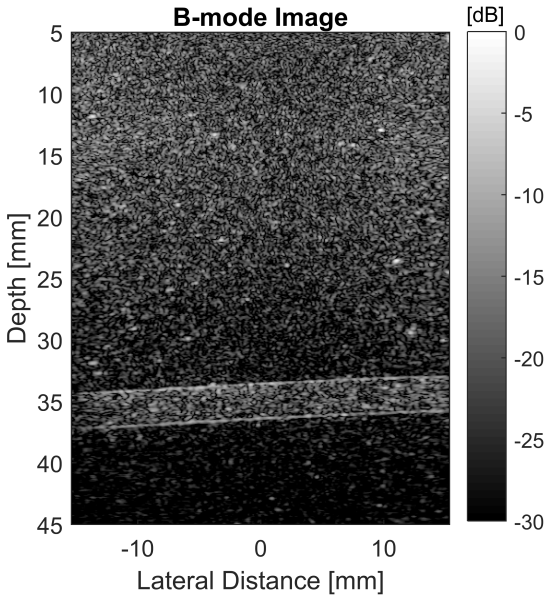

Figure 2.24: One typical B-mode image reconstructed from a single plane wave.

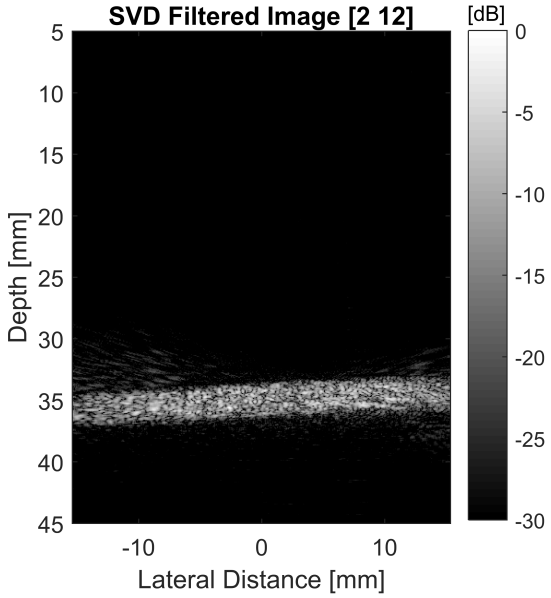

Figure 2.25: Corresponding B-mode image after SVD filtering. The orders of the used singular vectors are from 2 to 12 as shown in Fig. 2.23.

noise. The partitioned three clusters and their corresponding centroids are shown in Fig. 2.23. The second cluster with a middle level of coherence energy was then selected for reconstruction of microbubble signals.

The original B-mode image from a single plane wave is shown in Fig. 2.24 with its counterpart after SVD filtering shown in Fig. 2.25. The result shows that clustering singular values could provide a means to automate spatiotemporal processing of HFR contrast-enhanced ultrasound images. The immense potential of fully automatic SVD filtering techniques has not been unlocked yet, especially for large and dynamic organs such as the heart. The corresponding dataset may consist of spatiotemporally varied coherence over the cardiac cycle, where a block-wise SVD scheme might be of interest (Song *et al.*, 2017). The unwavering prevalence of conventional high pass filtering techniques in ultrasound Doppler imaging can be attributed to their higher computation efficiency compared to that using SVD. The development of accelerated SVD algorithms (Song *et al.*, 2017) is thus timely and desired for myriad applications, including functional brain imaging and super-resolution imaging, when using HFR contrast-enhanced ultrasound.

In conclusion, not only do these HFR contrast-enhanced ultrasound imaging techniques inspire the revisiting of fundamental applications such as Doppler and flow imaging, but also they promise a bright future for useful imaging methods with ultrahigh spatial or temporal resolution by processing the large amount of data.

Chapter 3

Combining Acoustic Trapping with Plane Wave Imaging for Localised Microbubble Accumulation in Large Vessels

The capability of accumulating microbubbles using ultrasound could be beneficial for enhancing targeted drug delivery. When microbubbles are used to deliver a therapeutic payload, there is a need to track them, for a localised release of the payload. In this chapter, a method for localising microbubble accumulation with fast image guidance is presented. A linear array transducer performed trapping of microbubble populations interleaved with plane wave imaging, through the use of a composite pulse sequence. The acoustic trap in the pressure field was created parallel with the direction of flow in a model of a vessel section. The acoustic trapping force resultant from the large gradients in the acoustic field was engendered to directly oppose the flowing microbubbles. This was demonstrated numerically with field simulations, and experimentally using the UARP II. SonoVue microbubbles at clinically relevant concentrations were pumped through a tissue-mimicking flow phantom and exposed to either the acoustic trap or a control ultrasonic field composed of a single-peak acoustic radiation force beam. Under the flow condition at a shear rate of 433 s^{-1}, the use of the acoustic trap led to lower speed estimations ($p < 0.05$) in the centre of the acoustic field, and an enhancement of 71% $\pm$ 28% ($p < 0.05$) in microbubble image brightness.

3.1 Introduction

The widespread employment of microbubbles as ultrasound contrast agents is attributed to their strong scattering capabilities and relative safety. The clinical use of microbubbles is to enhance the contrast in echocardiography (Senior *et al.*, 2009) and improve the visualization of liver perfusion (Battaglia & Cervelli, 2017), and so on. It is suggested that asymmetric microbubble oscillations across ultrasonic compression and rarefaction phases are responsible for the generation of harmonics (Faez *et al.*, 2013), in addition to scattering of higher harmonics due to nonlinear propagation (Leighton, 2007). Contrast imaging modalities which investigate microbubble nonlinear fundamental and second harmonic oscillations have been implemented in commercial systems (Phillips & Gardner, 2004). Myriad techniques which use microbubble subharmonic (Forsberg *et al.*, 2000) and superharmonic (Bouakaz *et al.*, 2003) frequencies are being explored to further improve the image quality. In recent years, HFR ultrasound, which typically uses unfocused plane/diverging wave transmissions (Montaldo *et al.*, 2009; Papadacci *et al.*, 2014), has been combined with microbubbles (Couture *et al.*, 2012; Toulemonde *et al.*, 2017c; Viti *et al.*, 2016). This has led to non-destructive microbubble detection at frame rates two orders of magnitude higher than the established line-by-line imaging mode. The large amount of data in HFR contrast-enhanced ultrasound has created a renewed interest in simultaneous Doppler and perfusion imaging (Tremblay-Darveau *et al.*, 2014) and provided opportunities for super-resolution imaging (Errico *et al.*, 2015).

The therapeutic use of microbubbles is currently an area of great interest. Microbubble volumetric vibrations can be actively driven by the use of ultrasound (de Saint Victor *et al.*, 2014), and the associated bio-mechanical effects have been used as a mechanism to break up blood clots since the 1990s (Tachibana & Tachibana, 1995). For sonoporation, the enhanced cell membrane permeability caused by localised microbubble oscillations (Kooiman *et al.*, 2014), has been shown to improve uptake of co-administered therapeutics (Mclaughlan *et al.*, 2013; Van Wamel *et al.*, 2006). Microbubbles can also be engineered as drug vehicles and payload release can be activated through the external acoustic fields at specific locations (Escoffre *et al.*, 2013; Lentacker *et al.*, 2009). Following intravenous injections, a low microbubble concentration in the ROI can hamper their therapeutic potential for sonothrombolysis (Petit *et al.*, 2015) or trans-membrane

drug delivery (Ward *et al.*, 2000). Conjugating microbubbles with antibodies can target them to vascular receptors with high specificity (Liu *et al.*, 2006), but some approaches can elicit an immune system response (Ferrara *et al.*, 2007). Furthermore, the targeting efficiency is reduced in the presence of high flow rates (Takalkar *et al.*, 2004). Microbubbles preferentially travel along the centreline of a vessel where the flow is fastest, which reduces binding further in large vessels, as microbubbles are not in the proximity of the diseased blood vessel endothelium. To address these limitations, ARF has been used to manipulate the position of microbubbles to the distal vascular wall in order to facilitate the cellular binding (Dayton *et al.*, 1999; Gessner *et al.*, 2012; Patil *et al.*, 2011; Wang *et al.*, 2013) and locally increase the microbubble concentration.

An alternative approach to ARF is the use of magnetic nanoparticle-doped microbubbles that can be manipulated by an external magnetic field (Owen *et al.*, 2012). *In vitro* (Crake *et al.*, 2015) and *in vivo* (Crake *et al.*, 2016) studies demonstrated that magnetic targeting of microbubbles can be achieved with a constrained depth of 20 mm. The use of optimised magnetic arrays could achieve improved targeting performance in terms of depth and accuracy (Barnsley *et al.*, 2016). These optimised arrays are comprised of multi-layer permanent magnet elements, generating the maximum field strength at a position of interest. Unfortunately, implementing this technique is difficult, since optimisations are valid only for specific depths.

Locally accumulating microbubbles over time would promote interactions with the diseased tissue in space, and permit enhanced mechanical bioeffects with the given microbubble dose upon therapeutic excitations. There is also a strong benefit of image monitoring which in turn guides localised microbubble accumulation and release of the payload. In large blood vessels, potentially all of these will contribute to therapeutic regimes involving acoustic cavitation, such as sonothrombolysis and trans-membrane drug delivery for atherosclerosis (Shamout *et al.*, 2015). In this chapter, a method for controlled microbubble accumulation through combining acoustic trapping with plane wave imaging is presented. The use of custom ultrasonic beams to image, translate, and retain microbubbles against physiologically relevant flow rates was investigated with a linear array transducer.

Table 3.1: L11-4v Transducer and Field-II Simulation Properties

Parameter	Value
Number of elements	128
Pitch size	0.30 mm
Element height	6 mm
Elevation focus	20 mm
Centre frequency	7.55 MHz
Bandwidth (−6 dB)	0.90 (fractional)
Sampling frequency	160 MHz
Excitation signal	3-cycle sinusoid (7 MHz)
Speed of sound	1547 m/s (Section 3.4.1)
Acoustic attenuation	0.42 dB/MHz/cm (Section 3.4.1)

3.2 Acoustic Microbubble Trapping and Imaging

This section details the implementation of a composite ultrasound sequence that combines both trapping and plane wave imaging modalities. An acoustic trap field comprised of phase and amplitude modulated beams affects microbubble flow behaviour to achieve localised accumulation and the instantaneous switch to imaging beams is expected to track microbubbles.

By considering a linear array transducer with N_e active elements that is split into two equal apertures, two equivalent but π phase shifted plane waves were emitted simultaneously from these subapertures ($N_e/2$ elements) and destructively interfered at the centre of the field. Fig. 3.1(a) shows a normalized 3-D PNP field (an animation can be found in Supplementary Video S1, https://ieeexplore.ieee.org/document/8361061) using the Field II package (Jensen & Svendsen, 1992) with parameters given in Table 3.1. To ensure clarity of the figure values below a threshold of −25 dB were removed. The arrow in Fig. 3.1(a) shows the flow direction of microbubbles. An acoustic null at the centre of the acoustic field produces the pressure gradients required for the trapping effect to arrest microbubbles in flow. To visualize the null zone in the elevation

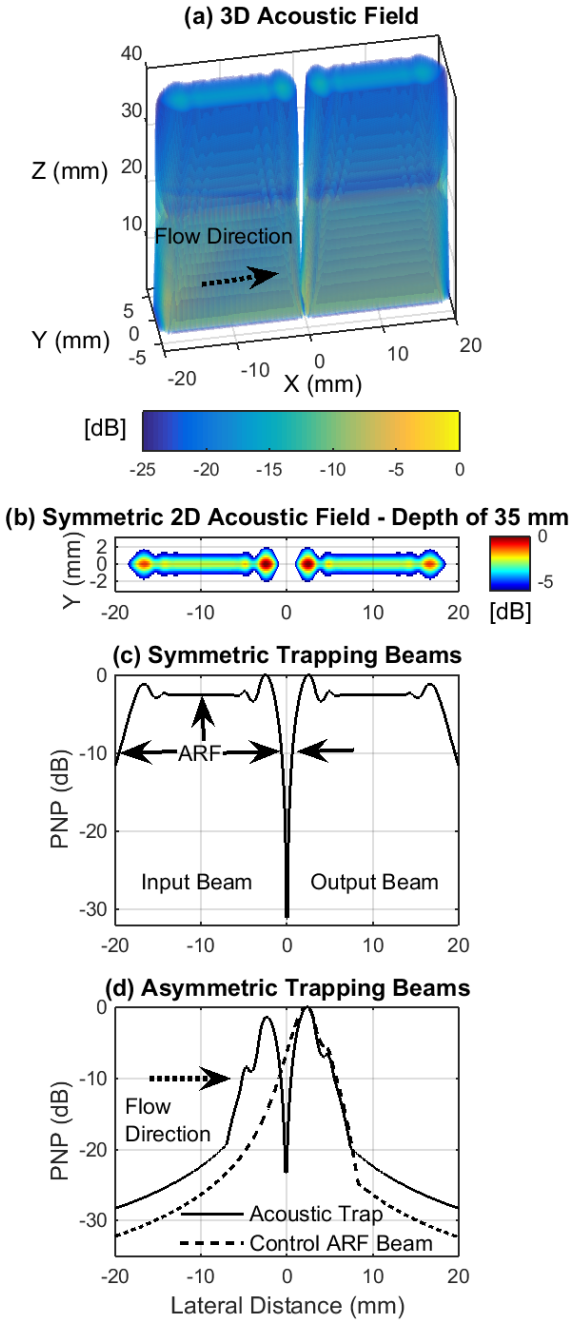

Figure 3.1: PNP simulations by Field II. (a) Symmetric 3-D acoustic trap field. At the depth of 35 mm: (b) −6 dB 2-D acoustic field; PNP profiles by emitting π phase shifted (c) symmetric and (d) asymmetric plane wave beams. The number of active elements (N_e) that were excited for the acoustic trap was 128 for (a)-(c) and 64 for (d). The control ARF beam in (d) was emitted by the 32-element output aperture. For the acoustic trap and control ARF beam in Fig. 3.1(d), an asymmetric Hann apodization window was applied to the central 64 elements.

direction, the −6 dB acoustic field at the depth of 35 mm is shown in Fig. 3.1(b). This plot was normalized by its own maximum value and the 35 mm depth was chosen to match the experimental setup in Section 3.4.2. The input beam (Fig. 3.1c) reduces the microbubble velocity through a primary radiation force that opposes the direction of flow. A disadvantage of using all (128) elements is that the radial radiation force within the inlet region impedes microbubbles entering the trapping region (Fig. 3.1c). To address this, the pressure was lowered by asymmetrically apodizing the outer elements of the array. Parameters relating to this operation were set for the given flow condition and more information about the ultrasound parameters is given in Section 3.4.2. The resulting simulation of the acoustic trap is shown in Fig. 3.1(d). The asymmetric trapping beam generates a lower pressure at the inlet, compared with that at the outlet. A single-peak ARF push beam resolved by emitting tapered plane waves only from the output aperture is also included in Fig. 3.1(d) as the control ARF beam in this study.

To monitor microbubble trapping, pulses for plane wave imaging were interleaved with the trapping beams. Every full field-of-view 2-D image was acquired through a single plane-wave transmission. Plane wave imaging was adopted to preserve the trapping efficiency by minimising the time needed for imaging feedback (Couture *et al.*, 2012; Viti *et al.*, 2016).

3.3 Forces on Microbubbles in A Trapping Field

In this section, the formulation of forces on a microbubble is undertaken followed by a simulation demonstrating the trapping effect on a single microbubble. The secondary radiation force that is produced by the microbubble re-scattered field is neglected in the present method.

3.3.1 Primary Radiation Force

The use of a linear array simplifies analysis within the 2-D imaging plane. In a trapping field, microbubbles will experience the axial radiation force, as shown in (Dayton *et al.*, 1997), and a trapping force through the generation of lateral pressure gradients (Harput *et al.*, 2016; Raiton *et al.*, 2012). Difficulties in characterizing the primary radiation

force on microbubble populations, can arise from different configurations of the ultrasonic system, the microbubble size distribution and concentration as highlighted in (Dayton *et al.*, 1997). But the force F_{b} on a single microbubble can be estimated by Eq. (3.1) (Dayton *et al.*, 1997; Leighton *et al.*, 1990):

$$F_{\mathrm{b}} = -\langle V(t)\nabla P\rangle\,, \tag{3.1}$$

where $\langle\ \rangle$ indicates a time average, $V(t)$ and ∇P are the microbubble volume and spatial pressure gradient, respectively.

At a specific depth of the trapping field, the axial radiation force F_{axial} on a microbubble can be formulated by Eq. (3.2) (Dayton *et al.*, 1997):

$$F_{\mathrm{axial}} = \frac{2\pi\,(P_{\mathrm{a}}W_x)^2\,D\,R_0}{\rho\,c\,\omega\,T}\,\frac{2\beta_{\mathrm{tot}}/\omega}{[(\omega_0/\omega)^2-1)]^2+(2\beta_{\mathrm{tot}}/\omega)^2}, \tag{3.2}$$

where P_{a} and W_x mean the peak acoustic pressure amplitude and the pressure amplitude modulation function in the direction (x) orthogonal to the incident field, respectively. D/T indicates the pulse duty cycle. ω and ω_0 denote the driving frequency and resonant frequency of the microbubble, respectively. R_0 is the equilibrium microbubble radius, ρ is the medium density, c is the speed of sound in the medium, and β_{tot} is the dimensionless damping coefficient.

In the direction perpendicular to the axial ultrasonic beam and at a specific depth, the amplitude modulated trapping field is modelled with a sinusoidal pattern (Yamakoshi & Noguchi, 1998). The acoustic amplitude P_{lateral} along this direction which is defined by the axis x is thus written as follows:

$$P_{\mathrm{lateral}} = P_0 + P_{\mathrm{a}}B(x)\sin(kx)\cos(\omega t), \tag{3.3}$$

where P_0 is the constant hydrostatic pressure and t is time. $k = 2\pi/\lambda_{\mathrm{lateral}}$, and $\lambda_{\mathrm{lateral}} = 10.8$ mm is the wavelength of the modelled sinusoidal pattern which is given by Fig. 3.2(a). For simplicity, the symmetric trapping setup with 64 active elements transmitting 7 MHz travelling waves was configured for Fig. 3.2(a) and a Hann window was applied to the active aperture to modulate the pressure amplitude. The constant hydrostatic pressure is not shown in Fig. 3.2(a) and the simulated pressure profile was normalized by P_{a} as given in Eq. (3.2) and Eq. (3.3). $B(x)$ is a rectangular window function which is defined by

$$B(x) = \begin{cases} 1, & -\frac{\lambda_{\text{lateral}}}{2} < x < \frac{\lambda_{\text{lateral}}}{2}, \\ 0, & \text{otherwise.} \end{cases} \tag{3.4}$$

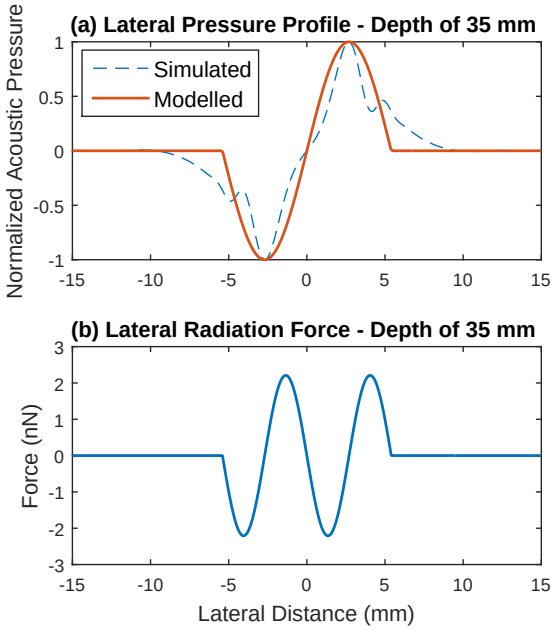

Figure 3.2: At the depth of 35 mm, (a) simulated and modelled lateral pressure patterns at the moment $t = 0$ in Eq. (3.3), and (b) the lateral radiation force on a 2.2-μm microbubble based on parameters given in Table 3.2.

The lateral pressure gradient $\nabla P_{\text{lateral}}$ is thus given by Eq. (3.5):

$$\nabla P_{\text{lateral}} = kP_{\text{a}}B(x)\cos(kx)\cos(\omega t). \tag{3.5}$$

Assuming linear amplitude oscillations, the microbubble volume can be modelled as Eq. (3.6) (Leighton *et al.*, 1990) for microbubbles with a resonant frequency below the ultrasound drive frequency.

$$V(t) = V_0[1 - (3R_{\text{e0}}/R_0)\sin(kx)\cos(\omega t + \pi)], \tag{3.6}$$

where V_0 is the equilibrium microbubble volume and R_{e0} is the instantaneous variation of the microbubble radius which is given by Eq. (3.7) (Dayton *et al.*, 1997):

$$R_{\text{e0}} = \frac{P_{\text{a}}}{R_0\rho\omega^2\sqrt{[(\omega_0/\omega)^2 - 1)]^2 + (2\beta_{\text{tot}}/\omega)^2}}. \tag{3.7}$$

Thus, the lateral radiation force F_{lateral} on a microbubble in a pulsed trapping field is deduced to be Eq. (3.8):

$$\begin{aligned} F_{\text{lateral}} &= -\left\langle V(t)\nabla P_{\text{lateral}}\frac{D}{T}\right\rangle \\ &= -\frac{3R_{\text{e0}}V_0\sin(2kx)kP_{\text{a}}B(x)}{4R_0}\frac{D}{T}. \end{aligned} \tag{3.8}$$

3.3.2 Stokes Drag Force and Microbubble Trapping

With the assumption that the microbubble radius does not change (Dayton *et al.*, 1997; Tortoli *et al.*, 2000), the Stokes drag force F_{drag} acting on one microbubble in fluid is given by Eq. (3.9) (Dayton *et al.*, 1997):

$$F_{\text{drag}} = 6\pi\eta R_0(v_{\text{f}} - v_{\text{b}}), \tag{3.9}$$

where η is the dynamic viscosity of the liquid, v_{b} and v_{f} are the microbubble and liquid velocity, respectively.

Considering a flow direction perpendicular to the axial ultrasonic beam, the lateral microbubble motion in a trapping field is described by Eq. (3.10), while neglecting the effect of gravity and buoyancy (Tortoli *et al.*, 2000; Yamakoshi & Noguchi, 1998)

$$m_{\text{b}}\frac{\mathrm{d}v_{\text{b}}}{\mathrm{d}t} + F_{\text{drag}} + F_{\text{lateral}} = 0, \tag{3.10}$$

where m_{b} is the microbubble mass.

A microbubble is trapped by the lateral radiation force when $v_{\text{b}} = 0$ and $\mathrm{d}v_{\text{b}}/\mathrm{d}t = 0$ are satisfied in Eq. (3.9) and Eq. (3.10). In this case, the maximum speed $\|v_{\max}\|$ of the microbubble which can be trapped is given by Eq. (3.11) through combining Eq. (3.8)-(3.10)

$$\|v_{\max}\| = \left\| \frac{R_{\text{e0}}V_0\sin(2kx)kP_{\text{a}}B(x)}{8{R_0}^2\pi\eta}\frac{D}{T}\right\|. \tag{3.11}$$

A simulation was performed by assuming the presence of a 2.2-μm SonoVue microbubble in purified water, with the microbubble positioned at a depth of 35 mm relative to the transducer surface. The lateral radiation force on the microbubble is shown in Fig. 3.2(b) with parameters reported in Table 3.2. Based on Eq. (3.11), the

microbubble with a velocity up to 5.3 cm/s can be halted at the 1.4 mm position where the trapping force reaches its maximum assuming that the flow is entering from the left side.

The presence of the input beam would displace microbubbles to the side of a vessel as a result of the axial radiation force. The displacement could decrease the velocity of the microbubbles (Dayton *et al.*, 1999) before they enter the trap region, allowing a larger fraction of microbubbles arrested by the trapping force.

Table 3.2: Parameters Used for Fig. 3.2(b)

Parameter	Value
Trapping setup	Symmetric (see Fig. 3.2a)
P_{a}	500 kPa
R_0	2.2 μm
ρ	998 kg/m^3
f	7 MHz
f_b	6.8 MHz (Gorce *et al.*, 2000)
$2\beta_{\mathrm{tot}}/\omega$	$0.15\frac{f_b}{f}$ (Dayton *et al.*, 1997)
η	1 mPa.s
λ	10.8 mm (see Fig. 3.2a)
$\frac{D}{T}$	50%

3.4 Experimental Tests

A tissue mimicking material (TMM) ultrasound flow phantom (Harput *et al.*, 2013) was manufactured for the experimental component of this study. For all experimental conditions, both the trapping field and control ARF beam as described in Section 3.2 were used.

3.4.1 Ultrasound TMM Phantom Manufacture

A wall-less agar-based TMM flow phantom was made by mixing 36 g (3% by mass) agar power (Acros Organics, Geel, Belgium) and 25 g glass microspheres (P2011SL-2.5, Cospheric, Santa Barbara, USA) with filtered and degassed water. The mixture was then heated on a hot plate (Corning, Inc., Mexico) until the temperature reached 96 °C for 30 minutes. Glycerine (Value Health, Nottingham, UK) of 8% by mass and 10 g Germall plus (Gracefruit, Stirlingshire, UK) were added when the temperature was below 70 °C. The continuous stirring throughout the whole process permitted a uniform distribution of ultrasound scatters. Once mixed, the solution was poured into a container incorporated with a 2.8-mm plastic tube. The tube was removed after the phantom set to create a wall-less flow phantom. The average speed of sound and attenuation through this TMM was measured to be 1547 m/s and 0.42 dB/MHz/cm, respectively (Browne *et al.*, 2003).

3.4.2 Flow Model and Experimental Parameters

The inlet of the 2.8-mm vessel at a depth of 35 mm (Fig. 3.3) was connected to a syringe, which was driven by a pump (Aladdin AL-1000, World Precision Instruments). The outlet was collected in a beaker and disposed of. At the ambient temperature 20 ± 1°C, SonoVue (Bracco S.p.A, Milan, Italy) solutions (diluted by 1:3000) were passed through the vessel with a constant flow rate of 56 mL/min (V_{mean} = 152 mm/s). Considering a Newtonian fluid, this flow corresponds to a shear rate of 433 s^{-1}, which is within the range of human arterial flow (Jeong & Rosenson, 2013). Inlet tubing of 50 cm ensured a constant parabolic flow profile within the imaging field as formulated by $L = 0.04 d_v Re$, where L is the entrance length for steady laminar flow, d_v is the diameter of the vessel, and Re is the Reynold's number (Leow *et al.*, 2015). The flow parameters are given in Table 3.3.

The UARP II was programmed to generate the trapping and plane wave imaging modalities, in conjunction with a Verasonics L11-4v transducer (Verasonics, Inc., WA, USA). Each sequence consisted of dual excitations, the first being a long-duration 7 MHz trapping waveform as shown in Fig. 3.4, followed by a two-cycle 7.55 MHz pulse for plane wave imaging. The transducer had a centre frequency of 7.55 MHz with a −6 dB bandwidth of 90%.

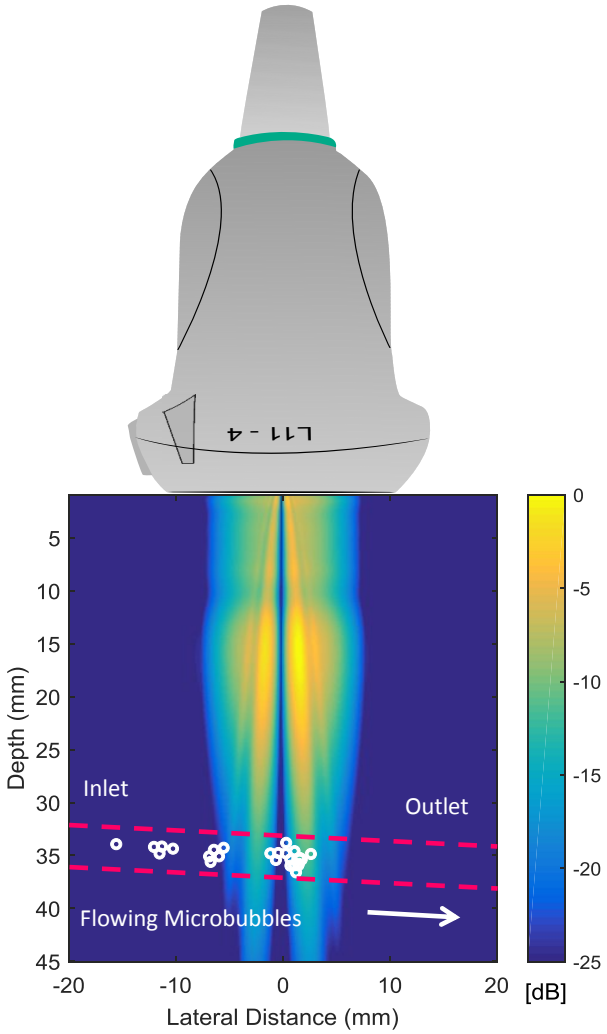

Figure 3.3: Schematic of the experimental setup with the simulated acoustic trap field (normalized PNP) superimposed onto the diagrammatic ultrasound flow phantom.

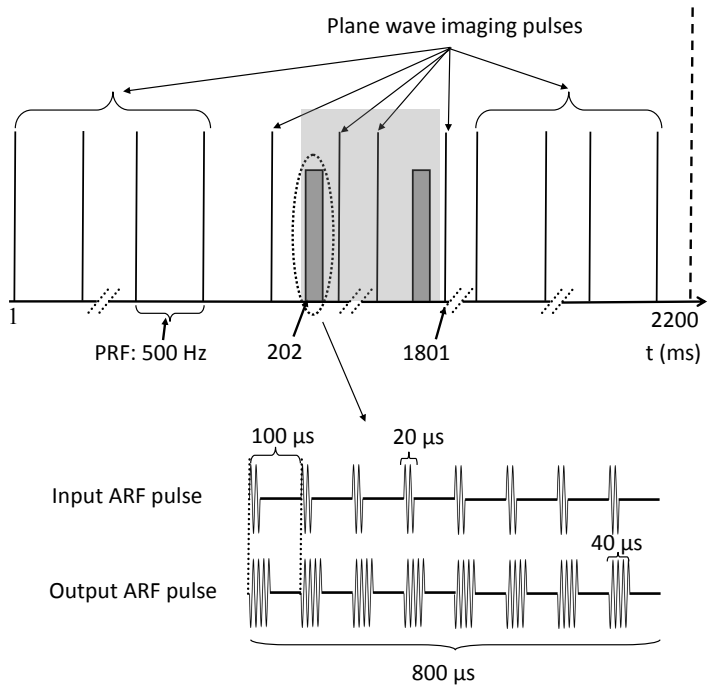

Figure 3.4: The timing of emission sequences in experiments. ARF beams were interleaved with the imaging mode from 202 to 1801 ms and the shading shows one period. For clarity, ARF pulses emitted from two subapertures are diagrammed.

Table 3.3: Flow Parameters

Parameter	Value
Flow model	2.8-mm vessel
Flow rate (mL/min)	56
Re	423
$V_{\max}$ (mm/s)	303
V_{mean} (mm/s)	152
Wall shear rate (s^{-1})	433
Flow condition	Laminar

A switching frequency of 1 kHz was chosen between these two schemes, which resulted in a 500-Hz frame rate for imaging. The schematic illustration of the sequence timing used in this study is shown in Fig. 3.4. The acoustic trap or control ARF beam was emitted in an intermittent way to protect the transducer (Fig. 3.4). ARF beams were activated between 202 and 1801 ms throughout the 2.2-s acquisition. For trapping microbubbles, the duty cycle ratio between the input and output apertures was empirically set to be 0.5 (Harput *et al.*, 2016). Only the output aperture was activated to emit the control ARF beam.

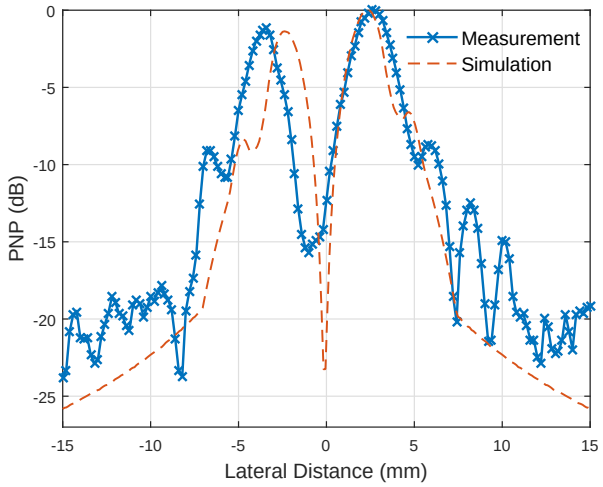

Figure 3.5: Estimated and measured PNP profiles of the acoustic trap (centre frequency: 7MHz) at the depth of 35 mm. The maximum derated PNP = 320 kPa in the measurement.

Pressures were measured by using a 200-μm calibrated needle hydrophone (Precision Acoustics, Dorchester, UK) in water at the depth of 35 mm. The maximum PNP for ARF beams was estimated to be 320 kPa (MI: 0.13 (Apfel & Holland, 1991; Church, 2005)) after correcting for the attenuation of the phantom, and the MI was tuned to 0.15 for imaging. For the given arterial flow condition, an aperture of 64 active elements was empirically set for the acoustic trap, and two 32-element subapertures were programmed to emit plane waves with the opposite phase polarity. The amplitude modulation of the beam as described in Section 3.2 was achieved through a pulse width modulation scheme (Cowell & Freear, 2008; Smith *et al.*, 2013). At the depth of 35 mm, the measured PNP profile of the designed acoustic trap is given in Fig. 3.5 and compared

with its simulated counterpart. Meanwhile, the improvement of lateral resolution in plane wave imaging is expected due to a larger aperture when all 128 elements are used to create each line of the image. Thus, all 128 elements were active for plane wave imaging.

All the raw data was subsequently transferred and saved to a local drive for offline post processing with Matlab (The MathWorks, Natick, MA, USA).

3.4.3 Analysis of Trapping Effects

The trapping force on the microbubble populations was used to affect their flow behaviour and retard them. Vector flow mapping through a custom speckle tracking algorithm (Nie *et al.*, 2016) was then used to provide a vector flow overlay to track microbubble trajectories, before, during, and after trapping. Briefly, RF frames were formed by using the delay and sum beamforming method (Montaldo *et al.*, 2009) with fixed axial and lateral sampling grids, followed by interframe displacement estimations. Displacements were first determined by using a correlation-based pattern matching method in integer pixels. Accompanied by median filtering and subpixel Gaussian interpolation (Niu *et al.*, 2010), the estimated displacements in conjunction with the known frame rate were used to render flow vectors within a ROI. Parameters in this processing are given in Table 3.4.

Table 3.4: Parameters in Beamforming and The Speckle Tracking Algorithm

Parameter	Value
Axial beamforming step	9.7 μm
Lateral beamforming step	75.0 μm
Axial kernel size	0.621 mm
Lateral kernel size	1.800 mm
Lateral kernel overlapping	50%
Axial kernel overlapping	50% or 66%

The influence, if any, of the vector density on the analysis of vector flow mapping was established by changing the size of the overlapped regions between blocks for equivalent

measurements. The axial and lateral kernel sizes are listed in Table 3.4 (Lenge *et al.*, 2014). This shows they were estimated with the ability to track the maximum velocity of 303 mm/s in this study (see Table 3.3). In each test, the interrogation window size and the lateral kernel overlapping size were kept unchanged, while the percentage of the axial window overlapping was varied between 50% and 66%.

A consequence of speed deceleration, caused by the trapping field, was that a greater quantity of microbubbles were deposited within the trap. The cumulative brightness (enveloped data) of microbubbles within ROIs was used to proportionally correlate microbubble quantities over time. The intensity baseline of this approach, was determined by replacing microbubble solutions with purified water.

For statistical analysis, a one-way ANOVA was used to demonstrate the statistical significance with a p value smaller than 0.05.

3.5 Experimental Results

3.5.1 Effects of a Trapping Field on Microbubble Flow Dynamics

Fig. 3.6 shows representative images acquired for, from top to bottom, water only, free-flowing microbubbles, microbubbles with the trapping field and microbubbles in combination with the control ARF beam. Schematic diagrams of PNP profiles across the vessel axis are added to Fig. 3.6(c) and (d).

In the presence of microbubbles, colour coded vector maps were superimposed onto their corresponding grey scale images reconstructed from single plane-wave pulses. These grey scale images are shown with a dynamic range of 40 dB in Fig. 3.6. The orientation of each arrow indicates the averaged interframe microbubble trace within that kernel, whilst the arrow length correlates the speed. In velocity estimations, the interrogation window occupied a depth span of 0.621 mm and a lateral width of 1.800 mm (see Table 3.4). The axial kernel overlapping of 50% was used for still vector flow frames in Fig. 3.6. Two adjacent plane-wave RF frames were needed to resolve a single vector flow frame, and no multi-frame averaging was applied to smooth the velocity profile.

Fig. 3.6(a) is a reference frame without microbubbles. The ROI within the flow channel showing microbubble trajectories was defined with dotted lines and utilised with all the data. The flow condition in this study was estimated to be steady (see

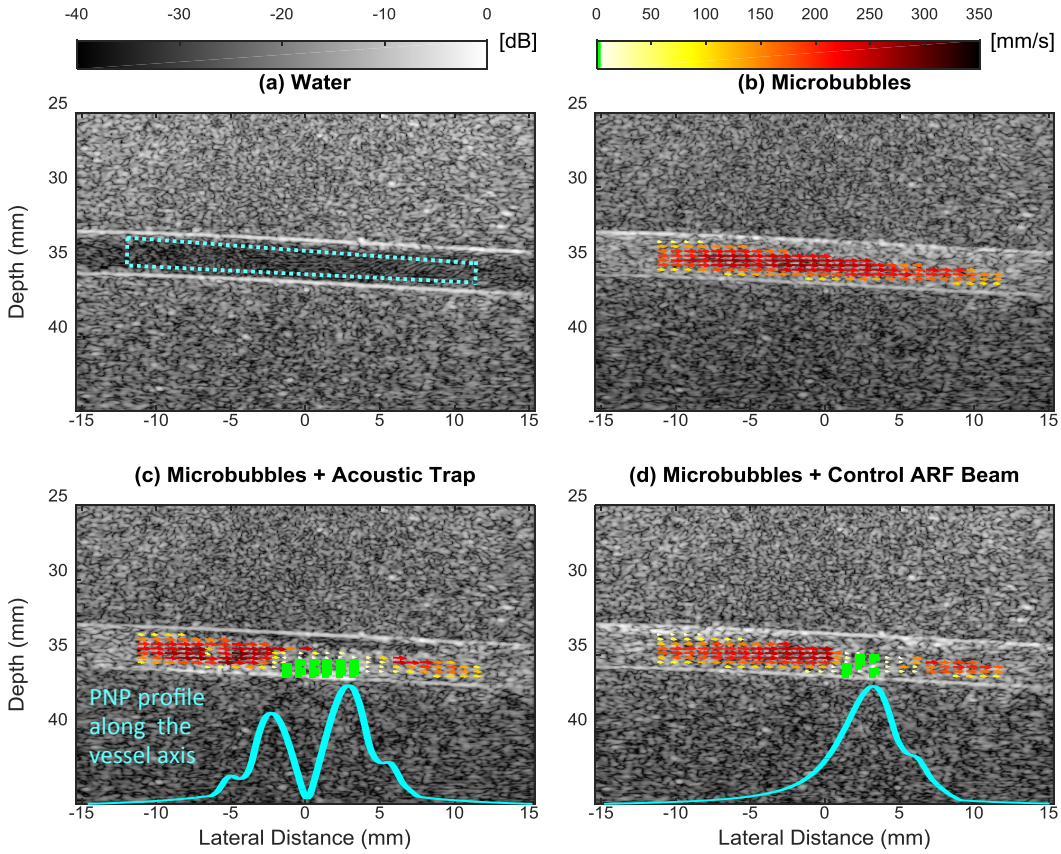

Figure 3.6: Examples of captured frames for (a) water, (b) freely flowing microbubbles, (c) microbubbles with the acoustic trap, and (d) microbubbles with the control ARF beam. In the presence of microbubbles, composite images are shown with the vector flow overlay. Flow vectors with a velocity slower than 5 mm/s are highlighted with green dots.

Table 3.3) and the resulting laminar flow would follow a parabolic pattern, with zero speed at the wall. With identical parameter sets used for Fig. 3.6(b)−(d), the noise floor of vector flow mapping was determined by processing one reference dataset with purified water pumped through the channel at a rate of 56 mL/min (see Section 3.4.3). Consequently, 1100 plane-wave RF frames (or 1099 vector flow maps) were used and the noise floor was found to be 1.2 ± 0.6 mm/s (mean value ± 3 standard deviations). To improve clarity, a threshold of 5 mm/s which is above the noise floor was used for labelling flow vector estimations as green dots, indicative of the occurrence of trapped microbubbles. Other values above the noise floor for velocity estimations could be used and the threshold of 5 mm/s was heuristically adopted for reporting. No flow direction information was available at these locations. The ROI was chosen to exclude flow vectors on the wall.

Supplementary Video S2 shows one example of the temporal evolution of microbubble flow patterns with acoustic trapping (https://ieeexplore.ieee.org/document/8361061). To reject noise mainly residing in the deep location, the SVD filter (Demené *et al.*, 2015) was introduced when producing the video. Interleaving the acoustic trapping beam with plane wave imaging pulses resulted in non-uniform microbubble flow speeds in the inlet, trap, and outlet regions (Fig. 3.6). When the eigen-based SVD filter was first applied to the global plane-wave data, the complex spatially-varying microbubble speed affected the consequential microbubble speckle pattern and complicated the velocity estimation. The block-wise SVD filtering has been suggested (Song *et al.*, 2017) to tackle spatially-varying characteristics but with heavy computational burdens. To simplify the processing in this study, the beamformed plane-wave RF frames were divided into the contrast region and the tissue background, and only the tissue background was spatio-temporally processed to remove noise. Noise is supposed to be described by high-order singular vectors which have smaller singular values (Demené *et al.*, 2015). The SVD filter order was chosen to be 10 from which the singular value curve starts to flatten (Song *et al.*, 2017) as shown in Fig. 3.7. Flow dynamics were tracked with the method detailed above. For Supplementary Video S2 (https://ieeexplore.ieee.org/document/8361061), the axial kernel overlapping of 50% was employed in velocity estimations and the video was played back at 25 fps.

To show the effect of the acoustic trap and control ARF beam on the flow profile, first a control experiment without any ARF beams was performed to calculate

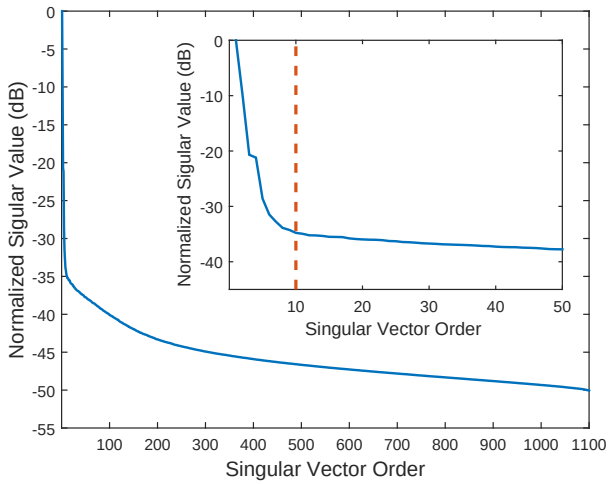

Figure 3.7: The singular value distribution for the data used in Supplementary Video S2. Inset: expanded view of the singular value distribution with a separation line showing the cutoff order of 10.

the baseline (Fig. 3.6b). Before the activation of ARF beams at $t = 202$ ms, there are no visible green dots representing trapped microbubbles. Fig. 3.6(c) shows a single snapshot of microbubble flow dynamics when the acoustic trap is active. Although the microbubble flow changes with time (see Supplementary Video S2, https://ieeexplore.ieee.org/document/8361061), the speed of microbubbles reduces significantly within the trapping region, with green dots showing trapped microbubbles. When compared with results by using the control ARF beam in Fig. 3.6(d), the acoustic trap in Fig. 3.6(c) enables more microbubble accumulation also in the lumen. Once acoustic trapping beams ceased at $t = 1801$ ms, the microbubble trajectories follow a laminar flow pattern similar to Fig. 3.6(b), as shown in Supplementary Video S2 (https://ieeexplore.ieee.org/document/8361061).

The two axial overlapping sizes in Table 3.4 were used to manipulate the density of flow vectors within the unaltered ROI. In each trial, the number of green labels was counted with the vector flow frame 101 to 900, considering the period (from 202 to 1801 ms) with the application of ARF beams. The normalized values are portrayed spreading the lateral axis as shown in Fig. 3.8. With the identical setup in velocity mapping, in comparison to experiments with the control ARF beam, where the drag force overcomes the counterflow radiation force, the acoustic trap shows the enhanced

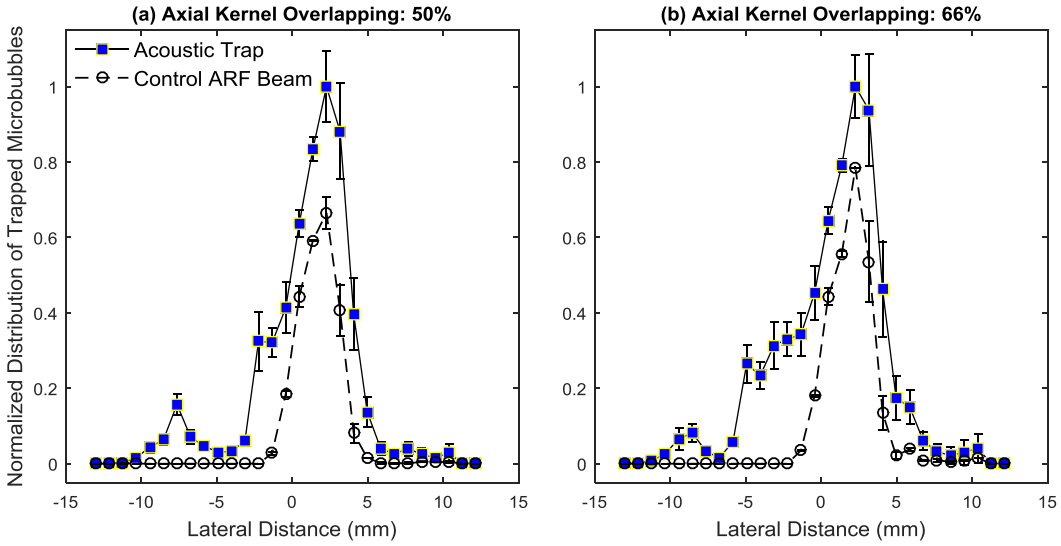

Figure 3.8: Normalized distributions of trapped microbubbles along the lateral axis are shown by summing green dots from vector flow maps. The mean value and standard deviation are given based on three repeated trials.

capability of microbubble accumulation ($p < 0.05$) for both conditions in Fig. 3.8.

3.5.2 Effects of a Trapping Field on Microbubble Signal Amplitude Curves

Three ROIs were defined and allocated at the inlet, the designed trapping region and the outlet as shown in Fig. 3.9(a). The signal magnitude curves are presented as a function of time over three repeated trials in Fig. 3.9(b)−(d).

During the first 202 ms duration without the use of ARF, no significant magnitude differences were observed (Fig. 3.9c and d). In the following 1.6-s period with the application of the acoustic trap, signal amplitudes from all three ROIs showed increases until approaching a steady state. Whereas in control experiments, the similar increasing trend of intensities occurred only in the trap and outlet ROIs. During the last 200 ms, specific to the trap ROI, an instantaneous signal increase was perceptibly observable after the cessation of ARF (Fig. 3.9c and d). However, much higher amplitudes were obtained with the acoustic trap. A secondary radiation force that was generated from microbubble re-scattered fields, can be attractive or repulsive determined by the relationship of microbubble vibration phases. In response to ARF beams, the

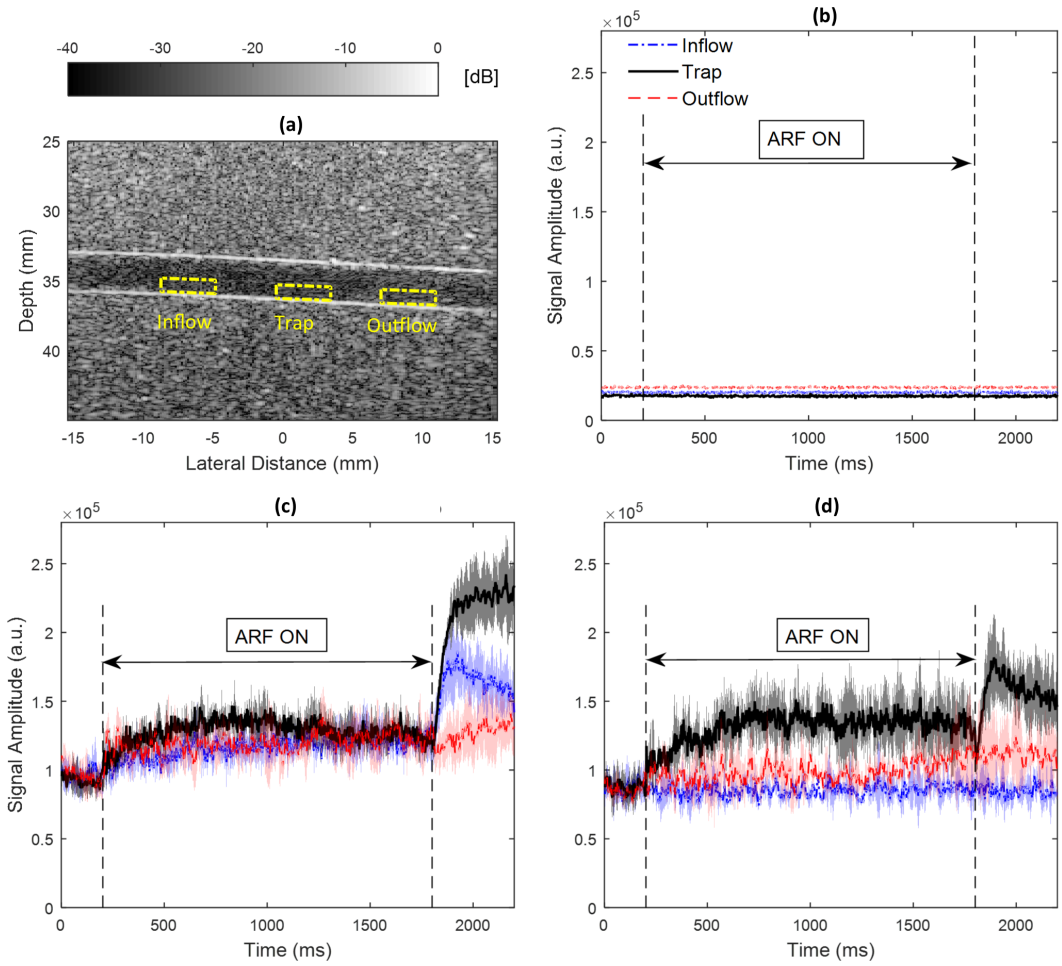

Figure 3.9: Average intensity curves in (a) ROIs are displayed as a function of time, for (b) water, (c) microbubbles + the acoustic trap, and (d) microbubbles + the control ARF beam. Results are shown with the mean and standard deviation from three trials.

secondary radiation force was present as aggregating microbubbles during sonication. The dispersion of microbubble clusters after ceasing ARF has been demonstrated to be responsible for the transient amplitude enhancement (Wang *et al.*, 2013, 2015). Thus, the prediction of microbubble quantities through image intensities would only be reliable after deactivating ARF beams. Consequently, within the trap ROI from 1900 to 2200 ms, the acoustic trap led to an average amplitude improvement of 71% ± 28% ($n = 3$, $p < 0.05$) over the control, indicating more efficient microbubble localisation.

3.6 Discussion

With a linear array transducer, this study demonstrated the use of acoustic trapping and plane wave imaging to facilitate localised microbubble accumulation. The proposed scheme was illustrated by simulating and measuring the beam pattern and further verified with a wall-less flow phantom. Greater microbubble accumulation was achieved within a ROI in a controlled way when the trapping field was activated. The interleaved plane wave imaging modality enabled the monitoring of this process. In the presence of additional therapeutic excitations, accumulated bare microbubbles using the proposed scheme are expected to enhance microbubble-cell interactions resultant from the increased microbubble concentration (Crake *et al.*, 2015). When microbubbles are functionalized or attached with a therapeutic payload such as a liposome (Peyman *et al.*, 2012), a localised payload release, and possibly control of the concentration of payload through varying the cluster size, could be achieved by using a single transducer performing microbubble trapping, imaging, and destruction.

Influenced by the ARF beams, the secondary radiation force from the microbubble re-scattered pressure field aggregates microbubbles. The microbubble cluster dynamics could be described with an identical model for a single microbubble through inputting the cluster radius to the system (Kooiman *et al.*, 2014). Consequently, clusters will resonate at a lower driving frequency. It is difficult to estimate the cluster radii *in vivo* making the resonant frequency unpredictable, which could affect imaging or payload release. When microbubbles are clustered it is hard to destroy them. However, after the trap is ceased they start to disperse. The instant increase of microbubble intensities in Fig. 3.9(c) and (d) is illustrated as a result of microbubble cluster dispersion (Wang *et al.*, 2013, 2015). Thus, it would be possible to destroy them and maximise the

release from a therapeutic microbubble by setting an appropriate time delay between the destruction pulse and trapping beam.

Quantifying trapped microbubbles with ultrasound imaging is challenging. The off-resonance driving, attenuation, and acoustic shadowing are responsible for the suppression of the intensity increase, irrelative with the real microbubble concentration. The size of clusters or the number of microbubbles cannot be estimated from the B-mode or contrast mode images when the trapping beam is active. In this study, the image brightness after deactivating ARF beams, as shown in in Fig. 3.9 (c) and (d) between 1900 and 2200 ms, was quantified and the acoustic trap showed an average gain of 71% $\pm$ 28% ($n = 3$, $p < 0.05$) relative to the control ARF beam.

The use of the 1-D linear array lacks the capability of beamforming along the elevation axis, which limits acoustic trapping as one in-plane method. Given the 3-D nature of vascular anatomy and blood flow, a 2-D array would be of immense importance which enables simultaneous microbubble trapping and imaging in a 3-D volume. With a fully addressed 2-D array, the high channel count would place a heavy burden on electronics. The optimised sparse array could be a good candidate, which maintains moderate acoustic field patterns but with much reduced active elements (Roux *et al.*, 2017). Although having a limitation in the elevation direction, the experimental comparison between the acoustic trap and a control ARF beam showed that the acoustic trap retained a larger microbubble population in the lumen area of a 2.8-mm vessel (Fig. 3.6c). This would be advantageous in cases where targets are not only located along the distal wall. Potentially, benefiting from the two-peak acoustic trap and the counterflow radiation force, microbubble localisation would be more resistant to the pulsatile nature of blood flow.

Narrower acoustic trapping regions can be achieved with higher driving frequencies resulting from shorter wavelengths. But the use of higher frequencies will be prone to higher attenuation. A centre frequency of 7 MHz was used for trapping in this study, but the easy control of electronics enables the flexible frequency modification for vessels at different depths.

Plane wave imaging should be operated in a real-time and continuous manner to assist motion detection, which is very important to keep the trap always in the targeted region. The use of a graphics processing unit (GPU)-based beamformer (Yiu

et al., 2011) may allow for the fast realization of plane wave imaging. To selectively image microbubbles, nonlinear imaging modalities such as subharmonic imaging (Harput *et al.*, 2013; McLaughlan *et al.*, 2017), PI, or AM (Eckersley *et al.*, 2005) can be further investigated.

There are multiple ways to manipulate the formation of the acoustic trap to accommodate different flow rates. For example, adjusting the driving voltage or dynamically apodizing the aperture of the transducer, could account for variable pressure slopes in the trap field, and thus simple ways to engender varying counterflow radiation forces. For the given flow condition in this study, empirically determined parameters were used for trapping microbubbles. More automated approaches to determine the required acoustical parameters should be further investigated. The fast realization of plane wave imaging could also make it possible to have the necessary feedback loop and guide the determination of required parameters.

The use of purified water as circulating fluid in a wall-less flow phantom is a simplified experimental demonstration of a complex *in vivo* application. The presence of other molecules within the blood stream, red blood cells for example, could interfere with microbubble trapping. The relative angle between the transducer and the vessel would affect the performance of the proposed method, which could be optimised through imaging prior to trapping. As the angle increases, so does the trapping efficiency. To make this scheme more widely adopted, a solution that could be employed is to tilt the transducer or electronically steer the beam, as is broadly used in ultrasonic colour Doppler imaging.

Acoustic trapping of microbubbles by using a linear array transducer was demonstrated with a tissue-mimicking flow phantom. In this section, intuitive observation of microbubble trapping under a microscope is presented. A 200-μm cellulose tube was positioned in water at the depth of 35 mm parallel to the transducer surface. The acoustic trapping beam had a centre frequency of 7 MHz and a output duty factor of 30% for a PRF of 1 kHz. The duty factor ratio between the input and output plane-wave beams was 0.5 and the MI of 0.12 was used. Other details of the acoustic trap can be found in Section 3.4.2. The flow rate of 5 mL/h was set to achieve a mean velocity of approximately 35 mm/s in the expanded cellulose tube when filled with water. Fig. 3.10 shows a series of micrographs acquired at different moments during the experiment where the incident acoustic beam is from the left side of the figure. Flowing

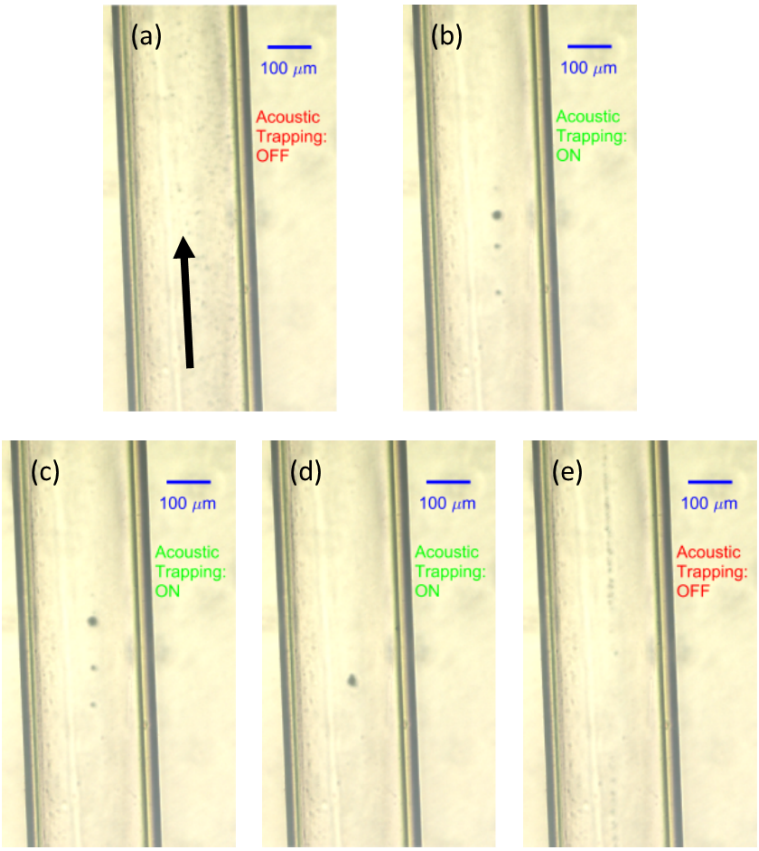

Figure 3.10: (a) Microbubbles in flow without acoustic trapping. The arrow shows the flow direction. (b) A cluster of trapped microbubbles. (c) The microbubble cluster started to shift away. (d) A new microbubble cluster replaced the previous one. (e) The microbubble cluster started to disappear after the end of ultrasound exposure.

microbubbles are barely visible without the application of the trapping beam as shown in Fig. 3.10(a). With the activation of the trapping beam, the microbubble cluster was trapped for a few seconds (Fig. 3.10 b). Once the trapping force was insufficient, the microbubble cluster started to shift away as shown in Fig. 3.10(c). A new microbubble cluster replaced the previous one (Fig. 3.10 d) and it was halted until the cease of ultrasound exposure (Fig. 3.10 e).

3.7 Conclusion

The capability of localised accumulation of microbubbles holds promise for the enhanced therapeutic use of microbubbles to treat vascular diseases. In this study, one scheme allowing for simultaneous microbubble trapping and imaging was proposed and demonstrated. After a period of 1.6 s with ARF beams interleaved, the acoustic trap outperformed the control, with slower microbubble speeds in the centre of the sound field ($p < 0.05$) and an enhancement of 71% $\pm$ 28% ($p < 0.05$) in image brightness. The easy control of electronics would enable this scheme applicable to a range of flow conditions, and with attachment of drugs to microbubbles, further amplified merits would be anticipated.

Chapter 4

Plane Wave Imaging of Liposome-loaded Microbubbles

A key component of targeted drug delivery using liposome-loaded microbubbles and ultrasound is the ability to track these drug vehicles in real time to guide payload release locally. As a uniquely identifiable emission from microbubbles, the subharmonic signal is of interest for this purpose. Acoustic characterization of liposome-loaded microbubble populations confirmed the decreased pressure threshold for subharmonic emissions (50 kPa vs. 200 kPa for normal microbubbles). This chapter proved the feasibility of subharmonic plane wave imaging of liposome-loaded microbubbles with improved subharmonic sensitivity especially at depth compared to their counterpart of bare (unloaded) microbubbles.

4.1 Introduction

Image guided ultrasound-targeted drug delivery using liposome-loaded microbubbles could become a new approach for cancer treatment (Escoffre *et al.*, 2013), as the toxic chemotherapy agents can be encapsulated and released locally upon the proper stimuli such as high intensity ultrasound. This has significant potential for reduction in side effects compared with a systematic delivery. A key component of this approach is the ability to track these drug vehicles in real time to guide payload release upon their arrival at the desired location. The imaging capability of these drug-loaded microbubbles could be further explored as a biomarker for the treatment response or a tool for drug

dose estimation for personalized medicine (Hudson *et al.*, 2015). Microbubble detection techniques with high sensitivity and less disruption are thus highly preferable for these applications.

The subharmonic emission, with respect to the second harmonic and superharmonic emissions, is exclusive to microbubbles at diagnostic pressure levels (Shi *et al.*, 1999). The potential use of microbubble subharmonic signals has been demonstrated by a range of studies, such as non-invasive blood pressure estimation (Dave *et al.*, 2017), quantification of perfusion (Forsberg *et al.*, 2006), ultrasound molecular imaging Gessner & Dayton (2010), and 3-D ultrasound imaging (Eisenbrey *et al.*, 2012), among others. However, the subharmonic nonlinearity of microbubbles only occurs when an acoustic pressure threshold is exceeded to generate Faraday waves on the bubble surface (Shi *et al.*, 1999). Buckling the microbubble lipid shell gives rise to the reduced acoustic pressure threshold for the initiation of the subharmonic (De Jong *et al.*, 2007). For bare phospholipid-coated microbubbles, gas diffusion from the core into the surrounding liquid could account for shell buckling and microbubbles can be compressed but less expansive in rarefaction phases ('compression-only' behaviour). With attachment of drug filled liposomes to the microbubble shell, ultrahigh-speed optical imaging revealed an 'expansion-only' microbubble behaviour, which mostly happened at low pressures ($<$ 30 kPa) (Luan *et al.*, 2012). In response to the incident acoustic field, liposome-loaded microbubbles undergo expansion, but very limited compression. More recently, acoustic characterization of liposome-loaded microbubble populations confirmed the subharmonic emissions at low pressures (50 kPa) (McLaughlan *et al.*, 2017). It is hypothesized that the decreased threshold for the generation of subharmonic emissions is related to the 'expansion-only' behaviour whereby microbubbles are enforced to a buckled state by the packed liposome layer.

The lower subharmonic threshold for the liposome-loaded microbubbles could be most beneficial for HFR ultrasound imaging by transmitting unfocused waves, whereby the imaging depth is currently limited by the lack of transmission focus. The use of plane-wave contrast imaging has enabled the continuous monitoring of microbubbles with improved contrast (Couture *et al.*, 2012; Viti *et al.*, 2016). As opposed to the line-by-line imaging mode, plane wave imaging spreads the spatial peak acoustic intensity over multiple pulses to preserve the survival rate of microbubbles, as the MI is the key determinant for microbubble destruction.

As unique signals from microbubbles, the subharmonic emissions are of interest to provide consistent contrast response. The aim of this study was to investigate whether the lowered acoustic pressure threshold for the production of subharmonics from liposome-loaded microbubbles could improve their ability to perform subharmonic plane wave imaging.

4.2 Materials and Methods

4.2.1 Manufacture of Liposomes and Microbubbles

Fig. 4.1 shows the diagram of a liposome-loaded microbubble. Liposomes encapsulating propidium iodide were manufactured prior to loading them to microbubbles (Peyman *et al.*, 2012). Propidium iodide was used as the mimicking drug. The phospholipids used for liposomes were prepared by mixing DSPC, cholesterol and DSPE-PEG2000-Biotin (all from Avanti Polar Lipids, Alabaster, AL, USA) all dissolved in chloroform with a molar fraction 62.8%, 32.3% and 4.8%, respectively. Drying chloroform was performed in vacuum for 24 hours. The dried lipid film was then hydrated by addition of 500 μL buffer comprising 1 mg/mL propidium iodide (P4864, Sigma-Aldrich, Dorset, UK). The solution was vortex mixed until all lipids dissolved into it. Liposomes were made by repeatedly extruding the prepared solution through a mini-extruder (Avanti Polar Lipids, Alabama, United States) that was heated to 60 °C on a hot plate. To remove excess propidium iodide, the solution was passed through a column (G-25, GE Healthcare, Buckinghamshire, United Kingdom). Liposomes with a mean diameter of 200 nm were finally manufactured with a concentration of approximately $1x10^{13}$ liposomes/mL.

Unloaded microbubbles were prepared by mixing 84 μL DPPC and 14 μL DSPE-PEG2000-Biotin with a concentration of 20 mg/mL (Avanti Polar Lipids, Alabaster, AL, USA) (Peyman *et al.*, 2012). After the stock chloroform was evacuated in a vacuum desiccator for 24 hours, the dried lipids were re-suspended in 1 mL buffer containing 99% purified water and 1% glycerine (by volume) and 4 mg/mL NaCl in a 1 mL vial. The vial was vortexed for 45 seconds before placed in an ultrasound bath (U50, Ultrawave Ltd., Cardiff, UK) for 15 minutes to facilitate lipid re-suspension. Finally, microbubbles were produced by saturating the prepared lipid solution with perfluorobutane (C_4F_{10})

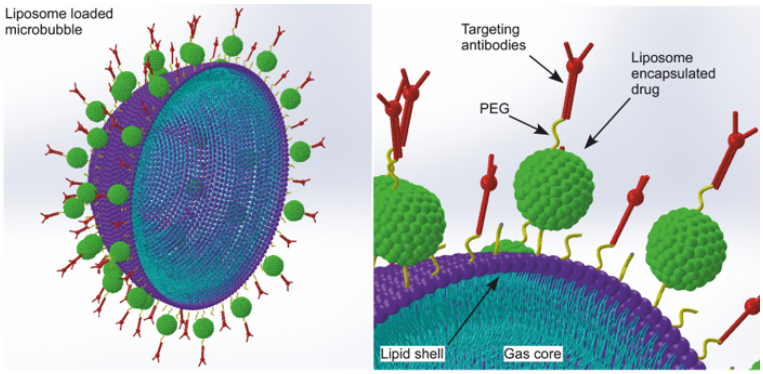

Figure 4.1: Schematic of a liposome-loaded microbubble. Image Courtesy of Dr. James R. McLaughlan at the University of Leeds.

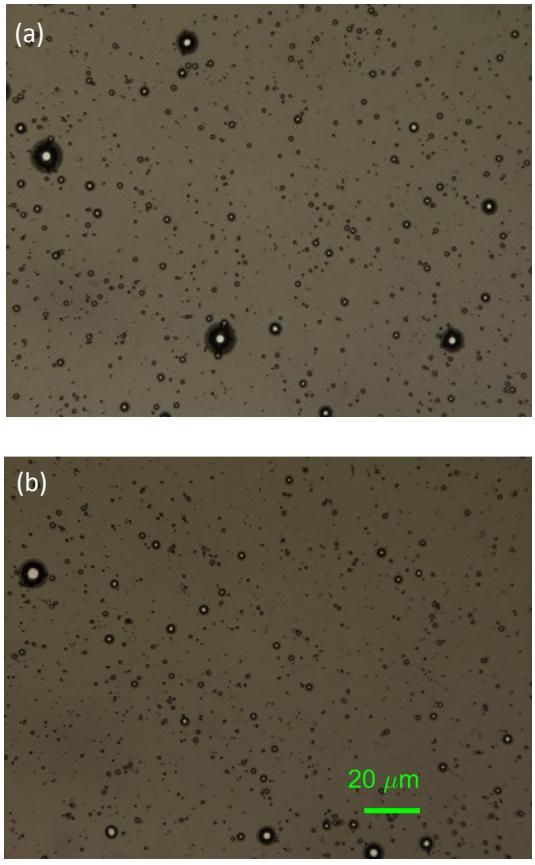

Figure 4.2: (a) Unloaded microbubbles, and (b) liposome-loaded microbubbles viewed under a microscope. 100x diluted.

followed by 15-s shaking using a CapMix mechanical shaker (ESPE, 3M Co., St. Paul, MN).

For liposome-loaded microbubbles, a 200 μL liposome solution was added with 10 μL of NeutrAvidin (A2666, Invitrogen Life Technologies, Paisley, UK), followed by incubation for 20 minutes at room temperature. The liposome solution was then added to a 1 mL unloaded microbubble solution and further incubated for 20 minutes at room temperature to form liposome-loaded microbubbles by linking liposomes to the microbubble shell through biotin-neutravidin binding.

Both types of microbubbles were optically inspected and analysed using an inverted microscope (Eclipse Ti-U, Nikon Instruments Inc., Tokyo, Japan) (Mclaughlan *et al.*, 2013) to determine the microbubble concentration and size distribution. Microbubbles were placed on a slide and imaged under the microscope, see Fig. 4.2. Images were taken and processed through ImageJ. The unloaded and liposome-loaded microbubble solutions showed similar concentrations containing approximately $1x10^{10}$ microbubbles/mL. In all experiments, microbubble solutions were diluted with purified water and a concentration of 1.9 x 10^6 microbubbles/mL was used. A mean diameter of 1.6 $\pm$ 0.9 μm and 1.6 $\pm$ 0.8 μm was found for unloaded and liposome-loaded microbubbles, respectively.

4.2.2 Subharmonic Imaging Setup and Ultrasound Parameters

A TMM wall-less flow phantom (Nie *et al.*, 2018b) was fabricated for the experimental component of this study. A 2.8-mm flow channel was embedded with an oblique angle relative to the transducer-phantom interface. The average attenuation and speed of sound through this TMM was measured to be 0.3 dB/MHz/cm and 1547 m/s, respectively.

Microbubble solutions with a concentration of 1.9 x 10^6 microbubbles/mL were continuously stirred and allowed to homogenize for 20 seconds prior to each measurement. The inlet of the flow channel was connected to a syringe through tubing. The prepared microbubble solutions were pumped through the channel with a mean flow velocity of 20 mm/s.

The UARP II (Boni *et al.*, 2018) equipped with a Verasonics L11-4v probe was used to generate subharmonic plane wave imaging. The transducer had a -6 dB bandwidth

of 90% and a centre frequency at 7.55 MHz. PNPs were measured in water with a 200-μm calibrated needle hydrophone (Precision Acoustics, Dorchester, UK) to determine the MI of 0.09. A pulse sequence of 15 plane waves (6 cycles @ 9 MHz), steered from -5° to 5° with an equal angle step, was emitted with a PRF of 6 kHz. Each pulse sequence was separated by a 2-s period, to transfer the raw data to a local drive and also allow for replenishment of microbubble populations between two acquisitions. Each measurement comprised of 10 transmissions of the sequence and the measurement was repeated for three times. Prior to each measurement, the flow tunnel was thoroughly rinsed with water. Subharmonic plane wave imaging was performed with both types of microbubbles for comparison.

The downloaded channel data was reconstructed offline by delay-and-sum beamforming in Matlab (The MathWorks, Natick, MA, USA). For subharmonic plane wave imaging, the echoes from 15 angled plane waves were coherently summed to retrieve one compounded frame. The RF beamformed data was then filtered using a bandpass filter (3−4.5 MHz), because the subharmonic and the fundamental frequencies spectrally overlap when further increasing the bandwidth of the filter. The filtered data was then Hilbert transformed and the enveloped data was used to calculate the subharmonic amplitude in ROIs as shown in Fig. 4.3 (a).

4.3 Results

Fig. 4.3 shows, from left to right, typical frames acquired for fundamental plane wave imaging with water only, subharmonic plane wave imaging with unloaded and liposome-loaded microbubbles, respectively. Two ROIs of A and B were delimitated by red and green lines as shown in Fig. 4.3(a), and the corresponding subharmonic amplitudes for both types of microbubbles are given in Fig. 4.4. Fig. 4.3(b) shows that the subharmonic signals from unloaded microbubbles diminish with depth. For subharmonic plane wave imaging, Fig. 4.4 shows that the average subharmonic intensity in ROI B is higher with liposome-loaded microbubbles, and the intensity difference with these two types of microbubble populations has been significantly larger in ROI A. These occurred due to the lack of the transmit focusing with plane waves. The acoustic pressure was gradually attenuated with depth and lower than the threshold to elicit subharmonic responses for unloaded microbubbles. However, for liposome-loaded microbubbles, subharmonic

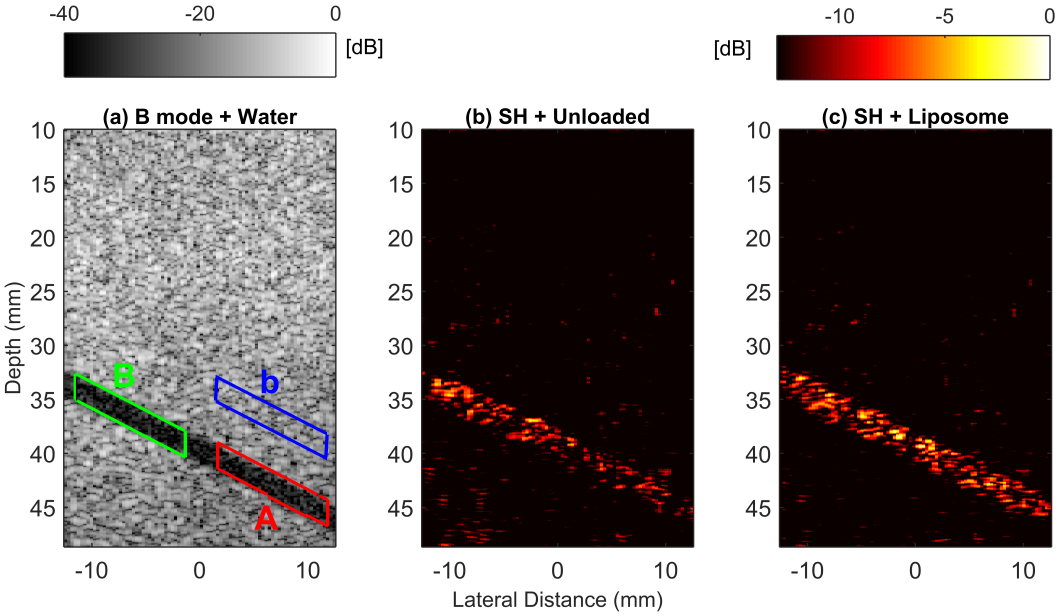

Figure 4.3: (a) B-mode image showing ROIs. Subharmonic images with (b) unloaded microbubbles, and (c) liposome-loaded microbubbles. SH: subharmonic.

nonlinearity sets in with a reduced acoustic pressure threshold, and this enables higher subharmonic sensitivity particularly at deep locations as shown in Fig. 4.3(c).

4.4 Discussion

Apart from the microbubble size and shell composition, the amplitude of the subharmonic is affected by a number of acoustic factors, such as the frequency and length of the excitation signal. Generally, the subharmonic response is enhanced when a microbubble is driven by a long-duration excitation signal with a frequency twice of its resonance. The use of broadband chirp excitations is thus broadly investigated to improve subharmonic imaging of microbubbles, by exciting the polydisperse microbubble populations with frequencies near their resonances (Harput *et al.*, 2013). When using a single chirp excitation, the fractional Fourier transform could be further exploited to extract spectrally overlapped components within the fractional Fourier domain for subharmonic microbubble imaging. Acoustic characterisation of the microbubble populations could also benefit subharmonic imaging when providing the accurate resonance

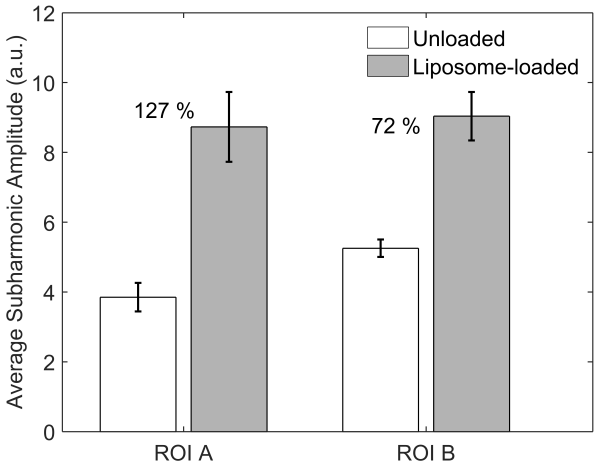

Figure 4.4: The average subharmonic amplitude and relative amplitude difference in percentage for ROI A and ROI B (results based on 10 x 3 = 30 measurements).

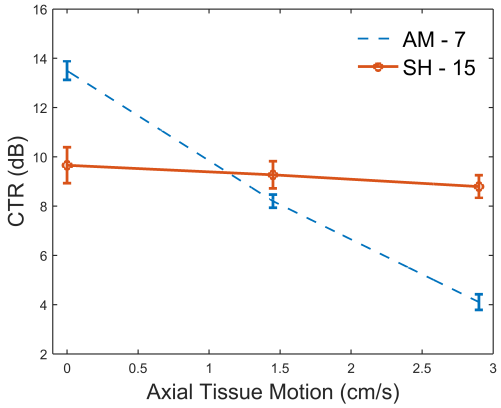

Figure 4.5: Effects of tissue motion on CTR for AM and subharmonic plane wave imaging. The numbers of 7 and 15 indicate the number of steering angles for compounding.

frequency. The effects of the number of liposomes linked to the microbubble on subharmonic emissions need to be explored in the future.

A lot of techniques such as AM and PI (Eckersley *et al.*, 2005), exist in commercial systems for contrast-enhanced imaging through exploiting nonlinear fundamental and second harmonic oscillations of the microbubble. Whereas the use of PI and AM could provide an improvement of contrast, the nature of nonlinear wave propagation hampers their ability to discriminate microbubbles and tissue. Additionally, tissue motion results in decorrelation of tissue signals within the PI or AM packet, leaving residual signals but misclassified as contrast (Viti *et al.*, 2016). The influence of tissue motion on CTR with liposome-loaded microbubbles, if any, was investigated through artificially displacing the raw channel data with subharmonic plane wave imaging (Gong *et al.*, 2018). The tissue motion of 1.4 or 2.8 cm/s was simulated in the direction of ultrasound propagation. For comparison, AM plane wave imaging with a 2-pulse packet was designed. The excitation signal was a 3-cycle 4.5 MHz sinusoid tapered with a Tukey window (coefficient: 0.2). The same PRF of 6 kHz, MI of 0.09 and the 10° sector angle as those employed for subharmonic plane wave imaging were used. But the number of scanning angles was reduced to 7 in one pulse sequence. This configuration was determined so that the imaging time for a final compound image was comparable to that for subharmonic plane wave imaging. Fig. 4.5 shows the CTR measurements between ROIs B and b with varied artificial tissue speeds. For AM, the CTR is significantly susceptible to tissue motion, while this is not the case for subharmonic plane wave imaging. This might suggest that when using plane waves, subharmonic imaging is more suitable for the quantitative applications of microbubbles, such as perfusion imaging and quantification of liposome-loaded microbubbles.

4.5 Conclusion

The present study experimentally demonstrated subharmonic plane wave imaging of liposome-loaded microbubbles with improved sensitivity compared to that with unloaded microbubbles. This could be explained by that liposome-loaded microbubbles are able to generate the subharmonic response at a reduced pressure threshold, through naturally forcing bubbles to the buckling state by the loaded liposome layer. This tech-

nique could be used for specifically tracking the drug payload loaded on microbubbles and has the potential for drug volume estimation.

Chapter 5

HFR Contrast-Enhanced Echocardiography Using Diverging Waves: 2-D Motion Estimation & Compensation

Combining diverging ultrasound waves and microbubbles could improve contrast-enhanced echocardiography (CEE), by providing enhanced temporal resolution for cardiac function assessment over a large imaging field of view. However, current image formation techniques using coherent summation of echoes from multiple steered diverging waves, are susceptible to tissue and microbubble motion artefacts, resulting in poor image quality. In this chapter, correlation-based 2-D motion estimation was used to perform motion compensation for CEE using diverging waves. The accuracy of this motion estimation method was evaluated with Field II simulations. The root-mean-square velocity errors were 5.9% $\pm$ 0.2% and 19.5% $\pm$ 0.4% in the axial and lateral directions, when normalized to the maximum value of 62.8 cm/s which is comparable to the highest speed of blood flow in the left ventricle (LV). The effects of this method on CR and CNR were tested *in vitro* using a tissue mimicking rotating disk with a diameter of 10 cm. Compared against the control without motion compensation, a mean increase of 12 dB in CR and 7 dB in CNR were demonstrated when using this motion compensation method. The motion correction algorithm was tested *in vivo* on a CEE dataset acquired with the UARP II performing coherent diverging wave imaging. Improve-

ment of the B-mode and contrast-mode image quality with cardiac motion and blood flow induced microbubble motion was achieved. The results of motion estimation were further processed to interpret blood flow in the LV. This allowed for a triplex cardiac imaging technique, consisting of B mode, contrast mode and 2-D vector flow imaging with a frame rate of 250 Hz.

5.1 Introduction

Microbubbles are micron-sized spheres with a heavy gas core that is stabilized by a shell made of lipids, polymers, proteins, or surfactants (Mulvana *et al.*, 2017). Due to their significant acoustic impedance mismatch relative to the surrounding tissue and blood cells, they are excellent ultrasound scatters and have long been used as ultrasound contrast agents (Qin *et al.*, 2009). Additional advances in understanding their nonlinear oscillations, when subject to an ultrasound field, underpin a number of microbubble-specific detection techniques such as PI (Simpson *et al.*, 1999) and AM (Eckersley *et al.*, 2005), granting insight into the microcirculation and hence perfusion(Tremblay-Darveau *et al.*, 2014, 2016a).

In cardiology, the use of microbubbles is recommended when more than 20% of the left ventricle (LV) endocardium is not clearly visible (Olszewski *et al.*, 2007). Contrast-enhanced echocardiography (CEE) is routinely used in the clinic for LV opacification, endocardial border definition, regional wall motion assessment, and LV mass diagnosis, among others (Porter *et al.*, 2018; Senior *et al.*, 2009). However, most conventional echocardiography is limited by a trade-off between the imaging field of view, temporal resolution, and spatial resolution due to the use of the conventional line-by-line scanning mode (Cikes *et al.*, 2014). For 2-D ultrasound imaging, a typical frame rate ranging from 30 to 80 Hz (Poree *et al.*, 2016) is sufficient for assessment of cardiac morphology, but insufficient for resolving short-lived cardiac events such as isovolumic acceleration (Cikes *et al.*, 2014) or complex intra-cardiac blood flow (Toulemonde *et al.*, 2017c). The accurate estimation of ventricular flow patterns by CEE using regular frame rates together with Navier-Stokes regularization has been demonstrated (Cimino *et al.*, 2012), but a substantial cut-off for the estimation of the high velocities exists due to the limited frame rate. Thus, the use of HFR CEE with a large imaging field of view could lead

to better assessment of cardiac function through visualisation and quantification of transient events not captured with current CEE techniques.

Improving the temporal resolution of echocardiography is an active area of research (Cikes *et al.*, 2014). One method is multi-line acquisition (MLA) (Shattuck *et al.*, 1984), wherein multiple receiving lines, typically 4 (Cikes *et al.*, 2014), are beamformed simultaneously from one weakly-focused transmission. However, the broadened beam in this method results in reduction of lateral resolution. Recent engineering advances in open ultrasound platforms such as the customization of the transmit waveform on each channel (Boni *et al.*, 2018), have allowed for the development of new HFR cardiac imaging techniques. Multi-line transmission is an example of this, and considered an alternative approach to MLA (Tong *et al.*, 2014, 2016; Zurakhov *et al.*, 2018). In this technique, multiple focused ultrasound beams, typically 4 (Poree *et al.*, 2016), are simultaneously transmitted to reduce the time needed to sweep the whole ROI. However, these multiple transmit beams overlap in the nearfield (Santos *et al.*, 2015), which might disrupt microbubbles significantly due to the increased MI, limiting its use for contrast-enhanced ultrasound. Another alternative to MLA is to transmit non-focused diverging waves (Fadnes *et al.*, 2017; Grondin *et al.*, 2017; Hasegawa & Kanai, 2011; Osmanski *et al.*, 2014; Papadacci *et al.*, 2014; Toulemonde *et al.*, 2016), where a full field-of-view 2-D image can be reconstructed from a single transmission. The image degradation due to the lack of transmit focusing can be minimised by coherent spatial compounding (Papadacci *et al.*, 2014) by sacrificing the imaging frame rate. As with synthetic transmit aperture imaging (Chen *et al.*, 2014; Gammelmark & Jensen, 2014; Kim *et al.*, 2002; Yiu *et al.*, 2008) and coherent plane wave imaging (Denarie *et al.*, 2013; Ekroll *et al.*, 2015), where synthetic summation of low-resolution images (LRIs) is required for a high-resolution image (HRI), coherent diverging wave imaging is susceptible to motion artefacts. The complex and nonrigid motion of the myocardium (Tong *et al.*, 2016) and pulsatile microbubble populations (Voorneveld *et al.*, 2017) in heart chambers could result in these artefacts, causing contrast and spatial resolution degradation in the compound image. Thus, further development of methods to preserve the efficacy of spatial compounding for HFR CEE using diverging waves is needed.

Doppler-based motion compensation has been proposed for HFR echocardiography using diverging waves (Joos *et al.*, 2018; Poree *et al.*, 2016). This technique which only accounts for axial motion, works well for the compensation of myocardial motion

but might not be ideal for HFR CEE. In the first instance, Doppler aliasing could happen in the LV, causing incorrect estimation and hence incorrect compensation. In addition, axial motion compensation alone could be insufficient when the total lateral motion is large in comparison to the wavelength (Harput *et al.*, 2018), which might be true for the fast-flowing microbubbles in the LV. Recently, an image registration algorithm adapted from magnetic resonance imaging, was applied to HFR CEE using phase-inverted diverging waves (Toulemonde *et al.*, 2017b), to correct motion artefacts *in vivo*. In this case, the determination of the reference frame is crucial and may result in compensation failure if the chosen reference frame has a low SNR.

In this study, a two-stage motion estimation method was applied to HFR CEE using diverging waves (Poree *et al.*, 2016; Toulemonde *et al.*, 2017c), to restore the quality of the coherent compound image by compensating for motion between steered diverging waves. This approach was evaluated both *in vitro* and *in vivo*. Without additional pulse transmissions, the results of motion estimation were also leveraged for 2-D vector blood flow mapping in the LV *in vivo*. This allowed for the implementation of a HFR triplex cardiac imaging tool, by simultaneously performing B-mode imaging, contrast-mode imaging and 2-D vector flow mapping.

5.2 Materials and Methods

5.2.1 Motion Estimation and Compensation

In this study, motion is defined as the combination of myocardial tissue motion, probe motion due to freehand scanning, and blood flow induced microbubble motion in heart chambers. We use a correlation-based 2-D motion estimation method to get subpixel displacements between adjacent tilted diverging wave emissions. Based on these estimated displacements, motion compensation is then performed by aligning image pixels of all LRIs prior to coherent summation. For motion compensation in ultrasound imaging using unfocused beams, the first LRI in the set (Yiu *et al.*, 2008), the central LRI (Toulemonde *et al.*, 2017b) or the $\frac{N}{2}$th LRI (where N is even) (Poree *et al.*, 2016) has been used as the reference for registration. In this study, all LRIs are heuristically registered to the first LRI within the sequence that is used for coherent compounding. The processing chain is shown in Fig. 5.1.

Two-stage Motion Estimation

A constant velocity for each estimation point was assumed during transmitting a diverging wave compounding sequence (a 4 ms period in this study as given in Section 5.2.2). Two-stage motion estimation was applied to the beamformed RF LRIs prior to coherent compounding in the polar grid. This approach was comprised of two stages. The first used rigid block matching (Leow *et al.*, 2015) with interrogation windows of identical size, and the second used iterative window refinement to improve resolution. Both stages were based on cross correlation.

To improve the robustness of the coarse estimations in the first stage, block matching was performed with correlation correction (Nie *et al.*, 2016), achieved by sequentially multiplying all available correlation maps from successive pairs of LRIs. Cross correlation was performed in the frequency domain and the peaks in the correlation functions were used to estimate the average displacements of interrogation windows. The subpixel motion estimations were then found by fitting the three-point Gaussian function in the proximity of the correlation peak (Niu *et al.*, 2010).

In the second stage, an iterative scheme was adopted for each pair of adjacent LRIs, wherein the interrogation windows were resized and deformed based on the results of motion estimation from a previous iteration. Window resizing was performed with the current window having a half radial size and a half angular size compared to the values used in the previous iteration. Window deformation was used for accommodating nonrigid motion and it was achieved by the first-order approximation of the local displacement field (Niu *et al.*, 2010; Scarano, 2001). The second stage was initialized with a motion estimation field from the first stage as shown in Fig. 5.1. In each iteration, new cross correlation functions were performed using the size-reduced and deformed interrogation windows, and the remaining displacement was accumulated to improve the local estimation accuracy. As the interrogation window size was further decreased in each iteration, the spatial resolution of motion estimation was improved. But there was a tradeoff between the spatial resolution of motion estimation (a smaller window size) and the computational complexity because of the need of more iterations. The maximum number of iterations was fixed to two in this study and more discussion about this arrangement can be found in Section 5.4.1. Between the iterations, subpixel

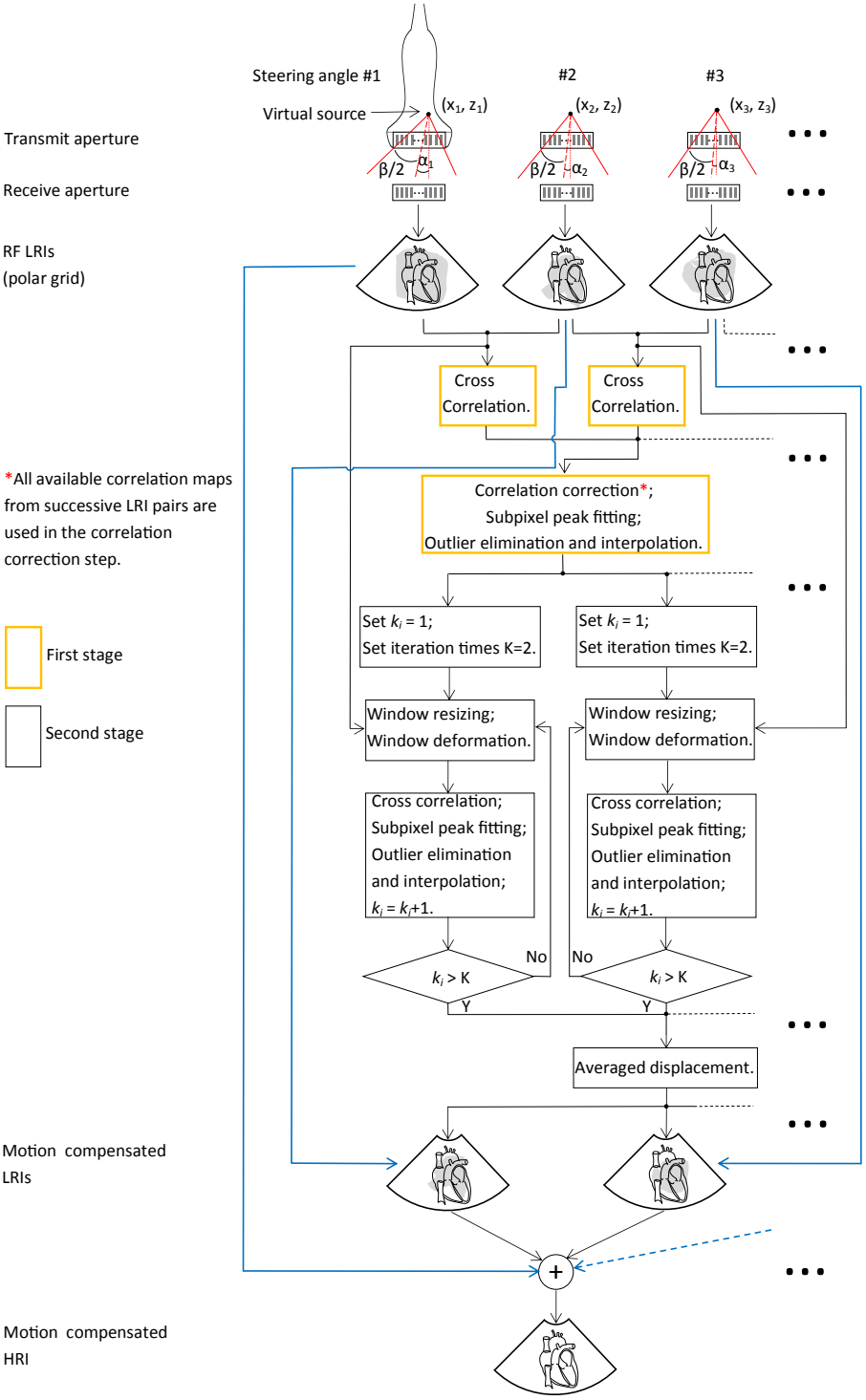

Figure 5.1: Workflow of the proposed diverging wave imaging approach with motion compensation. Motion estimation and compensation are performed within a pulse sequence that is used to form a HRI. β is not changed for different steering angles. α_1, α_2 and α_3: steering angles. β: divergent angle.

peak fitting was also performed on the new cross correlation functions which improved the accuracy of window deformation (Niu *et al.*, 2010).

A local median filter (Westerweel & Scarano, 2005)($\varepsilon = 0.02$, threshold $= 2$, $b = 1$) and a filtering method (Joos *et al.*, 2018) using global standard deviations ($\delta = 5$) were used to remove outliers for the first stage and each iteration in the second stage. Outlier vectors were replaced with linear interpolated values from nearest neighbours and the results of motion estimation were then smoothed by means of a least-squares method (Garcia, 2010). After two iterations, the displacement information at the centre of each interrogation window was found with each successive pair of LRIs. For each interrogation window, the displacement estimations from all successive pairs of LRIs were averaged to improve the accuracy. The displacement for each pixel was then obtained by linearly interpolating these averaged displacements at the window centres.

Application of Motion Compensation to HFR CEE Using Diverging Waves

A nonlinear imaging scheme AM (Eckersley *et al.*, 2005) was used for HFR CEE in this study. At each steering angle, a 2-pulse AM packet was transmitted, with the first pulse transmission having a full amplitude and the second one having a half amplitude. The echo from the full-amplitude transmission and twice of the sign-inverted echo from the half-amplitude transmission were combined before compounding. With the full-amplitude transmissions, a synchronized B-mode imaging sequence was acquired.

In comparison to half-amplitude transmissions, the full-amplitude transmissions provided an improved SNR. Two-stage motion estimation was thus performed on the LRIs from full-amplitude transmissions. Relocation of the image pixels was then applied to both low-resolution B-mode (RF) images and AM contrast-mode (RF) images before coherently summing them together. Linear interpolation of the LRI intensities was adopted to accommodate the subpixel accuracy of the motion estimations.

5.2.2 Imaging Setup

For diverging wave imaging, 4-cycle 2.78 MHz ultrasound pulses with either a full or half amplitude were transmitted, emanating diverging waves using the full aperture (Poree *et al.*, 2016). The 4-cycle excitation signals were tapered using a Tukey window with a coefficient of 0.2. The divergent angle β that was determinant to the imaging field of

view was set to 90°, as used in (Poree *et al.*, 2016). All *in vitro* and *in vivo* measurements were performed with the UARP II equipped with a Verasonics P4-2v transducer (Verasonics, Inc., WA, USA). The UARP II is capable of arbitrary waveform generation on each channel (Cowell & Freear, 2008; Smith *et al.*, 2013) which permits the accurate pressure modulation needed for nonlinear contrast-enhanced imaging with AM. The phased array transducer P4-2v had a −6 dB bandwidth of 60% and a centre frequency of 2.78 MHz. Acoustic pressures were measured at room temperature (21°C) in degassed and deionized water with a calibrated 200-μm needle hydrophone (Precision Acoustics, Dorchester, UK). The MI (Apfel & Holland, 1991; Church, 2005) was set to 0.12 with a derating factor of 0.3 dB/MHz/cm. The parameters for both *in vitro* and *in vivo* measurements are given in Table 5.1. For both B-mode and contrast mode imaging in this study, a Hamming window was used to design a bandpass filter with cut-off frequencies at 1.9 MHz and 3.6 MHz, matching the −6 dB bandwidth of the transducer.

To match the frame rate of 250 Hz as demonstrated in (Poree *et al.*, 2016; Toulemonde *et al.*, 2017c), a sequence of 16 pulse transmissions (2-pulse AM packet at each steering angle as illustrated in Section 5.2.1) was designed with a PRF of 4 kHz. To facilitate coherent compounding, the DWs were steered at varied angles while keeping the divergent angle β unchanged. The step between steering angles for motion estimation was fixed to 2° which is similar to 1.8° in (Joos *et al.*, 2018). Instead of using a pulse sequence with a constant angle step (−7°: 2°: 7°), the maximum steering angle was heuristically set to 10°. The resulting arrangement for steering angles was: −10°, −8°, −6°, −4°, 4°, 6°, 8°, 10°. This approach was to achieve an improved lateral resolution with coherent compounding, as the larger angular range gives lower sidelobe levels for the equivalent number of steering angles (Alomari *et al.*, 2014). The improved lateral resolution with the proposed sequence was demonstrated by measuring a point spread function using the UARP II. In degassed and deionized water, a wire target with a diameter of 150 μm was placed at the depth of 60 mm relative to the transducer surface, which matched the elevation focus of the transducer. The improved −6 dB lateral resolution of 2.1 mm was obtained when using the proposed sequence for both fundamental B-mode imaging and the contrast mode using AM. Whereas this value was 2.3 mm with the normal sequence that used an equal angle step (−7°: 2°: 7°). However, regardless of the optimisation, motion will always interfere with coherent diverging

Table 5.1: Parameters for Both *in vitro* and *in vivo* Measurements

Parameter	Value
Apodization in transmit	Rectangular window
Apodization in receive	Rectangular window
Sampling frequency for transmit	160 MHz
Sampling frequency for receive	20 MHz
Divergent angle β	90°
PRF	4 kHz
Imaging scheme	AM (see Section 5.2.1)
Steering angles	(−10°, −8°, −6°, −4°, 4°, 6°, 8°, 10°)
Excitation signal	4-cycle sinusoid (2.78 MHz)
Tapering function on excitations	Tukey (coefficient: 0.2)
MI	0.12 (derating factor: 0.3 dB/MHz/cm)

wave compounding. This study focuses on the demonstration of the feasibility to make motion compensation to preserve the quality of HFR CEE when using diverging waves.

5.2.3 Evaluation with a Rotating Disk

Accuracy of Motion Estimation

The accuracy of the motion estimation method was evaluated by using Field II simulations (Jensen & Svendsen, 1992). The transducer P4-2v that was used for both *in vitro* and *in vivo* measurements was simulated. Acoustic attenuation was not considered in the calculation. As motion estimation was performed with the linear LRIs from full-amplitude ultrasound pulses, AM pulse transmissions were not simulated. The simulation parameters are given in Table 5.2. A cylindrical phantom was simulated with a density of 10 scatters per resolution cell, generating a fully-developed speckle pattern (Gammelmark & Jensen, 2014). It had a thickness of 10 mm in the elevation direction and a disk diameter of 10 cm. No anechoic cysts were embedded. The

Table 5.2: Parameters for Field II Simulations

Parameter	Value
Number of elements	64
Pitch size	0.3 mm
Element height	13 mm
Elevation focus	60 mm
Centre frequency	2.78 MHz
Bandwidth (−6 dB)	60%
Speed of sound	1540 m/s
Sampling frequency for transmit	160 MHz
Sampling frequency for receive	20 MHz
Excitation signal	4-cycle sinusoid (2.78 MHz)
Tapering function on excitations	Tukey (coefficient: 0.2)
Apodization in transmit	Rectangular window
Apodization in receive	Rectangular window
Divergent angle β	90°
Steering angles	(−10°, −8°, −6°, −4°, 4°, 6°, 8°, 10°)

Table 5.3: Parameters for Beamforming and Motion Estimation

Parameter	Value
Radial pixel size	38.5 μm
Angular pixel size	0.0625°
Window size (1st stage)	152x84 (radial and angular lines)
Window size (2nd stage)	76x42; 38x21
Window overlap	50%

phantom was placed at the depth of 88 mm, and rotated at 4π rad/s with repeated insonifications by the 8-pulse transmission sequence ($-10°$, $-8°$, $-6°$, $-4°$, $4°$, $6°$, $8°$, $10°$) with a PRF of 2 kHz. The velocity of the disk achieved its maximum at the outer boundary with a value of 62.8 cm/s which is comparable to the highest speed of blood flow in the LV (Beeri *et al.*, 1998). In all simulations, white Gaussian noise was added to the RF data before beamforming giving a SNR of 30 dB.

The raw datasets were beamformed in a polar grid (90° wide) using the delay-and-sum approach in Matlab (The MathWorks, Natick, MA, USA). Two-stage motion estimation was then performed with LRIs. Parameters used for beamforming and motion estimation are summarized in Table 5.3. The estimated subpixel-wise displacements were then used to counter-shift the LRIs and correct for incoherence between angled diverging waves, enabling coherent compounding. The operation details of motion estimation and compensation are given in Section 5.2.1. Motion estimation between the frames with steering angles $-4°$ and $4°$ was not performed because of the large angular step of 8° (2° between other steered diverging waves) and the associated low image correlation (Jespersen *et al.*, 1998). More discussion about this operation is given in Section 5.4.1.

The root-mean-square (RMS) velocity errors (Fadnes *et al.*, 2017) were calculated from ten repeat simulations, with a different noise value added to each repeat. The RMS velocity errors were then normalized to the maximum speed of the disk.

Effects of Motion Compensation on Image Quality

An agar-based tissue-mimicking rotating disk (Nie *et al.*, 2018b) was fabricated for evaluating the effect of the proposed method on image quality *in vitro*. The average speed

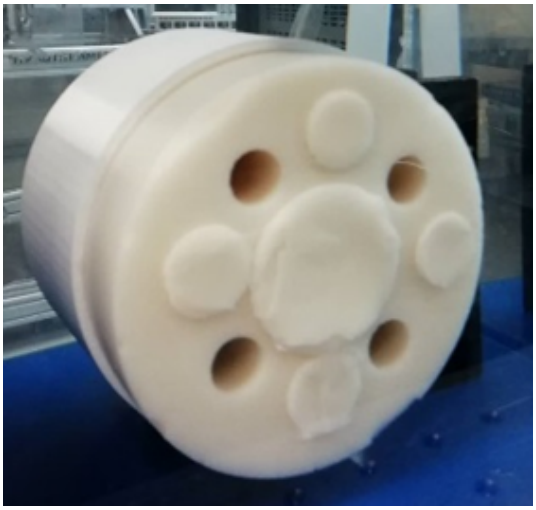

Figure 5.2: Photograph of the rotating disk for *in vitro* experiments.

of sound and attenuation through this phantom was 1540 m/s and 0.55 dB/MHz/cm, respectively (Browne *et al.*, 2003). The disk had a 10-cm diameter and four equidistant 12.8-mm anechoic cysts located at 32 mm relative to the disk centre. It was mounted to the shaft of a stepper motor controlling the rotation speed at 4π rad/s. The phantom was placed at the same depth of 88 mm as used for simulations. Fig. 5.2 shows the photograph of the *in vitro* rotating disk. The ultrasound parameters are given in Table 5.1. The effect of motion compensation was investigated only on B-mode imaging due to the absence of microbubbles. The benchmark of these measurements was determined by imaging the disk in a static state. Beamforming, motion estimation and compensation were performed off line using Matlab (Table 5.3).

The performance of the proposed method was quantitatively analysed by calculating the CR and CNR with the ROIs as shown in Fig. 5.3 (Chen *et al.*, 2018)

$$\mathrm{CR} = 20\log_{10}\left(\frac{\mu_{\mathrm{bg}}}{\mu_{\mathrm{cyst}}}\right), \tag{5.1}$$

$$\mathrm{CNR} = 20\log_{10}\left(\frac{\mu_{\mathrm{bg}} - \mu_{\mathrm{cyst}}}{\sqrt{\sigma_{\mathrm{bg}}^2 + \sigma_{\mathrm{cyst}}^2}}\right), \tag{5.2}$$

where μ_{bg} and μ_{cyst} are the mean image intensities (enveloped data before log-compression) within the background and cyst regions. σ_{bg} and σ_{cyst} denote their cor-

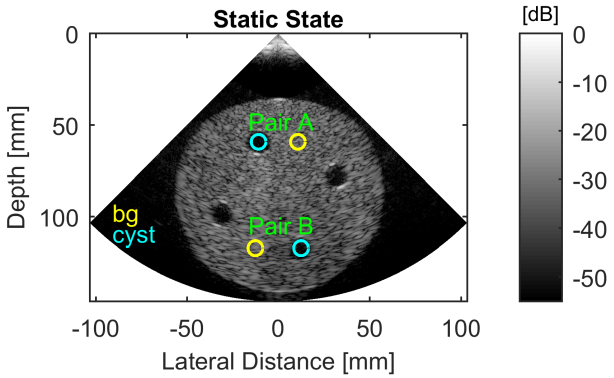

Figure 5.3: Illustration of ROIs used for quantitative analysis of CR and CNR. All circular ROIs have a diameter of 8 mm. bg: background.

responding standard deviations.

Two pairs of 8-mm diameter ROIs at different depths were defined in Fig. 5.3, and two ROIs in each pair were positioned at the same depth.

5.2.4 *In Vivo* Investigations

The *in vivo* data of apical two-chamber view was acquired from a healthy volunteer using the UARP II and SonoVue microbubbles (Bracco S.p.A, Milan, Italy). The acquisition was performed with handheld scanning utilizing the same probe and acoustic parameters used for *in vitro* validation (Table 5.1). The on-line B-mode imaging sequence using focused beams was used to guide the probe alignment and time the trigger of the AM diverging wave sequence. For real-time imaging feedback, the beams were focused at the depth of 10 cm with a MI of 0.25. The corresponding excitation signal was a 3-cycle 2.5 MHz sinusoid tapered with a Tukey window (coefficient: 0.5). The AM diverging wave scanning lasted for 1.4 seconds covering one cardiac cycle and the corresponding data was subsequently post-processed in Matlab.

The operation of beamforming and motion estimation was carried out with the parameters shown in Table 5.3, except the imaging depth was decreased to 12.6 cm from 14.6 cm to cover the LV. The RF images from the full-amplitude transmissions were used for motion estimation and compensation was then applied to both B-mode imaging and contrast-mode imaging. The results of motion estimation were simultaneously leveraged

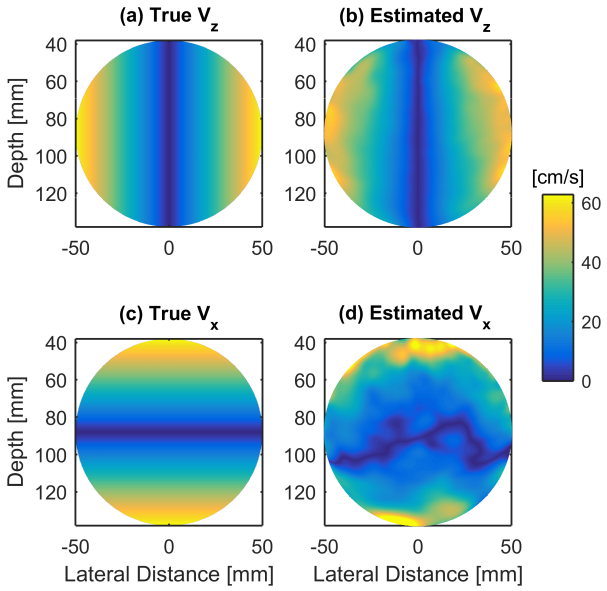

Figure 5.4: Estimated absolute velocities in the axial and lateral directions using Field II are compared to their theoretical true values. V_z: velocity in the axial direction; V_x: velocity in the lateral direction. The values are reported from one simulation.

for 2-D vector blood flow mapping in the LV. No temporal averaging was applied to smooth the velocity profile.

5.3 Results

5.3.1 Rotating Disk Studies

Accuracy of Two-Stage Motion Estimation

Fig. 5.4 shows the absolute velocities from the Field II simulation. These results show that the axial motion estimation was more accurate than the lateral motion estimation. Based on ten repeat simulations, the RMS velocity errors were 5.9% $\pm$ 0.2% and 19.5% $\pm$ 0.4% for the axial and lateral directions, respectively. In addition to improving the quality of the compound images, the results of motion estimation could be encoded to depict the complex blood flow patterns in the LV as demonstrated later in Section 5.3.2.

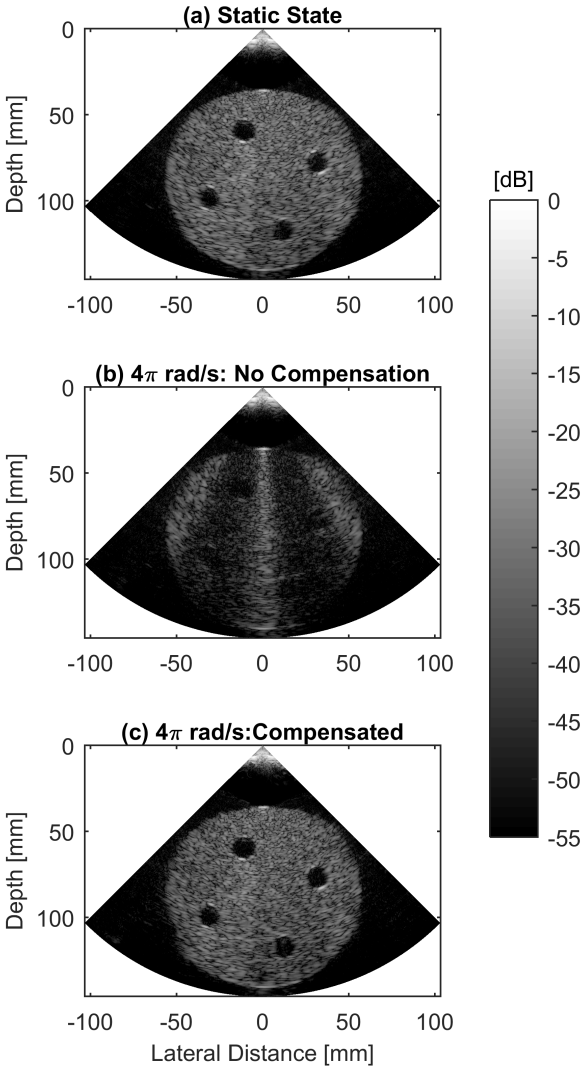

Figure 5.5: Compound images of the *in vitro* disk in the (a) static state, and the rotating state (b) without and (c) with motion compensation.

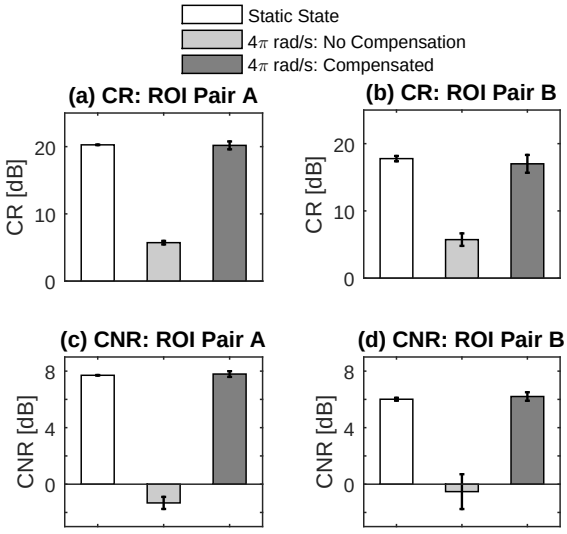

Figure 5.6: Quantitative CRs and CNRs for two pairs of ROIs as shown in Fig. 5.3. The mean values and standard deviations are from four repeat measurements.

Effects of Motion Correction on Image Quality

The images in Fig. 5.5, from top to bottom, show the *in vitro* disk in the static state as benchmark, in the spinning state without and with the integration of motion compensation, respectively. In comparison to Fig. 5.5(a), the benchmark, direct coherent diverging wave imaging in the presence of motion resulted in substantial artefacts due to incoherence between angled diverging waves, as shown in Fig. 5.5(b). Qualitatively, exploiting motion between angled diverging waves and applying motion compensation to LRIs prior to compounding yielded a significant improvement in image quality as shown in Fig. 5.5(c).

Quantitatively, the CRs and CNRs for two pairs of ROIs as given in Fig. 5.3 are summarized in Fig. 5.6. Both CRs and CNRs have been restored for ROI pairs A and B with motion compensation, obtaining comparable values to the references in all cases. Without motion compensation, the CR and CNR have decreased by approximately 12 dB and 7 dB (mean values for two ROI pairs). The depth of the ROI affected the standard deviations for both CRs and CNRs. A larger standard deviation was observable for all measurements in ROI pair B, placed at a deeper location. Due to acoustic attenuation, a lower SNR is expected in a deeper region, accounting for this

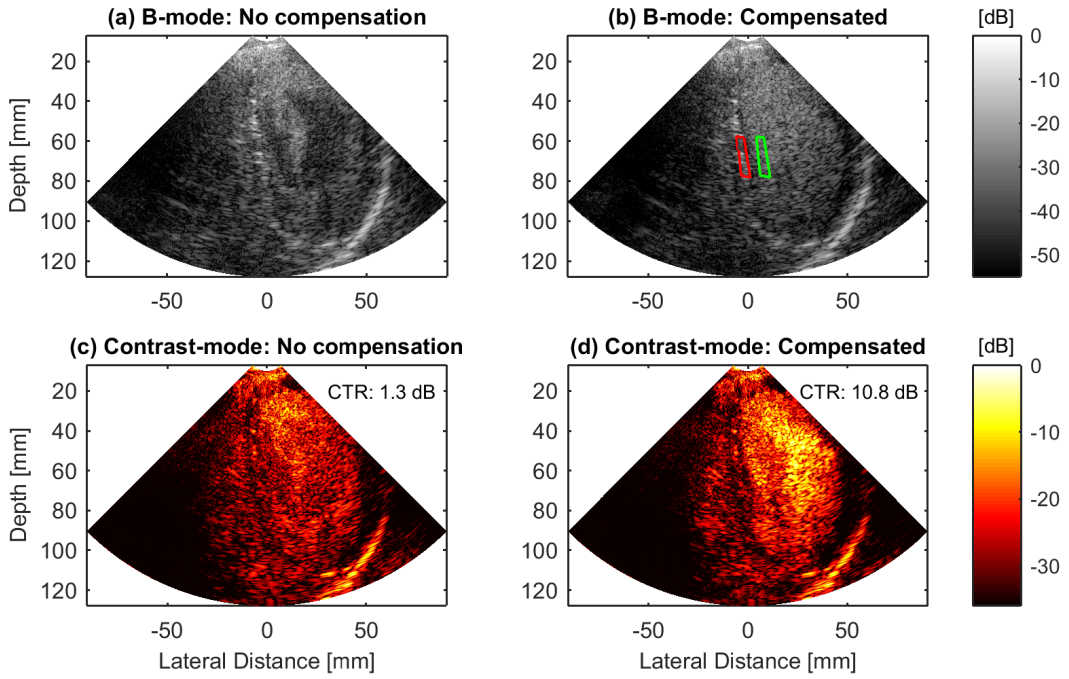

Figure 5.7: Synchronized B-mode and contrast-mode compound images from the same AM pulse sequence consisting of 16 pulse transmissions. All 16 transmissions were used for (c) and (d), and 8 full-amplitude transmissions were combined for (a) and (b). Motion compensation was applied to (b) and (d).

observation. But without the application of motion compensation, the information in the compound image (Fig. 5.5b) has been lost.

5.3.2 *In Vivo* Results

Fig. 5.7 shows beamformed frames from the diverging wave scanning sequence covering one cardiac cycle. Two full video clips are provided as the supplementary material (Supplementary Video S1, played back at its acquisition rate of 250 fps and Supplementary Video S2, played back at 50 fps, https://ieeexplore.ieee.org/document/8580591).

The quality of the *in vivo* cardiac images was improved when integrated with motion compensation (Fig. 5.7). This improvement was visible on B-mode images. For example, without the use of motion compensation, the microbubbles appeared to be unevenly distributed in the LV, resulting in a total dark region in the vicinity of the septum (Fig. 5.7a). However, when using compensation it is clear that the microbub-

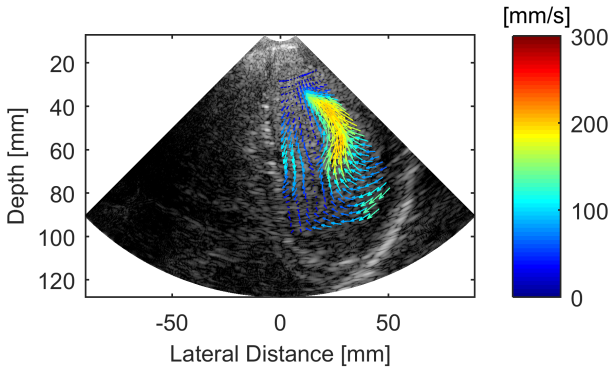

Figure 5.8: Composite image of the LV by superimposing flow vectors onto its corresponding B-mode image. These two types of information were obtained from the same RF data as used for Fig. 5.7. The B-mode background is the same as shown in Fig. 5.7(b).

bles were present throughout the LV (Fig. 5.7b). This enhancement can also be applied to contrast-enhanced imaging, which benefits from the preserved efficiency of coherent compounding with motion correction when comparing Fig. 5.7(c) and (d). The CTR (Toulemonde *et al.*, 2018) between the LV (green box in Fig. 5.7b) and the surrounding tissue region (red box in Fig. 5.7b) was calculated for Fig. 5.7(c) and (d). The delineation of the endocardial border is enhanced thanks to the improvement of CTR in Fig. 5.7(d) (10.8 dB compared to 1.3 dB in Fig. 5.7c). The results of motion estimation for Fig. 5.7(b) and (d) were further processed to render blood flow vectors in the LV. The combination of vector flow mapping and B-mode imaging is shown in Fig. 5.8. These flow vectors were from the last-iteration motion estimation but with a decimation factor of 1/4 along both directions for clarity. Two full videos showing 2-D vector blood flow mapping in the LV have been integrated within the same supplementary material including B-mode and contrast-mode images (`https://ieeexplore.ieee.org/document/8580591`). Fig. 5.8 demonstrates that the blood flow reaches its maximum velocity within the same region that is dark in Fig. 5.7(a) and (c).

5.4 Discussion

Motion is unavoidable in ultrasound imaging, with induced artefacts present as geometric distortion of organ structures when using the focused-beam imaging paradigm, but present as significant deterioration of image contrast/resolution when using coherent diverging wave imaging. For HFR CEE using diverging waves, correction of probe, myocardial and microbubble motion in the LV is necessary to restore the image quality impaired by incoherence between the angled diverging waves. Compensation of blood flow induced microbubble motion in the LV proved beneficial to segment myocardium with an improved CTR, as shown in Fig. 5.7(d). This demonstrates the relevance of the proposed motion compensation method for this application *in vivo*. A synchronized B-mode imaging sequence is also available in other nonlinear imaging schemes including PI and CPS. This approach could be used to correct motion artefacts for coherent diverging wave imaging based on PI and CPS.

5.4.1 Selection of Parameters

As values reported in Fig. 5.6 are parameter-related, they could change as a function of multiple parameters including the arrangement of steering angles, beamforming setup, sampling frequency, and motion estimation setup, among others. The number of diverging waves used for one compound image could be changed as long as the assumption of a constant velocity during the acquisition can be satisfied. In this study, the velocity was assumed to be constant within a 4-ms period (16 pulse transmissions with a PRF of 4 kHz) and the improved image quality with motion compensation was demonstrated *in vivo*. The motion estimation scheme proposed in this study has two stages, with the first stage giving the global starting point as the input of the second stage that comprises iterative window refinement. Fig. 5.9 shows the effect of the number of iterations in the second-stage motion estimation on the RMS velocity errors. The same parameters in Section 5.2.3 were used except that the number of iterations was varied. In this study, the number of iterations for the second-stage motion estimation was set to two, from which the curve in Fig. 5.9 starts to flatten.

A tilt angle step of 2° which is similar to 1.8° in (Joos *et al.*, 2018) was chosen for motion estimation in this study. However, the determination of this step is a compromise between the accuracy of motion estimation and the lateral resolution of

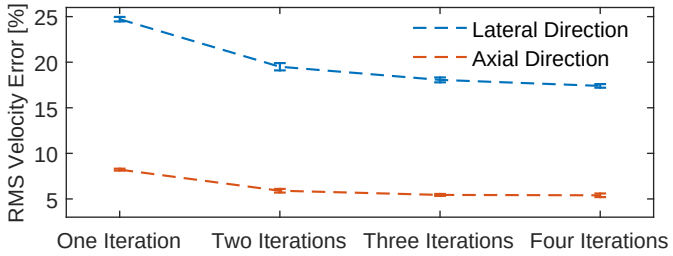

Figure 5.9: Relationship between the RMS velocity error and the number of iterations in the second-stage motion estimation. Results are from ten repeat simulations.

the compound image. For example, a small tilt angle step enables a high correlation between diverging waves, benefiting accurate motion estimation. A large tilt angle step provides a better lateral resolution after compounding due to a low correlation between diverging waves (Jespersen *et al.*, 1998). For the adopted imaging sequence in this study, the suitability of excluding the LRI pair with steering angles of $-4°$ and $4°$ for motion estimation was demonstrated by using the Field II simulated rotating disk. The relationship between the angular step θ ($2°$ or $8°$) and the accuracy of motion estimation was investigated using a single pair of LRIs from the steering angles of $-\theta/2$ and $\theta/2$. All other parameters were identical to those in Section 5.2.3. For the angular step of $2°$, the axial and lateral RMS velocity errors were $7.4\% \pm 0.1\%$ and $23.2\% \pm 0.4\%$, respectively. While for the angular step of $8°$, the corresponding errors increased to $9.9\% \pm 0.3\%$ and $27.9\% \pm 0.6\%$, respectively. All values here are based on ten repeat simulations.

The most accurate velocity estimation occurs along the direction of beam propagation (Saris *et al.*, 2016). For sector scanning using focused beams, the use of the beamformed images in the polar coordinate system rather than the scan-converted images in the Cartesian coordinate system is more effective for correlation-based motion estimation (Kim *et al.*, 2004). When using the Cartesian coordinate system, the estimation outliers mainly existed at locations with a large beam steering angle, where motion tracking did not follow the propagation direction of the incident ultrasonic beam (Kim *et al.*, 2004). Here the polar coordinate system was thus adopted for motion estimation and compensation.

This was explained with the simulated rotating disk phantom used for calculating the accuracy of the motion estimation method in Section 5.2.3. The associated B-mode

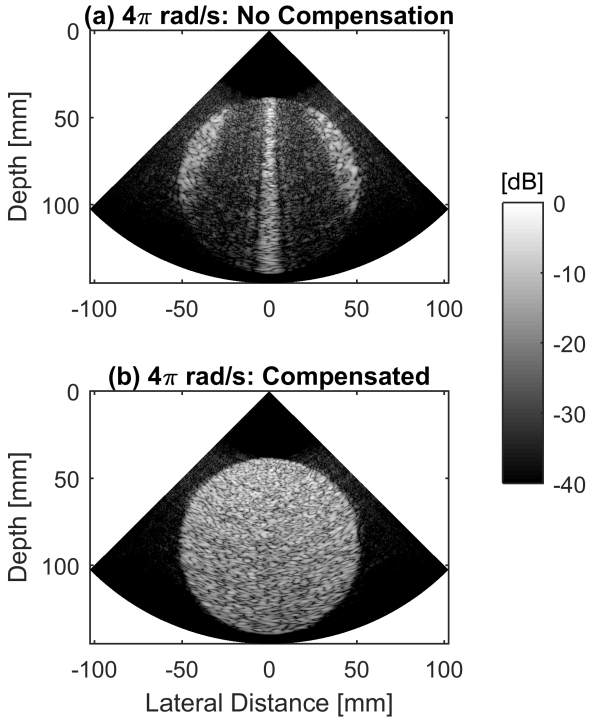

Figure 5.10: B-mode compound images of the simulated rotating disk (a) without and (b) with motion compensation in the polar coordinate system.

images with and without motion compensation are shown for demonstration. Fig. 5.10 shows the results when the polar coordinate system was used. Fig. 5.11 shows the results when motion estimation was performed in the Cartesian coordinate system. In Fig. 5.11, the interpretation of the disk is difficult due to the dark artefacts, where motion tracking does not follow the propagation direction of the diverging wave beam. The window sizes [(lateral distance, depth)] were varied between (3 mm x 2.95 mm), (6 mm x 5.9 mm), and (12 mm x 11.8 mm). For all used window sizes, the imaging artefacts were not avoided. For Fig. 5.11, the window size of (6 mm x 5.9 mm) was used.

Furthermore, the initial window size for motion estimation in the first stage should be big enough to accommodate the maximum flow velocity for specific cases, whilst keeping a good motion estimation resolution by minimizing the window size (Lenge *et al.*, 2014). The window size in this study was heuristically determined according to the 'one quarter rule' (Westerweel, 1997), where the inter-frame displacement should

be smaller than one quarter of the window size along both directions. With the combination of the maximum number of iterations in the second stage, the achievable local precision of motion compensation would be determined. The use of more iterations could improve the local accuracy for motion estimation and compensation but with higher computational cost.

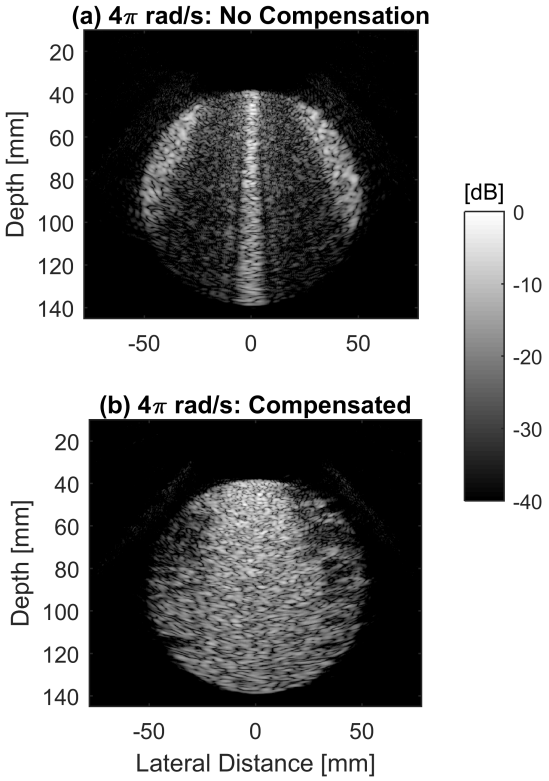

Figure 5.11: B-mode compound images of the simulated rotating disk (a) without and (b) with motion compensation in the Cartesian coordinate system.

5.4.2 Motion Artefacts within the AM Pulse Packet

At each steering angle, motion compensation was not applied between the subsequent LRIs from the full and half-amplitude transmissions in the AM scheme. This is because in multi-pulse contrast-enhancement schemes such as the adopted AM, higher velocities cause the artificial CTR enhancement because of incoherent subtraction, which could be beneficial for visual inspection (Lin *et al.*, 2013). However, for the quantitative use

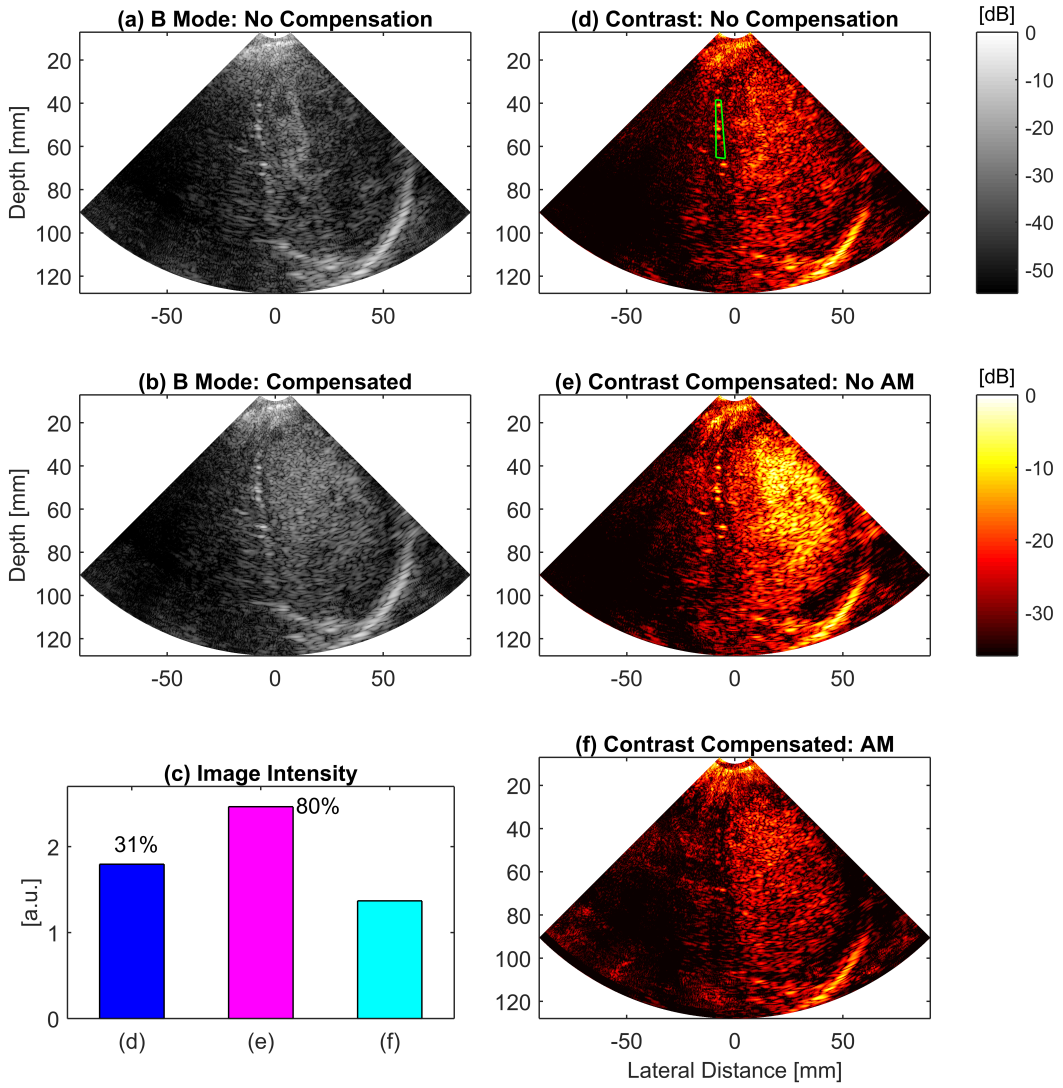

Figure 5.12: (a) and (b) show the B-mode compound images before and after motion compensation. Three contrast-mode images are shown in (d)−(f). (d) Without any motion compensation. (e) Only the motion artefacts between the AM LRIs were corrected. (f) When the motion artefacts within the AM pulse packet at each steering angle were also removed, apart from the motion compensation between the AM LRIs. For (d)−(f), intensity values for the myocardium ROI [marked in green on (d)] are shown in (c), where the percentage values marked show the differences in intensity of (d) and (e) relative to (f).

of microbubbles such as myocardial perfusion imaging, compensation of myocardial motion within the AM pulse packet at each steering angle could be necessary especially when the myocardium has a high speed as shown in Fig. 5.12. The effect of motion compensation is manifest for the myocardium, where the septum is poorly apparent in Fig. 5.12(a) when compared with Fig. 5.12(b). For the ROI of the myocardium, which is shown highlighted in green on Fig. 5.12(d), the image intensity in this region for each of Fig. 5.12(d)−(f) is shown in Fig. 5.12(c). The myocardial motion causes the decorrelation of tissue signals within the AM packet, leaving a residual signal but treated as the microbubble contrast signal. This is obvious in Fig. 5.12(e), where the myocardium becomes hyperechoic in the contrast-mode compound image when only motion artefacts between the AM LRIs were corrected. Fig. 5.12(f) shows the contrast-mode compound image when the motion within the AM packet at each steering angle was also compensated for. Also marked in Fig. 5.12(c), the intensity differences within the ROI are 31% and 80% for Fig. 5.12(d) and (e) when compared to the intensity in Fig. 5.12(f), where all motion artefacts were removed. The linear relationship is usually made between the contrast-mode image intensity and the microbubble concentration in quantitative myocardial perfusion studies (Tang *et al.*, 2011). The results suggest the necessity of removing the motion artefacts within the AM pulse packet for this application. This could also apply to other multi-pulse imaging schemes such as PI, where motion can interfere with the signal intensity (Lin *et al.*, 2013).

5.4.3 Future Development

The method was performed by using Matlab R2017a and executed on a CPU (Intel Xeon, E-5-1620, 3.6 GHz). The computation time of motion estimation and compensation for one compound image in the *in vitro* study was approximately 170 s, and it was approximately 130 s for the *in vivo* study. With the implementation of the applied approach on a GPU, the computational time could be significantly reduced. With addition of electrocardiography (ECG), accurately coupling the blood flow and the phase of the cardiac cycle would be possible. In this study, a lack of synchronized ECG was a limitation, which could be addressed with further development of the platform. Out-of-plane motion artefacts cannot be corrected with the current setup, which could be addressed by using a HFR 3-D scanning approach transmitting DWs (Roux *et al.*, 2018). Doppler-based strategies have been investigated for 3-D motion correction in

cardiac B-mode imaging using diverging waves (Chen *et al.*, 2018; Joos *et al.*, 2017a,b). It could be possible to translate our method to correct for motion in 3D, though to this end, many technical hurdles such as data handling, data transfer, and data storage need to be overcome.

Coupling myocardium and vortex dynamics has been suggested for early diagnosis of LV filling impairment (Faurie *et al.*, 2018), but this requires a high temporal resolution. With the same pulse sequence, HFR B-mode imaging, contrast-mode imaging and 2-D vector blood flow mapping have been obtained simultaneously at 250 Hz as demonstrated in Section 5.3.2. This provides a HFR triplex cardiac imaging tool using diverging waves, which could drastically improve our understanding of cardiac function by coupling myocardial motion, vortex dynamics in the LV and even microbubble-assisted myocardial perfusion.

5.5 Conclusion

This study described the implementation of a motion correction method for HFR CEE using coherent diverging wave imaging. Coherent summation of LRIs was corrupted without compensating for the motion between the angled diverging waves in both *in vitro* and *in vivo* studies. This method restored the image quality of a rotating disk *in vitro* with an increase of 12 dB in CR and 7 dB in CNR within the investigated cyst areas. The application of motion correction retrieved microbubble signals in the LV *in vivo*, enabling the better contrasted myocardium. With the same pulse sequence, a HFR cardiac imaging technique using diverging waves was demonstrated by combining B mode, contrast mode and 2-D vector blood flow mapping. Deciphering the interconnection between the simultaneous information (e.g., wall motion, vortex dynamics, and myocardial perfusion) obtained from these three imaging modes could be of clinical relevance for early diagnosis of cardiac dysfunction.

5. HFR CONTRAST-ENHANCED ECHOCARDIOGRAPHY USING DIVERGING WAVES: 2-D MOTION ESTIMATION & COMPENSATION

Chapter 6

Motion Compensation for HFR CEE Using Diverging Waves: Image Registration Versus Correlation-Based Method

6.1 Introduction

Clinical imaging systems are often constrained by cost and are not designed to be modified. These systems excite and store data from sub-groups of the aperture in order to reduce quantity of data. The research ultrasound platforms such as the UARP II are capable of exciting, sampling and storing data from each individual element of a phased array transducer, enabling an area known as HFR ultrasound imaging. By using unfocused diverging waves, a B-mode image can be reconstructed from a single transmission with parallel beamforming. For echocardiography, this approach can provide a frame rate up to 5 kHz, which is two orders of magnitude faster than the most clinical scanners. However, image degradation arising from the lack of transmit focusing when using diverging waves, could not be alleviated by coherent compounding due to the effect of cardiac motion. In Chapter 5, the motion effects on HFR CEE when combining diverging waves and microbubble contrast agents were demonstrated. A two-stage correlation-based method was introduced for motion-compensation, enabling coherent compounding. Despite the availability of different solutions for motion compensation,

little is known about their relative performance. The aim of this chapter was to compare any improvements in CR, CNR or CTR when using the correlation-based method (chapter 5) and an image registration-based method (Toulemonde *et al.*, 2017b) for motion compensation in HFR CEE using diverging waves.

6.1.1 Doppler-Based Techniques for Motion Compensation

Literature review of ultrasound Doppler techniques is given in Chapter 2. Numerous Doppler-based techniques (Faurie *et al.*, 2018; Joos *et al.*, 2018; Poree *et al.*, 2016) have been proposed to perform motion compensation for HFR echocardiography using diverging waves. In these strategies, myocardial motion is estimated with a triangle transmit sequence by using a modified autocorrelator. The shifts of the sidelobes due to the varied steering angles are then minimised. However, it would be difficult to implement these methods for HFR CEE. Since microbubbles can be selectively detected using nonlinear imaging schemes such as AM and PI at the cost of additional pulse transmissions, reducing the effective PRF and thus lowering the maximum detectable velocity without Doppler aliasing. With the motion compensation method in (Joos *et al.*, 2018; Poree *et al.*, 2016) and (Faurie *et al.*, 2018), the reliable Doppler estimation was reported to be as high as a half of the classical Nyquist Doppler velocity, *i.e.*, $cf_{\mathrm{PRF}}/(8f_0)$, where c indicates the speed of sound, f_{PRF} is the PRF, and f_0 is the centre frequency of the ultrasound pulse. Considering 1540 m/s, 4 kHz, and 2.78 MHz for c, f_{PRF}, and f_0 in Chapter 5, the reliable Doppler estimation for motion compensation can be made up to a threshold of 0.138 m/s with the halved PRF at 2 kHz by using AM. Doppler aliasing is likely in the LV, where blood flow can exceed this threshold as demonstrated in Fig. 5.8. In addition, the phase-based autocorrelation (Kasai *et al.*, 1985; Loupas *et al.*, 1995) in colour Doppler imaging could be biased in the presence of microbubbles due to their nonlinear vibrations (Ressner *et al.*, 2009), leading to incorrect motion compensation. In (Poree *et al.*, 2016) (Fig. 7), the Doppler-based motion compensation method with a linear tilt sequence caused a smeared background in a rotating disk experiment, but this artefact was not observed in Fig. 5.5. This could be explained by that our method uses 2-D pattern matching which is insensitive to the phase shift induced by sidelobes.

6.1.2 Image Registration Techniques for Motion Compensation

Image registration is prevalent in fusing different imaging modalities (e.g. MRI and ultrasound). It is a process of aligning images so that corresponding features can be easily related. In many applications, rigid image registration might be sufficient to correlate two medical images. While for cardiac imaging, tissue deformation needs to be accommodated, requiring nonrigid registration. Each nonrigid registration technique can be described with three components: a transformation matrix between the source and target images, the similarity index between these two images, and an optimisation function that optimises the similarity index and tunes the transformation matrix accordingly. In (Rueckert *et al.*, 1999), a combined transformation matrix T consisting of a global (T_{global}) and a local (T_{local}) transformation is formed

$$T(x, y, z) = T_{\text{global}}(x, y, z) + T_{\text{local}}(x, y, z). \tag{6.1}$$

For global motion, an affine transformation which can describe scaling and shearing is modelled. A free-form deformation based on B-splines is used to model nonrigid local motion by manipulating the underlying mesh of control points. Increasing resolution of the mesh control points can be achieved by refining the control point mesh, having decreased control point spacing at the current level. The nonrigid local deformation is optimised by a smooth transformation and the measurement of image similarity. To constrain the B-spline-based transformation to be smooth, a penalty term C_{smooth} is introduced. The measurement of image similarity $C_{\text{similarity}}$ can be performed based on the normalized mutual information which relies on the concept of information theory, or the squared sum of intensity differences. A cost function is written to find the optimal transformation as follows:

$$C = -C_{\text{similarity}}(I(t_0), T(I(t))) + \lambda_{\text{w}} C_{\text{smooth}}(T), \tag{6.2}$$

where $I(t_0)$ is the image intensity at t_0, and $I(t)$ is the image intensity at t. Here, the weighting parameter λ_{w} regulates the tradeoff between the image alignment and transformation smoothness. It is shown that the choice of this parameter is not crucial and a range between 0.001 and 0.1 is acceptable for ultrasound imaging applications (Harput *et al.*, 2018). The optimisation proceeds in two stages. In the first stage, the affine transformation parameters are optimised by using an iterative multiresolution method,

coping with the global motion. In the subsequent second stage, the parameters for nonrigid transformation are optimised in line with the cost function Eq. 6.2. The optimisation stops in practice when the change of the cost function is smaller than a predefined value.

6.2 Methods

6.2.1 Imaging Setup

The pulsing scheme for diverging wave imaging was adapted from (Nie *et al.*, 2019). The 4-cycle 2.78 MHz ultrasound pulses with either a full or half amplitude were transmitted, emanating diverging waves with the full aperture at each steering angle and enabling AM for contrast-enhanced imaging. The sector angle which was determinant to the imaging field of view was set to 90° and unchanged during beam steering for compounding. The arrangement of the steering angles was (−10°, −8°, −6°, −4°, 4°, 6°, 8°, 10°). The UARP II equipped with a phased array transducer P4-2v (Verasonics, Inc., WA, USA) was used for *in vitro* and *in vivo* measurements with a MI of 0.12 and a PRF of 4 kHz. The *in vitro* rotating disk phantom mentioned in Chapter 5 was used, and it was rotated at 4π rad/s.

6.2.2 Motion Estimation and Compensation

The proposed motion estimation algorithm (Nie *et al.*, 2019) used the correlation between angled diverging waves. A two-stage method was developed to find the correlation and subpixel displacement between angled LRIs in the polar coordinate system. The first stage used rigid block matching with correlation correction, achieved by multiplying all available correlation maps from the successive LRI pairs in the set for coherent summation. The second stage used an iterative scheme to improve the resolution and accuracy of the motion estimation by recursively decreasing the kernel size and deforming the kernel based on the results from the previous iteration. The number of iterations was set to two in this study, with different kernel sizes in each stage. The resultant motion estimation in each pixel was then obtained by linearly interpolating the motion estimation results from the last iteration of motion estimation. Based on these estimated displacements, motion compensation was then performed by aligning image pixels of all LRIs prior to coherent compounding. All LRIs with motion were

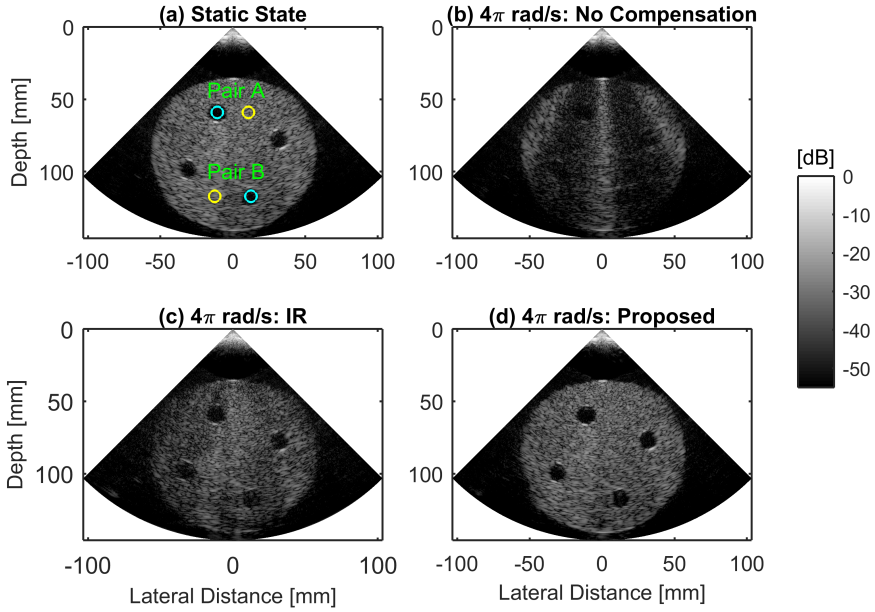

Figure 6.1: Compound images of the *in vitro* disk in the (a) static state, the rotating state (b) without motion compensation, and the rotating state compensated with (c) the image registration technique, and (d) the proposed correlation-based method. IR: image registration.

registered to the first LRI within the set that is used for coherent compounding. For the *in vitro* rotating disk experiments, two pairs of ROIs were delineated as shown in Fig. 6.1 (a) when the disk was placed static, with which the CRs and CNRs were calculated. All specific parameters were identical to Table 5.1 and 5.3.

For comparison, the image registration model (Rueckert *et al.*, 1999; Toulemonde *et al.*, 2017b) was applied to the LRIs in the polar grid before coherent summation of low-resolution B-mode and AM contrast-mode images. During image registration, the default parameters for 2-D images (`https://uk.mathworks.com/matlabcentral/fileexchange/20057-b-spline-grid-image-and-point-based-registration/`) were used. The first LRI within the set was used as the reference for registration.

6.3 Results

Using the image registration technique with motion correction, coherent compounding of diverging waves was partially improved, with the dark region reduced as shown in

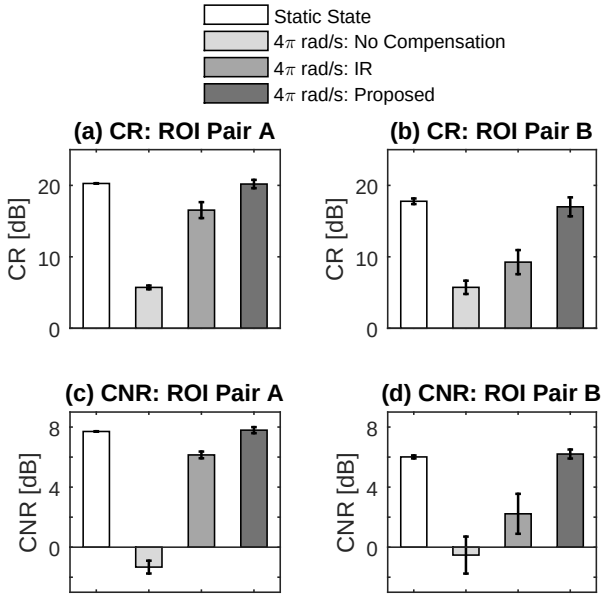

Figure 6.2: CRs and CNRs for two pairs of ROIs as shown in Fig. 6.1(a). The mean values and standard deviations are from four repeat measurements. IR: image registration.

Fig. 6.1 (c). With the correlation-based method, the artefacts from the original B-mode compound image (Fig. 6.1b) were removed without any smearing of the image as shown in Fig. 6.1(d). The CRs and CNRs were improved with the integration of both motion compensation strategies as shown in Fig. 6.2. Whereas in all cases, the improvement is more manifest when using the correlation-based method. This is particularly true for ROI pair B placed at a deeper location. The correlation-based method was found to improve the CR and CNR by 5 dB and 3 dB respectively (mean values for ROI pairs A and B) compared with the image registration model. The lower level of SNR for ROI pair B is expected, during image registration the operation of optimisation to minimise the cost function will take noise into account, deteriorating its performance for motion compensation.

Fig. 6.3(a) shows the ROIs for the calculation of CTR *in vivo*. Without motion compensation, dark imaging artefacts were found in Fig. 6.3(a) and Fig. 6.3(d). The use of the image registration model reduced the dark imaging artefacts (Fig. 6.3b and Fig. 6.3e). The correlation-based method further reduced the imaging artefacts as shown in Fig. 6.3(c), and a 6-dB improvement of CTR was demonstrated when

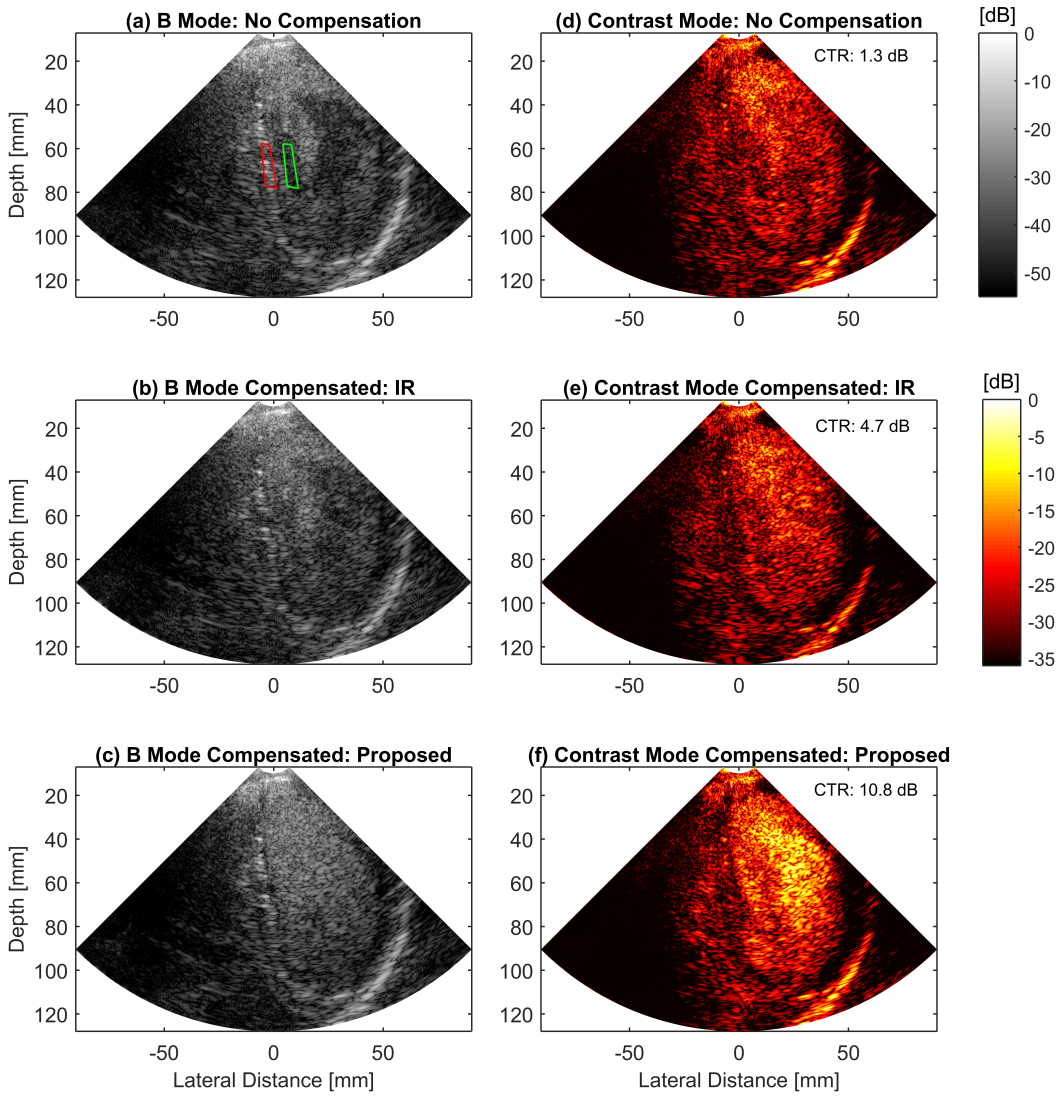

Figure 6.3: Synchronized B-mode and contrast-mode compound images from the same AM pulse sequence consisting of 16 pulse transmissions. Motion compensation was applied to (b), (c), (e) and(f). IR: image registration.

comparing Fig. 6.3(e) and Fig. 6.3(f).

6.4 Discussion

Transmitting the triangular transmit sequence as used in (Poree *et al.*, 2016) was further investigated by using Field II simulations. The number of steering angles is even in (Poree *et al.*, 2016). For comparison, two sequences were used. The steering angles for sequence one (linear transmit sequence) were: ($-7°$, $-5°$, $-3°$, $-1°$, $1°$, $3°$, $5°$, $7°$). For sequence two (triangular transmit sequence), they were ($-7°$, $-3°$, $1°$, $5°$, $7°$, $3°$, $-1°$, $-5°$). For sequence one, the method in Section 5.2.3 was used. For sequence two, motion estimation was performed between the first 4 angles, and then the later 4 angles. These two sets of motion estimation were then averaged to correct motion artefacts. The RMS velocity errors were 5.9% ± 0.1% and 19.9% ± 0.3% for the axial and lateral directions respectively for sequence one. For sequence two, they were 6.4% ± 0.1% and 22.4% ± 0.3%, respectively. These results are based on ten repeat simulations. No improvement was obtained when using the triangular transmit sequence, and the accuracy of motion estimation was even a little worse. The reason could be the larger angular step used for motion estimation with sequence two ($4°$ compared to $2°$ in sequence one). A larger steering angle results in a lower image correlation, negatively affecting the correlation-based motion estimation. Thus, the 'triangular transmit sequence' was not used.

For the correlation-based method, the velocity for each estimation point was assumed to be constant within a 4-ms period (16 pulse transmissions with a PRF of 4 kHz) and the improved image quality with motion compensation was demonstrated *in vivo*. The selection of the reference frame is thus not crucial in this method. One interesting application of changing the reference frame could be to artificially increase the frame rate. For example, in this study the same set of 8 LRIs for coherent compounding could be registered to every single LRI separately, providing up to 8 HRIs.

The motion estimation was performed with a static reference (the first LRI) when using the image registration technique. The selection of the reference frame is thus crucial and could disrupt motion correction if the reference frame has a low SNR. To further elaborate, image registration between each pair of consecutive frames was first

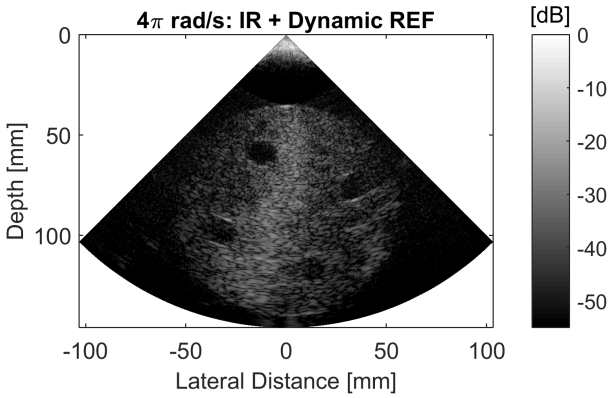

Figure 6.4: The RF data used for Fig. 6.1 was reprocessed using image registration-based motion correction with dynamic references. IR: image registration. REF: reference.

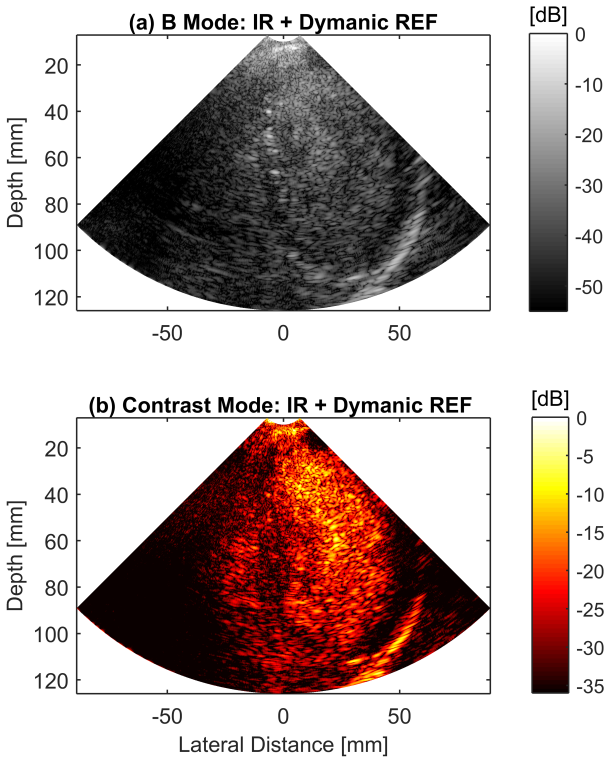

Figure 6.5: The RF data used for Fig. 6.3 was reprocessed using image registration-based motion correction with dynamic references. IR: image registration. REF: reference.

carried out, giving the motion field for each pair. Motion compensation was then performed by counter-shifting the LRIs based on the accumulated motion field calculated from each pair of consecutive frames. This arrangement may eliminate the problem of choosing a good reference frame with the image registration technique. Fig. 6.4 shows one typical compound image of the *in vitro* rotating disk phantom with the same RF data as used for Fig. 6.1. It is visible that the geometrical border of the disk is still largely affected by the dark imaging artefacts. In Fig. 6.5, the same RF data used for Fig. 6.3 was reprocessed with the scheme of using dynamic reference frames. Compared against Fig. 6.3(c), the dark imaging artefacts are noticeable especially within in the septum on the B-mode image in Fig. 6.5(a). The delineation of the endocardial border on the contrast-mode image as shown in Fig. 6.5(b) was degraded compared with Fig. 6.3(f). In Fig. 6.4 and Fig. 6.5, the images are presented with the first LRI as the registered state.

6.5 Conclusion

The efficacy of coherent diverging wave imaging is reliant on carefully designed motion compensation algorithms capable of correcting for incoherence between steered diverging-wave transmissions. Results first show that the proposed correlation-based method performed better in terms of CR and the visibility of geometrical borders of an *in vitro* rotating disk phantom. Compared against the image registration method, the improved CTR in AM contrast-enhanced imaging was also quantitatively demonstrated.

Chapter 7

Conclusion and Future Work

The state-of-the-art open ultrasound platforms offer precise amplitude and phase control on each channel, and access to the raw data. Leveraging the capabilities of the open platform to design novel transmit/receive sequencing and algorithms for manipulating and imaging microbubbles is the main motivation of this thesis. These developments have the potential for both diagnostic and therapeutic applications. In the following sections, the presented work is first summarized. It would not be possible to encase all aspects of the relevant techniques within this thesis, especially when considering the continuous emergence of new intriguing contributions in this field. Discussions of future research are then provided.

7.1 Summary and Conclusions

Switched mode excitation systems are cost-effective options for ultrasound generation especially for large count arrays. They are capable of amplitude and phase control of the excitation but suffering from signal distortion, due to the time delays when turning on and turning off the metal-oxide-semiconductor field-effect transistors (MOSFETs). The UARP II technologies feature quinary switching transmit circuits and harmonic reduction pulse width modulation (HRPWM), with low third harmonic output. The truly arbitrary waveform generation and sequencing control on each element of an array have underpinned the work in this thesis. In chapter 1, the specifications of the UARP II and other HFR ultrasound platforms were given.

In chapter 2, the fundamental techniques of ultrasound imaging were reviewed. These include B-mode imaging, ultrasound array transducers, ultrasound wave propagation, Doppler and vector flow imaging, nonlinear ultrasonics, contrast-enhanced ultrasound, and HFR ultrasound imaging using unfocused plane/diverging waves. When performing colour Doppler imaging, the desirability of using the 2-D autocorrelator for broadband Doppler signals was identified and supported by experimental measurements. This could provide hints for microbubble-enhanced Doppler imaging, where the echoes are largely broadband due to microbubbles' nonlinear response. The underlying theory of the multi-pulse microbubble imaging schemes was first explained by modelling the microbubble echo as a polynomial expansion of a basis waveform. By considering the effects of microbubble size and shell composition, the single-microbubble responses to those multi-pulse schemes were investigated with numerical experiments using the Marmottant model. The generation of the subharmonic component was also confirmed with this model when the applied acoustic pressure was high enough. The use of the single-microbubble simulation models neglects the secondary radiation force between microbubbles that originates from the microbubble re-scattered acoustic field. Enhanced models that can simulate a population of microbubbles could further improve the understanding of multi-pulse contrast-enhanced ultrasound imaging. Without nonlinear imaging schemes, the use of SVD for differentiating microbubbles from tissue was demonstrated with plane-wave frames. K-means clustering of singular values was then investigated as a way to automate the selection of singular vectors for enhanced microbubble imaging. To increase the prevalence of SVD in HFR contrast-enhanced ultrasound, the development of block-wise and accelerated SVD algorithms is desired.

The advantage of having precise control over the sequencing of an open platform was first demonstrated in chapter 3. The capability of aggregating and trapping microbubbles in flow holds promise for targeted drug delivery when using microbubbles as drug vehicles. As microbubbles could be locally accumulated, the payload concentration can be locally increased. This has potential for reducing the drug dose and side effects compared with a systematic delivery. In this chapter, the acoustic trap to arrest microbubbles against arterial flow rates was created by two opposing fields generated by plane-wave travelling waves from two subapertures of a single linear array transducer. Furthermore it was possible to monitor microbubble trapping using the same transducer by using the interleaved sequence for plane wave imaging. An advantage

of this delivery mechanism is that it does not rely on molecular targeting to control the drug dose - the acoustic trap does this. By adding high-intensity ultrasound pulses to the sequence, microbubbles could be destroyed to release the drug payload. Thus, the linear array could be capable of operating in all three modes: trapping, imaging and destruction. Rupturing large microbubble clusters is difficult, as surrounding microbubbles provide acoustic shielding. Microbubble clusters started to disperse after acoustic trapping ceased, but a high microbubble concentration was still maintained. Thus, a time delay could be set between the trapping and the destruction phase for an enhanced release by bursting more microbubbles.

Continuing on the use of ultrasound plane waves, subharmonic imaging of liposome-loaded microbubbles was then investigated in chapter 4. The subharmonic nonlinearity of microbubbles only occurs when the applied acoustic pressure is high enough to elicit the Faraday waves on the bubble surface. Buckling the microbubble shell through gas diffusion has been shown to decrease the pressure threshold to generate the subharmonic emission. By packing a layer of liposomes to the microbubble shell, the buckling state could also be facilitated to lower the pressure threshold for subharmonic imaging. As the exclusive response from microbubbles, the subharmonic signal is of interest for specially detecting the therapeutic liposome-loaded microbubbles. By distributing the total acoustic energy over multiple transmissions, coherent plane wave imaging is able to provide improved CTR compared to the line-by-line scanning mode without increasing the destruction rate of microbubbles. Subharmonic plane wave imaging of microbubbles was performed in this chapter, where it was found that, compared to unloaded microbubbles, it was easier to extract the subharmonic emission when using liposome-loaded microbubbles especially at deep locations. Numerically the use of liposome-loaded microbubbles was shown to improve the subharmonic amplitude by 127% compared with the unloaded microbubbles at the depth of 42 mm. In the future, more investigations are warranted to explore the relationship between the level of the enhanced subharmonic emission and the quantity of liposomes loaded on the microbubble.

In chapter 5, the combination of ultrasound diverging waves and microbubbles was considered. It was proposed, that coherent compounding is ineffective due to motion artefacts, and there may be necessity of developing motion compensation methods for HFR CEE. A correlation-based motion estimation scheme was proposed to compensate

for incoherence between angled transmissions. It was shown that for a 10-cm *in vitro* rotating disk phantom with a speed of 4π rad/s, the correlation-based motion compensation scheme improved the CR and CNR of the compound image by 12 dB and 7 dB respectively compared with their non-compensated counterpart. For the *in vivo* measurement, it was found that compensating for motion improved CTR, benefiting the delineation of the endocardial border. With the same pulse sequence, this chapter demonstrated simultaneous HFR B-mode imaging, contrast-enhanced imaging and vector flow mapping. This triplex imaging tool that is hitherto unrealised in hospitals, could impact the ability to quantify cardiac function by coupling myocardial motion, vortex dynamics in cardiac chambers and even microbubble-assisted myocardial perfusion.

The aim of chapter 6 was to compare any improvements in CR, CNR or CTR when using the correlation-based method (chapter 5) and an established image registration-based method for motion compensation in HFR CEE. For *in vitro* experiments with a rotating disk phantom, the proposed correlation-based method was shown to improve the CR and CNR by 5 dB and 3 dB, respectively. For the *in vivo* measurement, a 6-dB improvement in CTR was also demonstrated. Overall, the proposed correlation-based method outperformed the image registration algorithm in preserving the efficacy of coherent compounding for HFR CEE using diverging waves.

7.2 Future Research

HFR contrast-enhanced ultrasound using unfocused ultrasound waves is still mainly confined in academic research. A key technical challenge in the clinical roll-out of HFR ultrasound imaging is the volume of sampled data being received from the transducer needs real-time processing. A typical 128-element transducer produces 0.6 Mbytes of data per frame, at 5 KHz frame rate the continuous data rate is 3 Gbytes/s. Storage of several seconds of clinical data alone is challenging with the goal to produce real-time HFR imaging. These considerations indicate the requirement of a framework to amplify the theoretical value of HFR microbubble-enhanced ultrasound. Continuous ultrasound imaging with HFR feedback is only possible when using dedicated research platforms currently (Boni *et al.*, 2017, 2018). Real-time HFR Cardiac B-mode and

Doppler imaging was demonstrated (Ramalli *et al.*, 2018), followed by the demonstration of a GPU-enabled live ultrasound colour encoded speckle imaging platform (Yiu *et al.*, 2019). With the arrival of an era of big data, computational imaging techniques in the realm of machine/deep learning could make purposeful contributions to B-mode imaging (Gasse *et al.*, 2017) and motion estimation when using ultrasound (Dosovitskiy *et al.*, 2015). This could firstly facilitate real-time HFR imaging to enable clinical evaluation and secondly to aid functional evaluation of the organ with advanced algorithms by using the large amount of data afforded by HFR contrast-enhanced ultrasound.

The multiplane-wave (MV) compounding technique was proposed to improve the SNR of contrast-enhanced images at deep locations without increasing the MI (Gong *et al.*, 2018). Within one emission, the successive transmissions of multiple plane waves with different angles are first triggered, followed by decoding each single plane wave by properly combining the received data. However, the CTR obtained with this technique decreased significantly in the presence of motion artefacts (a CTR decrease of 7 dB for 5 cm/s). The decrease of CTR is attributed to the incoherence between steered transmissions, which suggests the necessity of developing proper motion compensation schemes for this technique in the future.

Scaling HFR ultrasound platforms for 3-D imaging is challenging. The increased channel count poses burdens on cost, data acquisition, transfer and processing. The employment of sparse (Harput *et al.*, 2018) and row-column arrays (Holbek *et al.*, 2016) is being intensively investigated, with demonstrations for 3-D super-resolution imaging and blood flow mapping. Compressive 3-D ultrasound imaging by using a single sensor was demonstrated recently (Kruizinga *et al.*, 2017). A plastic coding mask was placed in front of the ultrasound sensor, ensuring the identical compressed measurement in each voxel. This technique could provide an alternative to 3-D HFR contrast-enhanced ultrasound using 2-D matrix arrays.

Microbubbles are under active investigation for ultrasound-mediated targeted drug delivery. Coating microbubbles with magnetic nanoparticles has been used for imaging, targeting and improving the nonlinear acoustic response of microbubbles (Owen *et al.*, 2018). Gold nanoparticles have also been attached to the microbubble surface with the capability of dual modality photoacoustic and ultrasound imaging (Dove *et al.*, 2013). Manipulation of these microbubbles by using acoustic trapping as shown in chapter 3 could contribute to targeted photothermal therapy.

The architecture of the UARP II can be translated to the field of therapeutic ultrasound, where the capability of high-power transmit is required. The modified version of HRPWM (mHRPWM) (Cowell *et al.*, 2018) has been implemented in the High Intensity Focused Ultrasound Array Research Platform (HIFUARP) (Adams *et al.*, 2018), with which continuous control of the excitation amplitude and phase can be maintained even when using high-current MOSFETs. Thus, a combined ultrasound system for both therapeutic and diagnostic applications could be built using the same switched excitation circuits, reducing the cost and increasing the prevalence of image-guided HIFU for cancer treatment.

References

Adams, C., Carpenter, T.M., Cowell, D., Freear, S. & McLaughlan, J.R. (2018). Hifu drive system miniaturization using harmonic reduced pulsewidth modulation. *IEEE Transactions on Ultrasonics, Ferroelectrics, and Frequency Control*, **65**, 2407–2417. 122

Alomari, Z., Harput, S., Hyder, S. & Freear, S. (2014). Selecting the number and values of the cpwi steering angles and the effect of that on imaging quality. In *2014 IEEE International Ultrasonics Symposium*, 1191–1194. 88

Apfel, R.E. & Holland, C.K. (1991). Gauging the likelihood of cavitation from short-pulse, low-duty cycle diagnostic ultrasound. *Ultrasound in Medicine & Biology*, **17**, 179–185. 2, 58, 88

Arif, M. (2010). *Ultrasound harmonic imaging using chirp coded excitation*. Ph.D. thesis, University of Leeds. xix, 3

Asl, B.M. & Mahloojifar, A. (2009). Minimum variance beamforming combined with adaptive coherence weighting applied to medical ultrasound imaging. *IEEE Transactions on Ultrasonics, Ferroelectrics, and Frequency Control*, **56**, 1923–1931. 39

Averkiou, M.A. (2001). Tissue harmonic ultrasonic imaging. *Comptes Rendus de l'Acadmie des Sciences - Series IV - Physics*, **2**, 1139 – 1151. 28

Barnsley, L.C., Carugo, D. & Stride, E. (2016). Optimized shapes of magnetic arrays for drug targeting applications. *Journal of Physics D: Applied Physics*, **49**, 225501. 47

Battaglia, V. & Cervelli, R. (2017). Liver investigations: Updating on us technique and contrast-enhanced ultrasound (ceus). *European Journal of Radiology*, **96**, 65–73. 46

Beeri, E., Maier, S.E., Landzberg, M.J., Chung, T. & Geva, T. (1998). In vivo evaluation of fontan pathway flow dynamics by multidimensional phase-velocity magnetic resonance imaging. *Circulation*, **98**, 2873–2882. 91

BMUS (2010). Guidelines for the safe use of diagnostic ultrasound equipment. *Ultrasound*, **18**, 52–59. 15

Bohs, L., Geiman, B., Anderson, M., Gebhart, S. & Trahey, G. (2000). Speckle tracking for multi-dimensional flow estimation. *Ultrasonics*, **38**, 369–375. 24

Boni, E., Bassi, L., Dallai, A., Guidi, F., Meacci, V., Ramalli, A., Ricci, S. & Tortoli, P. (2016). Ula-op 256: A 256-channel open scanner for development and real-time implementation of new ultrasound methods. *IEEE Transactions on Ultrasonics, Ferroelectrics, and Frequency Control*, **63**, 1488–1495. xi, 5

Boni, E., Bassi, L., Dallai, A., Meacci, V., Ramalli, A., Scaringella, M., Guidi, F., Ricci, S. & Tortoli, P. (2017). Architecture of an ultrasound system for continuous real-time high frame rate imaging. *IEEE Transactions on Ultrasonics, Ferroelectrics, and Frequency Control*, **64**, 1276–1284. 36, 120

Boni, E., Yu, A.C.H., Freear, S., Jensen, J.A. & Tortoli, P. (2018). Ultrasound open platforms for next-generation imaging technique development. *IEEE Transactions on Ultrasonics, Ferroelectrics, and Frequency Control*, **65**, 1078–1092. 4, 36, 75, 83, 120

Bouakaz, A., Krenning, B.J., Vletter, W.B., Ten Cate, F.J. & De Jong, N. (2003). Contrast superharmonic imaging: A feasibility study. *Ultrasound in Medicine & Biology*, **29**, 547–553. 2, 46

Browne, J., Ramnarine, K., Watson, A. & Hoskins, P. (2003). Assessment of the acoustic properties of common tissue-mimicking test phantoms. *Ultrasound in Medicine & Biology*, **29**, 1053–1060. 55, 92

Chatterjee, D. & Sarkar, K. (2003). A newtonian rheological model for the interface of microbubble contrast agents. *Ultrasound in Medicine & Biology*, **29**, 1749–1757. 32

Chen, Y., Dhooge, J. & Luo, J. (2018). Doppler-based motion compensation strategies for 3d diverging wave compounding and multi-plane-transmit beamforming: A simulation study. *IEEE Transactions on Ultrasonics, Ferroelectrics, and Frequency Control*, 1–1. 92, 105

Chen, Y.H., Lin, Y.M., Ho, K.Y., Wu, A.Y. & Li, P.C. (2014). Low-complexity motion-compensated beamforming algorithm and architecture for synthetic transmit aperture in ultrasound imaging. *IEEE Transactions on Signal Processing*, **62**, 840–851. 83

Cheung, C.C.P., Yu, A.C.H., Salimi, N., Yiu, B.Y.S., Tsang, I.K.H., Kerby, B., Azar, R.Z. & Dickie, K. (2012). Multi-channel pre-beamformed data acquisition system for research on advanced ultrasound imaging methods. *IEEE Transactions on Ultrasonics, Ferroelectrics, and Frequency Control*, **59**, 243–253. xi, 5

Church, C.C. (2005). Frequency, pulse length, and the mechanical index. *Acoustics Research Letters Online*, **6**, 162–168. 2, 58, 88

Cikes, M., Tong, L., Sutherland, G.R. & Dhooge, J. (2014). Ultrafast cardiac ultrasound imaging: technical principles, applications, and clinical benefits. *JACC: Cardiovascular Imaging*, **7**, 812–823. 82, 83

Cimino, S., Pedrizzetti, G., Tonti, G., Canali, E., Petronilli, V., De Luca, L., Iacoboni, C. & Agati, L. (2012). In vivo analysis of intraventricular fluid dynamics in healthy hearts. *European Journal of Mechanics-B/Fluids*, **35**, 40–46. 82

Couture, O., Bannouf, S., Montaldo, G., Aubry, J.F., Fink, M. & Tanter, M. (2009). Ultrafast imaging of ultrasound contrast agents. *Ultrasound in Medicine & Biology*, **35**, 1908–1916. 4, 39

Couture, O., Fink, M. & Tanter, M. (2012). Ultrasound contrast plane wave imaging. *IEEE Transactions on Ultrasonics, Ferroelectrics, and Frequency Control*, **59**. 39, 46, 50, 72

Cowell, D. & Freear, S. (2008). Quinary excitation method for pulse compression ultrasound measurements. *Ultrasonics*, **48**, 98–108. 4, 58, 88

Cowell, D.M.J., Smith, P.R. & Freear, S. (2013). Phase-inversion-based selective harmonic elimination (pi-she) in multi-level switched-mode tone- and frequency-modulated excitation. *IEEE Transactions on Ultrasonics, Ferroelectrics, and Frequency Control*, **60**, 1084–1097. 4

Cowell, D.M.J., Carpenter, T.M., Adams, C. & Freear, S. (2018). Modified harmonic reduction pulse width modulation (mhrpwm) for switched excitation of resonant hifu transducers. In *2018 IEEE International Ultrasonics Symposium (IUS)*, 1–4. 122

Crake, C., de Saint Victor, M., Owen, J., Coviello, C., Collin, J., Coussios, C.C. & Stride, E. (2015). Passive acoustic mapping of magnetic microbubbles for cavitation enhancement and localization. *Physics in Medicine & Biology*, **60**, 785. 47, 66

Crake, C., Owen, J., Smart, S., Coviello, C., Coussios, C.C., Carlisle, R. & Stride, E. (2016). Enhancement and passive acoustic mapping of cavitation from fluorescently tagged magnetic resonance-visible magnetic microbubbles in vivo. *Ultrasound in Medicine & Biology*, **42**, 3022–3036. 47

Daeichin, V., Akkus, Z., Skachkov, I., Kooiman, K., Needles, A., Sluimer, J., Janssen, B., Daemen, M.J.A.P., van der Steen, A.F.W., de Jong, N. & Bosch, J.G. (2015). Quantification of bound microbubbles in ultrasound molecular imaging. *IEEE Transactions on Ultrasonics, Ferroelectrics, and Frequency Control*, **62**, 1190–1200. 11

Dave, J.K., Kulkarni, S.V., Pangaonkar, P.P., Stanczak, M., McDonald, M.E., Cohen, I.S., Mehrotra, P., Savage, M.P., Walinsky, P., Ruggiero II, N.J. *et al.* (2017). Non-invasive intra-cardiac pressure measurements using subharmonic-aided pressure estimation: Proof of concept in humans. *Ultrasound in Medicine & Biology*, **43**, 2718–2724. 72

Dayton, P., Klibanov, A., Brandenburger, G. & Ferrara, K. (1999). Acoustic radiation force in vivo: a mechanism to assist targeting of microbubbles. *Ultrasound in Medicine & Biology*, **25**, 1195–1201. 4, 47, 54

Dayton, P.A., Morgan, K.E., Klibanov, A.L., Brandenburger, G., Nightingale, K.R. & Ferrara, K.W. (1997). A preliminary evaluation of the effects of primary and secondary radiation forces on acoustic contrast agents. *IEEE Transactions on Ultrasonics, Ferroelectrics, and Frequency Control*, **44**, 1264–1277. 50, 51, 52, 53, 54

De Jong, N., Emmer, M., Chin, C.T., Bouakaz, A., Mastik, F., Lohse, D. & Versluis, M. (2007). compression-only behavior of phospholipid-coated contrast bubbles. *Ultrasound in Medicine & Biology*, **33**, 653–656. 72

de Saint Victor, M., Crake, C., Coussios, C.C. & Stride, E. (2014). Properties, characteristics and applications of microbubbles for sonothrombolysis. *Expert Opinion on Drug Delivery*, **11**, 187–209. 46

Demené, C., Deffieux, T., Pernot, M., Osmanski, B.F., Biran, V., Gennisson, J.L., Sieu, L.A., Bergel, A., Franqui, S., Correas, J.M. *et al.* (2015). Spatiotemporal clutter filtering of ultrafast ultrasound data highly increases doppler and fultrasound sensitivity. *IEEE Transactions on Medical Imaging*, **34**, 2271–2285. 40, 62

Denarie, B., Tangen, T.A., Ekroll, I.K., Rolim, N., Torp, H., Bjstad, T. & Lovstakken, L. (2013). Coherent plane wave compounding for very high frame rate ultrasonography of rapidly moving targets. *IEEE Transactions on Medical Imaging*, **32**, 1265–1276. 83

Desailly, Y., Tissier, A.M., Correas, J.M., Wintzenrieth, F., Tanter, M. & Couture, O. (2016). Contrast enhanced ultrasound by real-time spatiotemporal filtering of ultrafast images. *Physics in Medicine & Biology*, **62**, 31. 40

Dosovitskiy, A., Fischer, P., Ilg, E., Hausser, P., Hazirbas, C., Golkov, V., Van Der Smagt, P., Cremers, D. & Brox, T. (2015). Flownet: Learning optical flow with convolutional networks. In *Proceedings of The IEEE International Conference on Computer Vision*, 2758–2766. 121

Dove, J.D., Murray, T.W. & Borden, M.A. (2013). Enhanced photoacoustic response with plasmonic nanoparticle-templated microbubbles. *Soft Matter*, **9**, 7743–7750. 121

Dunmire, B., Beach, K., Labs, K., Plett, M. & Strandness, D. (2000). Cross-beam vector doppler ultrasound for angle-independent velocity measurements. *Ultrasound in Medicine & Biology*, **26**, 1213–1235. 24

Eckersley, R.J., Chin, C.T. & Burns, P.N. (2005). Optimising phase and amplitude modulation schemes for imaging microbubble contrast agents at low acoustic power. *Ultrasound in Medicine & Biology*, **31**, 213–219. 2, 28, 29, 33, 35, 68, 79, 82, 87

Eisenbrey, J.R., Sridharan, A., Machado, P., Zhao, H., Halldorsdottir, V.G., Dave, J.K., Liu, J.B., Park, S., Dianis, S., Wallace, K. *et al.* (2012). Three-dimensional subharmonic ultrasound imaging in vitro and in vivo. *Academic Radiology*, **19**, 732–739. 72

Ekroll, I.K., Voormolen, M.M., Standal, O.K.., Rau, J.M. & Lovstakken, L. (2015). Coherent compounding in doppler imaging. *IEEE Transactions on Ultrasonics, Ferroelectrics, and Frequency Control*, **62**, 1634–1643. 83

Errico, C., Pierre, J., Pezet, S., Desailly, Y., Lenkei, Z., Couture, O. & Tanter, M. (2015). Ultrafast ultrasound localization microscopy for deep super-resolution vascular imaging. *Nature*, **527**, 499–502. 4, 11, 36, 39, 46

Escoffre, J., Mannaris, C., Geers, B., Novell, A., Lentacker, I., Averkiou, M. & Bouakaz, A. (2013). Doxorubicin liposome-loaded microbubbles for contrast imaging and ultrasound-triggered drug delivery. *IEEE Transactions on Ultrasonics, Ferroelectrics, and Frequency Control*, **60**, 78–87. 3, 46, 71

Fadnes, S., Wigen, M.S., Nyrnes, S.A. & Lovstakken, L. (2017). In vivo intracardiac vector flow imaging using phased array transducers for pediatric cardiology. *IEEE Transactions on Ultrasonics, Ferroelectrics, and Frequency Control*, **64**, 1318–1326. 37, 83, 91

Faez, T., Emmer, M., Kooiman, K., Versluis, M., van der Steen, A.F.W. & de Jong, N. (2013). 20 years of ultrasound contrast agent modeling. *IEEE Transactions on Ultrasonics, Ferroelectrics, and Frequency Control*, **60**. 46

Faurie, J., Baudet, M., Pore, J., Cloutier, G., Tournoux, F. & Garcia, D. (2018). Coupling myocardium and vortex dynamics in diverging-wave echocardiography. *IEEE Transactions on Ultrasonics, Ferroelectrics, and Frequency Control*, 1–1. 105, 108

Feigenbaum, H., Stone, J.M., Lee, D.A., Nasser, W.K. & Chang, S. (1970). Identification of ultrasound echoes from the left ventricle by use of intracardiac injections of indocyanine green. *Circulation*, **41**, 615–621. 2

Ferrara, K., Pollard, R. & Borden, M. (2007). Ultrasound microbubble contrast agents: fundamentals and application to gene and drug delivery. *Annu. Rev. Biomed. Eng.*, **9**, 415–447. 47

Food, Administration, D. *et al.* (1985). 510 (k) guide for measuring and reporting acoustic output of diagnostic medical devices. *Rockville, MD*. 15

Forsberg, F., Shi, W.T. & Goldberg, B. (2000). Subharmonic imaging of contrast agents. *Ultrasonics*, **38**, 93–98. 46

Forsberg, F., Liu, J.B., Shi, W.T., Ro, R., Lipcan, K.J., Deng, X. & Hall, A.L. (2006). In vivo perfusion estimation using subharmonic contrast microbubble signals. *Journal of Ultrasound in Medicine*, **25**, 15–21. 72

Frinking, P.J., Bouakaz, A., Kirkhorn, J., Ten Cate, F.J. & De Jong, N. (2000). Ultrasound contrast imaging: current and new potential methods. *Ultrasound in Medicine & Biology*, **26**, 965–975. 29

Gammelmark, K.L. & Jensen, J.A. (2014). 2-d tissue motion compensation of synthetic transmit aperture images. *IEEE Transactions on Ultrasonics, Ferroelectrics, and Frequency Control*, **61**, 594–610. 83, 89

Garcia, D. (2010). Robust smoothing of gridded data in one and higher dimensions with missing values. *Computational Statistics & Data Analysis*, **54**, 1167–1178. 87

Gasse, M., Millioz, F., Roux, E., Garcia, D., Liebgott, H. & Friboulet, D. (2017). High-quality plane wave compounding using convolutional neural networks. *IEEE Transactions on Ultrasonics, Ferroelectrics, and Frequency Control*, **64**, 1637–1639. 39, 121

Gessner, R. & Dayton, P.A. (2010). Advances in molecular imaging with ultrasound. *Molecular Imaging*, **9**, 7290–2010. 72

Gessner, R., Lukacs, M., Lee, M., Cherin, E., Foster, F.S. & Dayton, P.A. (2010). High-resolution, high-contrast ultrasound imaging using a prototype dual-frequency transducer: In vitro and in vivo studies. *IEEE Transactions on Ultrasonics, Ferroelectrics, and Frequency Control*, **57**, 1772–1781. 35

Gessner, R.C., Streeter, J.E., Kothadia, R., Feingold, S. & Dayton, P.A. (2012). An in vivo validation of the application of acoustic radiation force to enhance the diagnostic utility of molecular imaging using 3-d ultrasound. *Ultrasound in Medicine & Biology*, **38**, 651–660. 47

Gill, R.W. (1985). Measurement of blood flow by ultrasound: accuracy and sources of error. *Ultrasound in Medicine & Biology*, **11**, 625–641. 24

Gong, P., Song, P. & Chen, S. (2018). Improved contrast-enhanced ultrasound imaging with multiplane-wave imaging. *IEEE Transactions on Ultrasonics, Ferroelectrics, and Frequency Control*, **65**, 178–187. 79, 121

Gorce, J.M., Arditi, M. & Schneider, M. (2000). Influence of bubble size distribution on the echogenicity of ultrasound contrast agents: A study of sonovue. *Investigative Radiology*, **35**, 661–671. 54

Gramiak, R. & Shah, P.M. (1968). Echocardiography of the aortic root. *Investigative Radiology*, **3**, 356–366. 2

Greis, C. (2004). Technology overview: Sonovue (bracco, milan). *European Radiology*, **14**, P11–5. 2

Grondin, J., Sayseng, V. & Konofagou, E.E. (2017). Cardiac strain imaging with coherent compounding of diverging waves. *IEEE Transactions on Ultrasonics, Ferroelectrics, and Frequency Control*, **64**, 1212–1222. 11, 37, 83

Harput, S., Arif, M., Mclaughlan, J., Cowell, D.M.J. & Freear, S. (2013). The effect of amplitude modulation on subharmonic imaging with chirp excitation. *IEEE Transactions on Ultrasonics, Ferroelectrics, and Frequency Control*, **60**, 2532–2544. 2, 21, 54, 68, 77

Harput, S., Nie, L., Cowell, D.M.J., Carpenter, T., Raiton, B., McLaughlan, J. & Freear, S. (2016). Simultaneous trapping and imaging of microbubbles at clinically relevant flow rates. In *2016 IEEE International Ultrasonics Symposium (IUS)*, 1–4. i, 50, 58

Harput, S., Christensen-Jeffries, K., Brown, J., Li, Y., Williams, K.J., Davies, A.H., Eckersley, R.J., Dunsby, C. & Tang, M.X. (2018). Two-stage motion correction for super-resolution ultrasound imaging in human lower limb. *IEEE Transactions on Ultrasonics, Ferroelectrics, and Frequency Control*, **65**, 803–814. 84, 109

Harput, S., Christensen-Jeffries, K., Brown, J., Zhu, J., Zhang, G., Leow, C.H., Toulemonde, M., Ramalli, A., Boni, E., Tortoli, P., Eckersley, R.J., Dunsby, C. & Tang, M. (2018). 3-d super-resolution ultrasound imaging using a 2-d sparse array with high volumetric imaging rate. In *2018 IEEE International Ultrasonics Symposium (IUS)*, 1–9. 39, 121

Hasegawa, H. & Kanai, H. (2011). High-frame-rate echocardiography using diverging transmit beams and parallel receive beamforming. *Journal of Medical Ultrasonics*, **38**, 129–140. 37, 83

Hasson, A.M. *et al.* (2016). Characterizations of the mathematical models of ultrasound contrast agents: a review. *Collage of Education*, **1**. 32

Heiles, B., Correia, M., Pernot, M., Provost, J., Tanter, M. & Couture, O. (2017). Volumetric ultrafast ultrasound localization microscopy using a 3232 matrix array. In *2017 IEEE International Ultrasonics Symposium (IUS)*, 1–1. 39

Hohmann, J., Albrecht, T., Hoffmann, C. & Wolf, K.J. (2003). Ultrasonographic detection of focal liver lesions: increased sensitivity and specificity with microbubble contrast agents. *European Journal of Radiology*, **46**, 147–159. 2

Holbek, S., Christiansen, T.L., Stuart, M.B., Beers, C., Thomsen, E.V. & Jensen, J.A. (2016). 3-d vector flow estimation with rowcolumn-addressed arrays. *IEEE Transactions on Ultrasonics, Ferroelectrics, and Frequency Control*, **63**, 1799–1814. 121

Hoskins, P.R., Martin, K. & Thrush, A. (2010). *Diagnostic ultrasound: physics and equipment*. Cambridge University Press. 13, 16

Hoyos, C.A.V., Stuart, M.B., Hansen, K.L., Nielsen, M.B. & Jensen, J.A. (2016). Accurate angle estimator for high-frame-rate 2-d vector flow imaging. *IEEE Transactions on Ultrasonics, Ferroelectrics, and Frequency Control*, **63**, 842–853. 36

Hudson, J.M., Williams, R., Tremblay-Darveau, C., Sheeran, P.S., Milot, L., Bjarnason, G.A. & Burns, P.N. (2015). Dynamic contrast enhanced ultrasound for therapy monitoring. *European Journal of Radiology*, **84**, 1650–1657. 72

Hyun, D., Abou-Elkacem, L., Perez, V.A., Chowdhury, S.M., Willmann, J.K. & Dahl, J.J. (2018). Improved sensitivity in ultrasound molecular imaging with coherence-based beamforming. *IEEE Transactions on Medical Imaging*, **37**, 241–250. 39

Jensen, J.A. & Munk, P. (1998). A new method for estimation of velocity vectors. *IEEE Transactions on Ultrasonics, Ferroelectrics, and Frequency Control*, **45**, 837–851. 24

Jensen, J.A. & Svendsen, N.B. (1992). Calculation of pressure fields from arbitrarily shaped, apodized, and excited ultrasound transducers. *IEEE Transactions on Ultrasonics, Ferroelectrics, and Frequency Control*, **39**, 262–267. 48, 89

Jensen, J.A., Holten-Lund, M.F., Nilsson, R.T., Hansen, M., Larsen, U.D., Domsten, R.P., Tomov, B.G., Stuart, M.B., Nikolov, S.I., Pihl, M.J., Du, Y., Rasmussen, J.H. & Rasmussen, M.F. (2013). Sarus: A synthetic aperture real-time ultrasound system. *IEEE Transactions on Ultrasonics, Ferroelectrics, and Frequency Control*, **60**, 1838–1852. xi, 5

Jeong, S.K. & Rosenson, R.S. (2013). Shear rate specific blood viscosity and shear stress of carotid artery duplex ultrasonography in patients with lacunar infarction. *BMC Neurology*, **13**, 36. 55

Jespersen, S.K., Wilhjelm, J.E. & Sillesen, H. (1998). Multi-angle compound imaging. *Ultrasonic Imaging*, **20**, 81–102. 91, 100

Joos, P., Liebgott, H., Varray, F., Petrusca, L., Garcia, D., Vray, D. & Nicolas, B. (2017a). High-frame-rate 3-d echocardiography based on motion compensation: An in vitro evaluation. In *2017 IEEE International Ultrasonics Symposium (IUS)*, 1–4. 105

Joos, P., Liebgott, H., Varray, F., Petrusca, L., Garcia, D., Vray, D. & Nicolas, B. (2017b). High-volume-rate 3-d ultrasound imaging based on motion compensation: A feasibility study. In *2017 IEEE International Ultrasonics Symposium (IUS)*, 1–1. 105

Joos, P., Pore, J., Liebgott, H., Vray, D., Baudet, M., Faurie, J., Tournoux, F., Cloutier, G., Nicolas, B. & Garcia, D. (2018). High-frame-rate speckle-tracking echocardiography. *IEEE Transactions on Ultrasonics, Ferroelectrics, and Frequency Control*, **65**, 720–728. 83, 87, 88, 99, 108

Kaneko, O.F. & Willmann, J.K. (2012). Ultrasound for molecular imaging and therapy in cancer. *Quantitative Imaging in Medicine and Surgery*, **2**, 87. 11

Kasai, C., Namekawa, K., Koyano, A. & Omoto, R. (1985). Real-time two-dimensional blood flow imaging using an autocorrelation technique. *IEEE Transactions on Sonics and Ultrasonics*, **32**, 458–464. 20, 108

Kaul, S. (1998). Quantification of myocardial blood flow using ultrasound-induced destruction of microbubbles administered as a constant venous infusion. *The Journal of the Acoustical Society of America*, **103**, 3001–3001. 28

Kim, H., Hertzberg, J. & Shandas, R. (2004). Development and validation of echo piv. *Experiments in Fluids*, **36**, 455–462. 24, 25, 100

Kim, K., Hwang, J., Jeong, J. & Song, T. (2002). An efficient motion estimation and compensation method for ultrasound synthetic aperture imaging. *Ultrasonic Imaging*, **24**, 81–99. 83

Klibanov, A.L. (2009). Preparation of targeted microbubbles: ultrasound contrast agents for molecular imaging. *Medical & Biological Engineering & Computing*, **47**, 875–882. 3

Kooiman, K., Vos, H.J., Versluis, M. & de Jong, N. (2014). Acoustic behavior of microbubbles and implications for drug delivery. *Advanced Drug Delivery Reviews*, **72**, 28–48. 46, 66

Kruizinga, P., van der Meulen, P., Fedjajevs, A., Mastik, F., Springeling, G., de Jong, N., Bosch, J.G. & Leus, G. (2017). Compressive 3d ultrasound imaging using a single sensor. *Science Advances*, **3**, e1701423. 121

Leighton, T., Walton, A. & Pickworth, M. (1990). Primary bjerknes forces. *European Journal of Physics*, **11**, 47. 51, 52

Leighton, T., Phelps, A., Ramble, D. & Sharpe, D. (1996). Comparison of the abilities of eight acoustic techniques to detect and size a single bubble. *Ultrasonics*, **34**, 661–667. 35

Leighton, T.G. (2007). What is ultrasound? *Progress in Biophysics and Molecular Biology*, **93**, 3–83. 26, 46

Lenge, M., Ramalli, A., Boni, E., Liebgott, H., Cachard, C. & Tortoli, P. (2014). High-frame-rate 2-d vector blood flow imaging in the frequency domain. *IEEE Transactions on Ultrasonics, Ferroelectrics, and Frequency Control*, **61**, 1504–1514. 60, 101

Lenge, M., Ramalli, A., Tortoli, P., Cachard, C. & Liebgott, H. (2015). Plane-wave transverse oscillation for high-frame-rate 2-d vector flow imaging. *IEEE Transactions on Ultrasonics, Ferroelectrics, and Frequency Control*, **62**, 2126–2137. 36

Lentacker, I., De Smedt, S.C. & Sanders, N.N. (2009). Drug loaded microbubble design for ultrasound triggered delivery. *Soft Matter*, **5**, 2161–2170. 46

Leow, C.H., Bazigou, E., Eckersley, R.J., Alfred, C., Weinberg, P.D. & Tang, M.X. (2015). Flow velocity mapping using contrast enhanced high-frame-rate

plane wave ultrasound and image tracking: Methods and initial in vitro and in vivo evaluation. *Ultrasound in Medicine & Biology*, **41**, 2913–2925. 4, 36, 39, 55, 85

Li, Y.L. & Dahl, J.J. (2015). Coherent flow power doppler (cfpd): flow detection using spatial coherence beamforming. *IEEE Transactions on Ultrasonics, Ferroelectrics, and Frequency Control*, **62**, 1022–1035. 39

Lin, F., Cachard, C., Mori, R., Varray, F., Guidi, F. & Basset, O. (2013). Ultrasound contrast imaging: influence of scatterer motion in multi-pulse techniques. *IEEE Transactions on Ultrasonics, Ferroelectrics, and Frequency Control*, **60**, 2065–2078. 102, 104

Lin, F., Shelton, S.E., Espíndola, D., Rojas, J.D., Pinton, G. & Dayton, P.A. (2017). 3-d ultrasound localization microscopy for identifying microvascular morphology features of tumor angiogenesis at a resolution beyond the diffraction limit of conventional ultrasound. *Theranostics*, **7**, 196. 39

Liu, Y., Miyoshi, H. & Nakamura, M. (2006). Encapsulated ultrasound microbubbles: therapeutic application in drug/gene delivery. *Journal of Controlled Release*, **114**, 89–99. 47

Loupas, T., Powers, J.T. & Gill, R.W. (1995). An axial velocity estimator for ultrasound blood flow imaging, based on a full evaluation of the doppler equation by means of a two-dimensional autocorrelation approach. *IEEE Transactions on Ultrasonics, Ferroelectrics, and Frequency Control*, **42**, 672–688. 20, 108

Luan, Y., Faez, T., Gelderblom, E., Skachkov, I., Geers, B., Lentacker, I., van der Steen, T., Versluis, M. & de Jong, N. (2012). Acoustical properties of individual liposome-loaded microbubbles. *Ultrasound in Medicine & Biology*, **38**, 2174–2185. 72

Macé, E., Montaldo, G., Cohen, I., Baulac, M., Fink, M. & Tanter, M. (2011). Functional ultrasound imaging of the brain. *Nature Methods*, **8**, 662. 4

Marmottant, P., van der Meer, S., Emmer, M., Versluis, M., de Jong, N., Hilgenfeldt, S. & Lohse, D. (2005). A model for large amplitude oscillations of coated bubbles accounting for buckling and rupture. *The Journal of the Acoustical Society of America*, **118**, 3499–3505. 33

Matrone, G., Savoia, A.S., Caliano, G. & Magenes, G. (2015). The delay multiply and sum beamforming algorithm in ultrasound b-mode medical imaging. *IEEE Transactions on Medical Imaging*, **34**, 940–949. 39

Mclaughlan, J., Ingram, N., Smith, P.R., Harput, S., Coletta, P.L., Evans, S. & Freear, S. (2013). Increasing the sonoporation efficiency of targeted polydisperse microbubble populations using chirp excitation. *IEEE Transactions on Ultrasonics, Ferroelectrics, and Frequency Control*, **60**, 2511–2520. 4, 46, 75

McLaughlan, J.R., Harput, S., Abou-Saleh, R.H., Peyman, S.A., Evans, S. & Freear, S. (2017). Characterisation of liposome-loaded microbubble populations for subharmonic imaging. *Ultrasound in Medicine & Biology*, **43**, 346–356. 28, 68, 72

Meunier, J., Bertrand, M., Mailloux, G. & Petitclerc, R. (1988). Assessing local myocardial deformation from speckle tracking in echography. In *Medical Imaging II*, 20–31, International Society for Optics and Photonics. 25

Montaldo, G., Tanter, M., Bercoff, J., Benech, N. & Fink, M. (2009). Coherent plane-wave compounding for very high frame rate ultrasonography and transient elastography. *IEEE Transactions on Ultrasonics, Ferroelectrics, and Frequency Control*, **56**, 489–506. 4, 36, 46, 59

Moubark, A.M., Alomari, Z., Harput, S., Cowell, D.M. & Freear, S. (2016). Enhancement of contrast and resolution of b-mode plane wave imaging (pwi) with non-linear filtered delay multiply and sum (fdmas) beamforming. In *2016 IEEE International Ultrasonics Symposium (IUS)*, 1–4, IEEE. 36

Mulvana, H., Browning, R.J., Luan, Y., de Jong, N., Tang, M.X., Eckersley, R.J. & Stride, E. (2017). Characterization of contrast agent microbubbles for ultrasound imaging and therapy research. *IEEE Transactions on Ultrasonics, Ferroelectrics, and Frequency Control*, **64**, 232–251. 2, 82

Ng, A. & Swanevelder, J. (2011). Resolution in ultrasound imaging. *Continuing Education in Anaesthesia Critical Care & Pain*, **11**, 186–192. 18

Nie, L., Harput, S., Cowell, D.M.J. & Freear, S. (2016). Velocity estimation error reduction in stenosis areas using a correlation correction method. In *2016 IEEE International Ultrasonics Symposium (IUS)*, 1–4. i, 59, 85

Nie, L., Harput, S., McLaughlan, J.R., Cowell, D.M.J., Carpenter, T. & Freear, S. (2017). Acoustic microbubble trapping in blood mimicking fluid. In *2017 IEEE International Ultrasonics Symposium (IUS)*, 1–4. i

Nie, L., Carpenter, T.M., Cowell, D.M.J., McLaughlan, J.R., ubuku, A.A. & Freear, S. (2018a). High frame-rate coherent diverging wave imaging with 2-d motion compensation. In *2018 IEEE International Ultrasonics Symposium (IUS)*, 1–4. i

Nie, L., Harput, S., Cowell, D.M.J., Carpenter, T.M., Mclaughlan, J.R. & Freear, S. (2018b). Combining acoustic trapping with plane wave imaging for localized microbubble accumulation in large vessels. *IEEE Transactions on Ultrasonics, Ferroelectrics, and Frequency Control*, **65**, 1193–1204. i, xi, 5, 40, 75, 91

Nie, L., McLaughlan, J.R., Cowell, D.M.J., Carpenter, T.M. & Freear, S. (2018). Subharmonic plane wave imaging of liposome-loaded microbubbles. In *2018 IEEE International Ultrasonics Symposium (IUS)*, 1–4. i

Nie, L., Cowell, D.M.J., Carpenter, T.M., Mclaughlan, J.R., ubuku, A.A. & Freear, S. (2019). High-frame-rate contrast-enhanced echocardiography using diverging waves: 2-d motion estimation and compensation. *IEEE Transactions on Ultrasonics, Ferroelectrics, and Frequency Control*, **66**, 359–371. i, 110

Niu, L., Wang, J., Qian, M. & Zheng, H. (2009). Sub-piexl methods for improving vector quality in echo piv flow, imaging technology. In *2009 Annual International Conference of the IEEE Engineering in Medicine and Biology Society*, 487–490, IEEE. 25

Niu, L., Qian, M., Wan, K., Yu, W., Jin, Q., Ling, T., Gao, S. & Zheng, H. (2010). Ultrasonic particle image velocimetry for improved flow gradient imaging: algorithms, methodology and validation. *Physics in Medicine & Biology*, **55**, 2103. 59, 85, 87

Olszewski, R., Timperley, J., Cezary, S., Monaghan, M., Nihoyannopoulis, P., Senior, R. & Becher, H. (2007). The clinical applications of contrast echocardiography. *European Journal of Echocardiography*, **8**, s13–s23. 82

Opacic, T., Dencks, S., Theek, B., Piepenbrock, M., Ackermann, D., Rix, A., Lammers, T., Stickeler, E., Delorme, S., Schmitz, G. *et al.* (2018). Motion model ultrasound localization microscopy for preclinical and clinical multiparametric tumor characterization. *Nature Communications*, **9**, 1527. 11

Osmanski, B.F., Pernot, M., Montaldo, G. & Tanter, M. (2011). Imaging blood flow dynamics within fast moving tissue: Application to the myocardium. In *2011 IEEE International Ultrasonics Symposium*, 272–275. 36

Osmanski, B.F., Maresca, D., Messas, E., Tanter, M. & Pernot, M. (2014). Transthoracic ultrafast doppler imaging of human left ventricular hemodynamic function. *IEEE Transactions on Ultrasonics, Ferroelectrics, and Frequency Control*, **61**, 1268–1275. 11, 37, 83

Owen, J., Pankhurst, Q. & Stride, E. (2012). Magnetic targeting and ultrasound mediated drug delivery: Benefits, limitations and combination. *International Journal of Hyperthermia*, **28**, 362–373. 47

Owen, J., Crake, C., Lee, J.Y., Carugo, D., Beguin, E., Khrapitchev, A.A., Browning, R.J., Sibson, N. & Stride, E. (2018). A versatile method for the preparation of particle-loaded microbubbles for multimodality imaging and targeted drug delivery. *Drug Delivery and Translational Research*, **8**, 342–356. 121

Papadacci, C., Pernot, M., Couade, M., Fink, M. & Tanter, M. (2014). High-contrast ultrafast imaging of the heart. *IEEE Transactions on Ultrasonics, Ferroelectrics, and Frequency Control*, **61**, 288–301. 37, 46, 83

Patil, A.V., Rychak, J.J., Klibanov, A.L. & Hossack, J.A. (2011). Real-time technique for improving molecular imaging and guiding drug delivery in large blood vessels: in vitro and ex vivo results. *Molecular Imaging*, **10**, 7290–2011. 47

Petit, B., Bohren, Y., Gaud, E., Bussat, P., Arditi, M., Yan, F., Tranquart, F. & Allémann, E. (2015). Sonothrombolysis: the contribution of stable

and inertial cavitation to clot lysis. *Ultrasound in Medicine & Biology*, **41**, 1402–1410. 46

Peyman, S.A., Abou-Saleh, R.H., McLaughlan, J.R., Ingram, N., Johnson, B.R., Critchley, K., Freear, S., Evans, J.A., Markham, A.F., Coletta, P.L. *et al.* (2012). Expanding 3d geometry for enhanced on-chip microbubble production and single step formation of liposome modified microbubbles. *Lab on a Chip*, **12**, 4544–4552. 3, 66, 73

Phillips, P. (2001). Contrast pulse sequences (cps): imaging nonlinear microbubbles. In *Ultrasonics Symposium, 2001 IEEE*, vol. 2, 1739–1745, IEEE. 2, 29

Phillips, P. & Gardner, E. (2004). Contrast-agent detection and quantification. *European Radiology*, **14**, P4–P10. 46

Poree, J., Posada, D., Hodzic, A., Tournoux, F., Cloutier, G. & Garcia, D. (2016). High-frame-rate echocardiography using coherent compounding with doppler-based motion-compensation. *IEEE Transactions on Medical Imaging*, **35**, 1647–1657. 37, 82, 83, 84, 87, 88, 108, 114

Porter, T.R., Mulvagh, S.L., Abdelmoneim, S.S., Becher, H., Belcik, J.T., Bierig, M., Choy, J., Gaibazzi, N., Gillam, L.D., Janardhanan, R. *et al.* (2018). Clinical applications of ultrasonic enhancing agents in echocardiography: 2018 american society of echocardiography guidelines update. *Journal of the American Society of Echocardiography*, **31**, 241–274. 82

Qin, S., Caskey, C.F. & Ferrara, K.W. (2009). Ultrasound contrast microbubbles in imaging and therapy: physical principles and engineering. *Physics in Medicine & Biology*, **54**, R27. 82

Qiu, Y., Gigliotti, J.V., Wallace, M., Griggio, F., Demore, C.E., Cochran, S. & Trolier-McKinstry, S. (2015). Piezoelectric micromachined ultrasound transducer (pmut) arrays for integrated sensing, actuation and imaging. *Sensors*, **15**, 8020–8041. 3

Raiton, B., McLaughlan, J., Harput, S., Smith, P., Cowell, D. & Freear, S. (2012). The capture of flowing microbubbles with an ultrasonic tap using acoustic radiation force. *Applied Physics Letters*, **101**, 044102. 50

Ramalli, A., Dallai, A., Guidi, F., Bassi, L., Boni, E., Tong, L., Fradella, G., DHooge, J. & Tortoli, P. (2018). Real-time high-frame-rate cardiac b-mode and tissue doppler imaging based on multiline transmission and multiline acquisition. *IEEE Transactions on Ultrasonics, Ferroelectrics, and Frequency Control*, **65**, 2030–2041. 121

Ressner, M., Jansson, T., Cedefamn, J., Ask, P. & Janerot-Sjoberg, B. (2009). Contrast biases the autocorrelation phase shift estimation in doppler tissue imaging. *Ultrasound in Medicine & Biology*, **35**, 447–457. 108

Ricci, S., Ramalli, A., Bassi, L., Boni, E. & Tortoli, P. (2018). Real-time blood velocity vector measurement over a 2-d region. *IEEE Transactions on Ultrasonics, Ferroelectrics, and Frequency Control*, **65**, 201–209. 4

Roux, E., Ramalli, A., Liebgott, H., Cachard, C., Robini, M.C. & Tortoli, P. (2017). Wideband 2-d array design optimization with fabrication constraints for 3-d us imaging. *IEEE Transactions on Ultrasonics, Ferroelectrics, and Frequency Control*, **64**, 108–125. 67

Roux, E., Varray, F., Petrusca, L., Cachard, C., Tortoli, P. & Liebgott, H. (2018). Experimental 3-d ultrasound imaging with 2-d sparse arrays using focused and diverging waves. *Scientific Reports*, **8**, 9108. 104

Rueckert, D., Sonoda, L.I., Hayes, C., Hill, D.L.G., Leach, M.O. & Hawkes, D.J. (1999). Nonrigid registration using free-form deformations: application to breast mr images. *IEEE Transactions on Medical Imaging*, **18**, 712–721. 109, 111

Santos, P., Tong, L., Ortega, A., Lvstakken, L., Samset, E. & Dhooge, J. (2015). Acoustic output of multi-line transmit beamforming for fast cardiac imaging: a simulation study. *IEEE Transactions on Ultrasonics, Ferroelectrics, and Frequency Control*, **62**, 1320–1330. 83

Saris, A.E., Hansen, H.H., Fekkes, S., Nillesen, M.M., Rutten, M.C. & de Korte, C.L. (2016). A comparison between compounding techniques using large beam-steered plane wave imaging for blood vector velocity imaging in a carotid artery model. *IEEE Transactions on Ultrasonics, Ferroelectrics, and Frequency Control*, **63**, 1758–1771. 100

Scarano, F. (2001). Iterative image deformation methods in piv. *Measurement Science and Technology*, **13**, R1. 85

Senior, R., Becher, H., Monaghan, M., Agati, L., Zamorano, J., Vanoverschelde, J.L. & Nihoyannopoulos, P. (2009). Contrast echocardiography: evidence-based recommendations by european association of echocardiography. *European Journal of Echocardiography*, **10**, 194–212. 2, 11, 46, 82

Shamout, F.E., Pouliopoulos, A.N., Lee, P., Bonaccorsi, S., Towhidi, L., Krams, R. & Choi, J.J. (2015). Enhancement of non-invasive trans-membrane drug delivery using ultrasound and microbubbles during physiologically relevant flow. *Ultrasound in Medicine & Biology*, **41**, 2435–2448. 47

Shankar, P., Krishna, P.D. & Newhouse, V. (1998). Advantages of subharmonic over second harmonic backscatter for contrast-to-tissue echo enhancement. *Ultrasound in Medicine & Biology*, **24**, 395–399. 35

Shattuck, D.P., Weinshenker, M.D., Smith, S.W. & von Ramm, O.T. (1984). Explososcan: A parallel processing technique for high speed ultrasound imaging with linear phased arrays. *The Journal of the Acoustical Society of America*, **75**, 1273–1282. 83

Shi, W., Forsberg, F., Raichlen, J., Needleman, L. & Goldberg, B. (1999). Pressure dependence of subharmonic signals from contrast microbubbles. *Ultrasound in Medicine & Biology*, **25**, 275–283. 72

Simpson, D.H., Chin, C.T. & Burns, P.N. (1999). Pulse inversion doppler: a new method for detecting nonlinear echoes from microbubble contrast agents. *IEEE Transactions on Ultrasonics, Ferroelectrics, and Frequency Control*, **46**, 372–382. 29, 82

Skachkov, I., Luan, Y., van der Steen, A.F.W., de Jong, N. & Kooiman, K. (2014). Targeted microbubble mediated sonoporation of endothelial cells in vivo. *IEEE Transactions on Ultrasonics, Ferroelectrics, and Frequency Control*, **61**, 1661–1667. 3

Smith, P.R., Cowell, D.M.J. & Freear, S. (2013). Width-modulated square-wave pulses for ultrasound applications. *IEEE Transactions on Ultrasonics, Ferroelectrics, and Frequency Control*, **60**, 2244–2256. 58, 88

Song, P., Manduca, A., Trzasko, J.D. & Chen, S. (2017). Ultrasound small vessel imaging with block-wise adaptive local clutter filtering. *IEEE Transactions on Medical Imaging*, **36**, 251–262. 43, 62

Song, P., Trzasko, J.D., Manduca, A., Qiang, B., Kadirvel, R., Kallmes, D.F. & Chen, S. (2017). Accelerated singular value-based ultrasound blood flow clutter filtering with randomized singular value decomposition and randomized spatial downsampling. *IEEE Transactions on Ultrasonics, Ferroelectrics, and Frequency Control*, **64**, 706–716. 43

Szabo, T.L. (2004). *Diagnostic ultrasound imaging: inside out*. Academic Press. 1, 13

Tachibana, K. & Tachibana, S. (1995). Albumin microbubble echo-contrast material as an enhancer for ultrasound accelerated thrombolysis. *Circulation*, **92**, 1148–1150. 46

Takalkar, A.M., Klibanov, A.L., Rychak, J.J., Lindner, J.R. & Ley, K. (2004). Binding and detachment dynamics of microbubbles targeted to p-selectin under controlled shear flow. *Journal of Controlled Release*, **96**, 473–482. 47

Tang, M.X., Mulvana, H., Gauthier, T., Lim, A., Cosgrove, D., Eckersley, R. & Stride, E. (2011). Quantitative contrast-enhanced ultrasound imaging: a review of sources of variability. *Interface Focus*, **1**, 520–539. 104

Tong, L., Ramalli, A., Jasaityte, R., Tortoli, P. & D'hooge, J. (2014). Multi-transmit beam forming for fast cardiac imaging – experimental validation and in vivo application. *IEEE Transactions on Medical Imaging*, **33**, 1205–1219. 83

Tong, L., Ramalli, A., Tortoli, P., Fradella, G., Caciolli, S., Luo, J. & D'hooge, J. (2016). Wide-angle tissue doppler imaging at high frame rate using multi-line transmit beamforming: An experimental validation in vivo. *IEEE Transactions on Medical Imaging*, **35**, 521–528. 83

Tong, L., He, Q., Ortega, A., Ramalli, A., Tortoli, P., Luo, J. & Dhooge, J. (2019). Coded excitation for crosstalk suppression in multi-line transmit beamforming: Simulation study and experimental validation. *Applied Sciences*, **9**, 486. xi, 12

Tortoli, P., Pratesi, M. & Michelassi, V. (2000). Doppler spectra from contrast agents crossing an ultrasound field. *IEEE Transactions on Ultrasonics, Ferroelectrics, and Frequency Control*, **47**, 716–726. 53

Tortoli, P., Bambi, G. & Ricci, S. (2006). Accurate doppler angle estimation for vector flow measurements. *IEEE Transactions on Ultrasonics, Ferroelectrics, and Frequency control*, **53**, 1425–1431. 24

Toulemonde, M., Li, Y., Lin, S., Tang, M.X., Butler, M., Sboros, V., Eckersley, R. & Duncan, W.C. (2016). Cardiac imaging with high frame rate contrast enhanced ultrasound: In-vivo demonstration. In *2016 IEEE International Ultrasonics Symposium (IUS)*, 1–4. 37, 83

Toulemonde, M., Duncan, W.C., Leow, C., Sboros, V., Li, Y., Eckersley, R.J., Lin, S., Tang, M. & Butler, M. (2017a). Cardiac flow mapping using high frame rate diverging wave contrast enhanced ultrasound and image tracking. In *2017 IEEE International Ultrasonics Symposium (IUS)*, 1–4. 39

Toulemonde, M., Duncan, W.C., Stanziola, A., Sboros, V., Li, Y., Eckersley, R.J., Lin, S., Tang, M.X. & Butler, M. (2017b). Effects of motion on high frame rate contrast enhanced echocardiography and its correction. In *2017 IEEE International Ultrasonics Symposium (IUS)*, 1–4. 84, 108, 111

Toulemonde, M., Li, Y., Lin, S., Cordonnier, F., Butler, M., Duncan, W.C., Eckersley, R.J., Sboros, V. & Tang, M. (2018). High-frame-rate contrast echocardiography using diverging waves: Initial in vitro and in vivo evaluation. *IEEE Transactions on Ultrasonics, Ferroelectrics, and Frequency Control*, **65**, 2212–2221. 28, 40, 98

Toulemonde, M.E., Corbett, R., Papadopoulou, V., Chahal, N., Li, Y., Leow, C.H., Cosgrove, D.O., Eckersley, R.J., Duncan, N., Senior, R. &

Tang, M.X. (2017c). High frame-rate contrast echocardiography: In-human demonstration. *JACC: Cardiovascular Imaging*. 46, 82, 84, 88

Tremblay-Darveau, C., Williams, R., Milot, L., Bruce, M. & Burns, P.N. (2014). Combined perfusion and doppler imaging using plane-wave nonlinear detection and microbubble contrast agents. *IEEE Transactions on Ultrasonics, Ferroelectrics, and Frequency Control*, **61**, 1988–2000. 39, 46, 82

Tremblay-Darveau, C., Williams, R., Milot, L., Bruce, M. & Burns, P.N. (2016a). Visualizing the tumor microvasculature with a nonlinear plane-wave doppler imaging scheme based on amplitude modulation. *IEEE Transactions on Medical Imaging*, **35**, 699–709. 39, 82

Tremblay-Darveau, C., Williams, R., Sheeran, P.S., Milot, L., Bruce, M. & Burns, P.N. (2016b). Concepts and tradeoffs in velocity estimation with plane-wave contrast-enhanced doppler. *IEEE Transactions on Ultrasonics, Ferroelectrics, and Frequency Control*, **63**, 1890–1905. 39

Udesen, J. & Jensen, J.A. (2006). Investigation of transverse oscillation method. *IEEE Transactions on Ultrasonics, Ferroelectrics, and Frequency Control*, **53**, 959–971. 24

van Neer, P.L., Danilouchkine, M.G., Verweij, M.D., Demi, L., Voormolen, M.M., van der Steen, A.F. & de Jong, N. (2011). Comparison of fundamental, second harmonic, and superharmonic imaging: A simulation study. *The Journal of the Acoustical Society of America*, **130**, 3148–3157. 2

Van Wamel, A., Kooiman, K., Harteveld, M., Emmer, M., Folkert, J., Versluis, M. & De Jong, N. (2006). Vibrating microbubbles poking individual cells: drug transfer into cells via sonoporation. *Journal of Controlled Release*, **112**, 149–155. 46

Viti, J., Vos, H.J., d. Jong, N., Guidi, F. & Tortoli, P. (2016). Detection of contrast agents: Plane wave versus focused transmission. *IEEE Transactions on Ultrasonics, Ferroelectrics, and Frequency Control*, **63**, 203–211. 46, 50, 72, 79

Voorneveld, J., Muralidharan, A., Hope, T., Vos, H.J., Kruizinga, P., van der Steen, A.F.W., Gijsen, F.J.H., Kenjeres, S., de Jong, N. & Bosch, J.G. (2017). High frame rate ultrasound particle image velocimetry for estimating high velocity flow patterns in the left ventricle. *IEEE Transactions on Ultrasonics, Ferroelectrics, and Frequency Control*, 1–1. 83

Wang, S., Hossack, J.A., Klibanov, A.L. & Mauldin Jr, F.W. (2013). Binding dynamics of targeted microbubbles in response to modulated acoustic radiation force. *Physics in Medicine & Biology*, **59**, 465. 47, 66

Wang, S., Wang, C.Y., Unnikrishnan, S., Klibanov, A.L., Hossack, J.A. & Mauldin Jr, F.W. (2015). Optical verification of microbubble response to acoustic radiation force in large vessels with in vivo results. *Investigative Radiology*, **50**, 772–784. 66

Ward, M., Wu, J. & Chiu, J.F. (2000). Experimental study of the effects of optison® concentration on sonoporation in vitro. *Ultrasound in Medicine & Biology*, **26**, 1169–1175. 47

Westerweel, J. (1997). Fundamentals of digital particle image velocimetry. *Measurement Science and Technology*, **8**, 1379. 101

Westerweel, J. & Scarano, F. (2005). Universal outlier detection for piv data. *Experiments in Fluids*, **39**, 1096–1100. 87

Yamakoshi, Y. & Noguchi, Y. (1998). Micro particle trapping by opposite phases ultrasonic travelling waves. *Ultrasonics*, **36**, 873–878. 51, 53

Yiu, B.Y., Tsang, I.K. & Alfred, C. (2008). A modified synthetic aperture imaging approach with axial motion compensation. In *Ultrasonics Symposium, 2008. IUS 2008. IEEE*, 1254–1257, IEEE. 83, 84

Yiu, B.Y., Lai, S.S. & Alfred, C. (2014). Vector projectile imaging: time-resolved dynamic visualization of complex flow patterns. *Ultrasound in Medicine & Biology*, **40**, 2295–2309. 24

Yiu, B.Y.S., Tsang, I.K.H. & Yu, A.C.H. (2011). Gpu-based beamformer: Fast realization of plane wave compounding and synthetic aperture imaging. *IEEE Transactions on Ultrasonics, Ferroelectrics, and Frequency Control*, **58**, 1698–1705. 67

Yiu, B.Y.S., Walczak, M., Lewandowski, M. & Yu, A.C.H. (2019). Live ultrasound color encoded speckle imaging platform for real-time complex flow visualization in vivo. *IEEE Transactions on Ultrasonics, Ferroelectrics, and Frequency Control*, 1–1. 121

Yu, A.C.H. & Lovstakken, L. (2010). Eigen-based clutter filter design for ultrasound color flow imaging: a review. *IEEE Transactions on Ultrasonics, Ferroelectrics, and Frequency Control*, **57**, 1096–1111. 40

Zurakhov, G., Tong, L., Ramalli, A., Tortoli, P., Dhooge, J., Friedman, Z. & Adam, D. (2018). Multiline transmit beamforming combined with adaptive apodization. *IEEE Transactions on Ultrasonics, Ferroelectrics, and Frequency Control*, **65**, 535–545. 83